Semi-analytical approaches for the prediction of the noise produced by ducted wind turbines

Küçükosman, Cansev

DOI
10.4233/uuid:b749675c-edb1-4355-ba09-bf46278077d0

Publication date
2019

Document Version
Final published version

Citation (APA)
Küçükosman, C. (2019). *Semi-analytical approaches for the prediction of the noise produced by ducted wind turbines*. [Dissertation (TU Delft), Delft University of Technology]. https://doi.org/10.4233/uuid:b749675c-edb1-4355-ba09-bf46278077d0

SEMI - ANALYTICAL APPROACHES FOR THE PREDICTION OF THE NOISE PRODUCED BY DUCTED WIND TURBINES

YAKUT CANSEV KÜÇÜKOSMAN

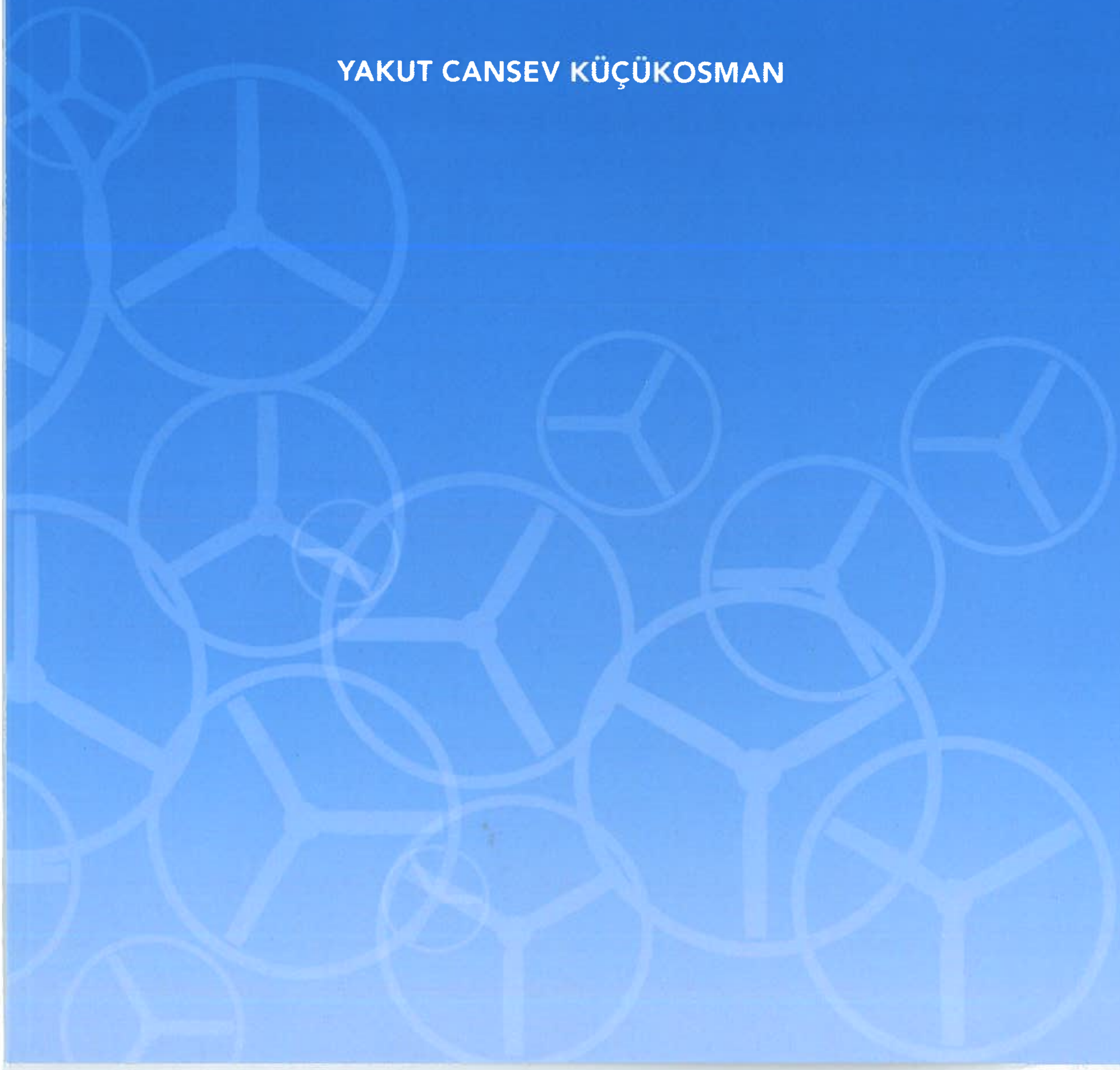

Propositions

accompanying the dissertation

SEMI-ANALYTICAL APPROACHES FOR THE PREDICTION OF THE NOISE PRODUCED BY DUCTED WIND TURBINES

by

Yakut Cansev KÜÇÜKOSMAN

1. The acceleration of the flow above the fairing decreases the turbulent intensity, however, in the vicinity of the probe, this advantage is not observed (*Chapter 6*).
2. Analytical solutions provide insight and a good basis to improve the numerical models, but do not always yield a good match with experimental data (*Chapter 6*).
3. It is hard to obtain a mesh insensitive solution for local variables (*Part I*).
4. In terms of accuracy vs computational cost balance, it is reasonable to simplify a 3D problem to a 2D one as long as the three-dimensional effects can be represented through the boundary conditions of the two-dimensional simulations (*Chapter 5*).
5. Listening to someone does not mean that one understands the situation unless s/he establishes empathy.
6. Mindfulness is the key to make everyone's life easier.
7. If we don't take actions, we are responsible for what is coming next.
8. The essence of being an experimentalist is to acknowledge the fact that an experiment is a losing streak.
9. Life is full of ups and downs if we define it that way but in reality, it is full of opportunities.
10. Learning one's language does not always give the opportunity to understand the humour.

These propositions are regarded as opposable and defendable, and have been approved as such by the promotor prof. dr. D. Casalino.

SEMI-ANALYTICAL APPROACHES FOR THE PREDICTION OF THE NOISE PRODUCED BY DUCTED WIND TURBINES

SEMI-ANALYTICAL APPROACHES FOR THE PREDICTION OF THE NOISE PRODUCED BY DUCTED WIND TURBINES

Dissertation

for the purpose of obtaining the degree of doctor
at Delft University of Technology
by the authority of the Rector Magnificus prof.dr.ir. T.H.J.J. van der Hagen
chair of the Board for Doctorates
to be defended publicly on
Thursday 21 March 2019 at 10:00 o'clock

by

Yakut Cansev KÜÇÜKOSMAN

Master of Science in Turbulence,
École Centrale de Lille, École Nationale Supérieure de Mécanique et d'Aérotechnique,
École Nationale Supérieure d'ingénieurs de Poitiers, France
born in Ankara, Turkey

This dissertation has been approved by the promotors.

Composition of the doctoral committee:

Rector Magnificus	chairperson
Prof.dr. D. Casalino	Delft University of Technology, promotor
Prof.dr.ir. C. Schram	von Karman Institute for Fluid Dynamics, Belgium, copromotor

Independent members:

Prof.dr. S. Moreau	Université de Sherbrooke, Canada
Prof.dr. M. Roger	École Centrale de Lyon, France
Prof.dr. S.J. Watson	Delft University of Technology
Dr. ir. S. Oerlemans	Siemens Gamesa Renewable Energy, Denmark
Prof.dr. F. Scarano	Delft University of Technology, reserve member

Other members:

Dr. J. Christophe	von Karman Institute for Fluid Dynamics, Belgium

Keywords: wind turbine noise, semi-analytical models, ducted wind turbines

Printed by: IPSKAMP printing

Cover by: Argun Çençen

ISBN 978-94-028-1421-7

CONTENTS

NOMENCLATURE

Acronyms

1/2/3D	One/Two/Three Dimensional
a.o.a	Angle of Attack
ABL	Atmospheric Boundary Layer
AMI	Arbitrary Mesh Interface
APG	Adverse Pressure Gradient
BATMAN	Broadband And Tonal Models for Airfoil Noise
BEM	Blade Element Momentum
BIWT	Building Integrated Wind Turbines
BPF	Blade Passing Frequency
CAD	Computer-Aided Design
CFD	Computational Fluid Dynamics
CPU	Central Processing Unit
CROR	Contra-rotating Open Rotor
DAWT	Diffuser Augmented Wind Turbine
FPG	Favorable Pressure Gradient
FWH	Ffowcs Williams and Hawkings
HWA	Hot Wire Anemometer
MRF	Multiple Reference Frame
PIV	Particle Image Velocimetry
PSD	Power Spectrum Density
RANS	Reynolds Averaged Navier-Stokes
RPM	Random Particle-Mesh
RSNM	RANS-based Statistical Noise Model

SMM	Sliding Mesh Method
SNGR	Stochastic Noise Generation and Radiation
SPL	Sound Pressure Level
SRF	Single Reference Frame
SRS	Scale-Resolving Simulation
T.I.	Turbulence Intensity
TKE	Turbulent Kinetic Energy
VKI	von Karman Institute for Fluid Dynamics
WPS	Wall-Pressure Spectrum
ZPG	Zero Pressure Gradient

Coefficients

C_f	Skin friction coefficient	[-]
C_p	Pressure coefficient	[-]
C_{power}	Power coefficient	[-]

Greek Symbols

β_c	Clauser's parameter	[-]
Δ	Rotta-Caluser parameter	[-]
δ	Boundary layer thickness	[m]
δ^*	Displacement thickness	[m]
Δ_*	Zagarola-Smits'parameter	[-]
ϵ	Turbulent dissipation	$[m^2/s^3]$
γ	Specific heat ratio	[-]
κ	von Karman constant	[-]
Λ	Eddy size	[m]
λ	Acoustic wavelength	[m]
$\mathcal{L}$	Aeroacoustic transfer function	[-]
μ	Dynamic viscosity	$[Pa \cdot s]$
ν	Kinematic viscosity	$[m^2/s]$

Ω	Specific turbulence dissipation rate	$[1/s]$
ω	Angular frequency	[1/s]
Ω_{rot}	Angular velocity	[rad/s]
ϕ_{pp}	Wall-pressure PSD	dB/Hz
Π	Cole's wake parameter	[-]
Ψ	Azimuthal angle	[rad]
ρ	Density	$[kg/m^3]$
τ_w	Wall shear stress	$[Pa/m^2]$
θ	Momentum thickness	[m]
Θ_r	Polar observation angle	[rad]
u_τ	Friction velocity	[m/s]

Roman Symbols

c	chord of the blade or airfoil	[m]
c_0	Speed of sound	[m/s]
d	span	[m]
H	Shape factor	[-]
J	Bessel function	[-]
k	Acoustic wavenumber	$[m^-1]$
k_t	Turbulent kinetic energy	$[m^2/s^2]$
l_y	Spanwise correlation length	[m]
M	Mach number	[-]
Pr	Prandtl number	[-]
q	Dynamic pressure	[Pa]
R	Distance between source and observer	[m]
R_T	Ratio of the outer to inner time scales	[m]
Re	Reynolds number	[-]
S_{pp}	Far-field acoustic PSD	[dB/hz]
St	Sthrouhal number	[-]

U	Axial velocity	[m/s]
U_c	Convective velocity	[m/s]
U_e	External velocity	[m/s]
U_∞	free-stream velocity	[m/s]
B	Number of blades	[-]
b	Corcos constant	[-]
p	Pressure	$[Pa]$
X, Y, Z	Observer coordinate system	[m]
x, y, z	Source coordinate system	[m]

Subscripts

0	Local free-stream value
∞	Free-stream value
r,θ,z	Radial, azimuthal, axial coordinates
x, y, z	Streamwise, normal-to-wall and spanwise coordiantes

ABSTRACT

The integration of wind turbines into urban environments is a challenging task due to the reduced wind speed and high turbulence levels caused by the surface resistance, as well as limited spacing. If a specific building arrangement is explored, an improvement in wind speed can be obtained. This would be especially beneficial for tall buildings where a wind turbine can be placed on the roof, side, or through a duct. However, the main problem associated with the integration of wind turbines is the acoustic annoyance. Therefore, the focus of this thesis is twofold. First, a robust, accurate, and low computational cost numerical methodology is proposed to predict the trailing edge noise for a ducted wind turbine. Second, a measurement device is developed to acquire noise emitted by a rotating machine where the duct surface cannot be altered. An investigation of the incoming flow on the noise emitted by a building-integrated wind turbine is conducted by different aerodynamic roughness lengths.

The far-field trailing-edge noise prediction by the Amiet analytical theory is applied for two isolated airfoils, the NACA0012 at 0° and the DU96-W180 at 4°. The comparison of the wall-pressure spectrum is performed by using the state-of-art semi-empirical models; Goody, Rozenberg, Kamruzzaman, Catlett, Hu & Herr and Lee, and an integral model from Panton & Linebarger. A sensitivity analysis of the wall-pressure spectrum and far-field noise prediction based on different mesh resolutions is investigated and the far-field results are validated with experimental data. Furthermore, another analysis is performed by varying the probe location to quantify the sensitivity of the wall-pressure spectrum obtained by different models as well as the corresponding far-field noise predictions.

The extended variant of Schlinker and Amiet theory is applied to a full scale commercial ducted wind turbine. The three-dimensional Reynolds Averaged Navier-Stokes simulation with a Multiple Reference Frame is performed to obtain the flow field. The far-field noise is predicted by a strip theory by neglecting the scattering due to the presence of the diffuser. To reduce the three-dimensional computational cost, a two dimensional isoradial approach is proposed and applied to the same configuration without considering the flow acceleration due to the diffuser and nacelle. To reproduce the flow acceleration due to the diffuser and nacelle, a two dimensional axisymmetric simulation without the presence of a blade is conducted. Several locations obtained from this simulation are then imposed as an inlet condition for the two dimensional isoradial approach. A comparison between the three and two dimensional approaches is assessed by the wall-pressure spectrum and the far-field noise prediction obtained upstream and downstream of the blade.

Experimental considerations regarding a noise measurement technique of a ducted wind turbine and the assessment of the noise emitted by a building-integrated wind turbine in an urban environment are investigated. The former study focuses on a development of a fairing based on a remote microphone technique. The fairing is designed as a streamlined profile to avoid additional disturbances as well as to reduce the turbulence level. The microphone is located inside of the fairing and connected to the surroundings with a pipe-cavity system. The system is modelled analytically and compared with the system response function. The investigation of the fairing is performed aerodynamically and aeroacoustically with different wind speeds and turbulence levels. Later, this device is validated through with a practical application. The latter study investigates the effect of different incoming flows both in magnitude and turbulence intensity on the noise emission in the case of a building integrated wind turbine placed through a duct. The acoustic measurements are performed for two different incoming flow speeds and six different wind directions with nine microphones. Furthermore, the power efficiency of the in-duct wind turbine is compared to another wind turbine, which is placed on the top of a model building.

ABSTRACT

De integratie van windturbines in stedelijke omgeving is een uitdagende taak vanwege de verminderde windsnelheid, de hoge turbulentie veroorzaakt door de bebouwde-omgeving en de beperkte ruimte. Indien een specifieke bouwinrichting wordt onderzocht, kan een verhoging in windsnelheid verkregen worden. Dit zou vooral voordelig zijn voor hoge gebouwen waar een windturbine op het dak, de zijkant of in een opening kan worden geplaatst. Toch is het grootste probleem de akoestische hinder geassocieerd aan de integratie van windturbines. Bijgevolg is de focus van dit proefschrift tweeledig. Eerst wordt er een robuuste, nauwkeurige numerieke methodologie voorgesteld met lage rekenkundige kost om het geluid van de vleugelachterrand te voorspellen voor een windturbine in een opening. Ten tweede wordt een niet-intrusief meetapparaat ontwikkeld om het uitgezonden geluid afkomstig van de roterende machine op te meten. Een onderzoek van de inkomende vind stroom op het geluid uitgezonden door een gebouw-geïntegreerde windturbine wordt uitgevoerd met verschillende aerodynamische ruwheidslengtes.

De voorspelling van het verre-veld vleugelachterrand geluid door de Amiet-analytische theorie wordt toegepast voor twee geïsoleerde schoepen, de NACA0012 op 0X en de DU96-W180 op 4X. De vergelijking van het wand-drukspectrum wordt uitgevoerd met behulp van state-of-art, semi-empirische modellen; Goody, Rozenberg, Kamruzzaman, Catlett, Hu & Herr en Lee, en het volledig model van Panton & Linebarger. Een gevoeligheidsanalyse van het wanddrukspectrum en verre-veld geluidsvoorspelling wordt onderzocht op basis van verschillende grid resoluties en de verre-veld-resultaten worden gevalideerd met experimentele gegevens. Verder wordt nog een analyse uitgevoerd door de locatie van de sonde te variëren om de gevoeligheid van het wanddrukspectrum, verkregen door verschillende modellen, evenals de bijbehorende verre-veld geluidvoorspellingen, te kwantificeren.

De uitgebreide variant van de Schlinker en Amiet-theorie wordt toegepast op een commerciële windturbine geplaatst in een opening, en dit op volledige schaal. De driedimensionale Reynolds Averaged Navier-Stokes simulatie met een 'Multiple Reference Frame' wordt uitgevoerd om het stroomveld te verkrijgen. Het verre-veld geluid wordt voorspeld door een striptheorie door de verstrooiing vanwege de aanwezigheid van de diffuser te verwaarlozen. Om de driedimensionale computerkosten te verminderen wordt er een tweedimensionale isoradiale benadering voorgesteld en toegepast op dezelfde configuratie zonder rekening te houden met de stroomversnelling als gevolg van de diffuser en de nacelle. Om de stroomversnelling door de diffuser en de nacelle te reproduceren, wordt een tweedimensionale asymmetrische simulatie zonder schoep uitgevoerd. Verschillende locaties verkregen uit deze simulatie worden dan opgelegd als inlaatvoorwaarde voor de tweedimensionale isoradiale benadering. Een vergelijking tussen de drie- en tweedimensionale benaderingen wordt uitgevoerd door het wanddrukspectrum en de voorspelling van het verre-veld geluid verkregen stroomopwaarts en stroomafwaarts van het blad te vergelijken.

Experimentele overwegingen met betrekking tot een geluidsmeettechniek van een windturbine geplaatst in een opening en de beoordeling van het geluid van een gebouw-geïntegreerde windturbine in een stedelijke omgeving worden onderzocht. De vorige studie richt zich op de ontwikkeling van een kap gebaseerd op een microfoontechniek op afstand. De kap is ontworpen als een gestroomlijnd profiel om extra storingen te voorkomen en om de turbulentie te verminderen. De microfoon bevindt zich in de kap en is verbonden met de omgeving dankzij een openingholtesysteem. Het systeem is analytisch gemodelleerd en vergeleken met de responsfunctie van het systeem. Een aerodynamisch en aeroakoustisch onderzoek van de stroomlijnkap wordt uitgevoerd met verschillende windsnelheden en turbulentieniveaus. Vervolgens wordt dit apparaat gevalideerd dankzij een praktische toepassing. Deze studie onderzoekt het effect van verschillende inkomende vind stromen, zowel in grootte als turbulentie-intensiteit, op het uitgezonden geluid in het geval van een gebouw-geïntegreerde windturbine geplaatst in een opening. De akoestische metingen worden uitgevoerd voor twee verschillende inkomende stroomsnelheden en zes verschillende windrichtingen met negen microfoons. Verder wordt de stroomefficiëntie van de windturbine in de opening vergeleken met een andere windturbine, geplaatst boven op een modelgebouw.

1

INTRODUCTION

This chapter is devoted to a brief introduction of the thesis followed by the objectives and outline.

1.1. BACKGROUND

The energy demand due to urbanization and industrialization has raised in recent years [109]. As stated by the United Nations in 2007 [137], the energy consumption in cities was found to be around 75 % which will increase due to migration to the cities from the rural areas in developing countries [4]. If the traditional energy production approach remains unchanged, the depletion of fossil fuels will result in a higher cost [146] as well as green-house gas emission causing environmental problems [106]. To overcome these issues, it is necessary to find sustainable and renewable energy solutions for the future. Since a great amount of energy consumption occurs in a city, it would be effective and efficient to generate power within them. That will also help to reduce the use of transmission and distribution infrastructure throughout the generation of power to the consumer as well as the transmission losses. In recent years, a lot of care has been taken to investigate and improve the wind energy applications in urban areas as an alternative energy resource.

The assessment of wind energy in urban environments has interesting challenges compared to open terrains. Firstly, the resistance caused by buildings in urban environments reduces the wind speed and produces a higher turbulence level with rapid fluctuations both in magnitude and direction [52, 106, 178]. Secondly, the limited space in the urban environment prevents installation of large wind turbines. Even though the incoming wind speed and turbulent inflow conditions for the urban boundary layer are highly dependent on the atmospheric conditions, the effect of urban geometry overcomes them, especially over the surface layer, which can be approximated as 10% of the total atmospheric boundary layer thickness [183]. Therefore, specific building arrangements can also be used to alter the wind flow within the urban canopy to further improve the wind energy potential. As can be expected, tall buildings provide better conditions to this end. The wind turbines can be placed either on the top of the building, within a duct or around them [178]. It has been found that a well-situated building arrangement can lead to a power increase up to 70% [131]. As stated by Hu and Cheng [99], the idea of ducted wind turbines is based on adjusting the wind flow, not only in terms of wind speed magnitude but also wind direction which increases the power efficiency.

Even though the wind energy is promising in the long term, social acceptance plays a key role in the integration of wind turbines in urban environments [177]. The main issue related to social acceptance is associated with the acoustic annoyance caused by wind turbines. As a siting of wind turbine is unique in each urban environment, an investigation of special positioning is necessary to take into account relevant factors including the buildings, trees and other obstacles' arrangement as well as the effect of the noise emission to the immediate environment [177]. For this reason, there is a solid need to predict and reduce the noise emitted by wind turbines since small modifications in the blade design can yield a considerable noise reduction [22]. Thus, robust and accurate as well as low cost prediction methods are necessary for the early stage design of wind turbines.

1.2. MOTIVATIONS AND OBJECTIVES

To integrate the wind turbines into urban environments, it is important to overcome the acoustic annoyance caused by wind turbines [80, 152, 182]. Hence, the motivation of this thesis is to investigate this issue both numerically and experimentally. Even though, the numerical methods are being used to estimate the acoustic far-field noise for almost a decade [22], it is also critical to quantitatively evaluate the accuracy and robustness of the low fidelity prediction methods such as hybrid methods for further simplifications. The other motivation of this thesis is to provide a preliminary experimental methodology to investigate the effect of urban environment on the power efficiency and noise emission of building-integrated wind turbines as the experimental investigation of building-integrated wind turbines is a topic still open to further research. On this framework, the thesis is composed of two main parts. The first part focuses on accuracy and robustness of the low cost prediction methods and proposes a methodology to further simplify the three dimensional approach to two dimensions. The second part focuses on the development of measurement techniques for already existing ducted rotating machines and investigations of the urban topology on the noise emitted by building-integrated wind turbine in terms of turbulence and inflow direction. Furthermore, this part also answers the convenient siting of the wind turbine on the building by means of power production. The following objectives are followed throughout the thesis:

- To propose a methodology that can predict far-field trailing edge noise from an airfoil by considering the simulation cost. The chosen hybrid method combines the flow field obtained by Reynolds-Averaged-Navier-Stokes (RANS) simulations and acoustic far-field by Amiet's theory.

- To perform a quantitative comparison of state-of-art wall pressure models by means of 2D RANS simulations with several airfoil configurations and to compare with experimental results.

- To conduct a grid sensitivity analysis for RANS simulations to quantify the robustness and accuracy of the wall-pressure models as well as the far-field noise prediction.
- To extend the existed model for a full scale wind turbine and to propose a further simplification of the 3D method to a 2D.
- To develop a measurement device based on a remote microphone technique to acquire the noise emitted by ducted rotating machines.
- To asses the effect of the urban environment on the noise emission by a building-integrated wind turbine.

1.3. THESIS OUTLINE

The thesis is composed of two main parts that consist of numerical and experimental considerations of ducted wind turbines, defined as Part I and Part II. The introduction is followed by Chapter 2, which presents a review of a diffuser-augmented wind turbine and noise mechanism. After Chapter 2, Part I starts with the numerical methodology for both two and three dimensional techniques (Chapter 3). The accuracy and mesh sensitivity of RANS based trailing edge predictions using Amiet's theory is presented in Chapter 4. Part I is finalized with Chapter 5, which presents numerical results for a full-scale ducted wind turbine. Part II is focused on experimental considerations of ducted wind turbines, including development of a measurement device based on a remote microphone technique (Chapter 6) and the investigation of inflow conditions on the wind turbine efficiency (Chapter 7). Finally, a brief summary of the obtained main results along with the conclusions and the possible future work are presented in Chapter 8.

2

REVIEW OF DIFFUSER-AUGMENTED WIND TURBINE AND NOISE MECHANISM

In this chapter, the basic working principle of conventional and diffuser-augmented wind turbine (DAWT) will be explained. Later, the development of ducted wind turbines as well as the general noise mechanism observed in wind turbines without a duct will be explained. Finally, the present numerical noise prediction methods will be discussed.

2.1. WORKING PRINCIPLE OF DIFFUSER-AUGMENTED WIND TURBINES

The wind turbine rotor extracts energy by slowing down passing wind. To obtain a 100% efficient wind turbine, the wind speed downstream the wind turbine has to be zero. However, that would prevent the upstream wind from moving through the turbine which causes the turbine stop spinning. According to Betz's law [23], the maximum kinetic energy a bare wind turbine can extract is $16/27 \simeq 0.59$ which is known as the Betz limit. The axial velocity and pressure distributions on the centreline are shown in Fig. 2.1. It can be observed that for the maximum operating conditions, the flow velocity upstream of the rotor decreases to $\frac{2}{3}U_\infty$, where U_∞ is the free-stream velocity, as the cross sectional area of the stream tube increases. At the downstream side, the cross-sectional area is twice the disk area which results in the velocity decreasing further down to $\frac{1}{3}U_\infty$.

In order to exceed the Betz limit, the power augmentation can be performed in two ways. The first one is to use a vortex generator to create a low-pressure region to accelerate the flow as shown in Fig. 2.2. The second method is to use an annular lifting device whose suction side is pointed inwards to create a lift force which increases the velocity at the centerline as shown in Fig. 2.3.

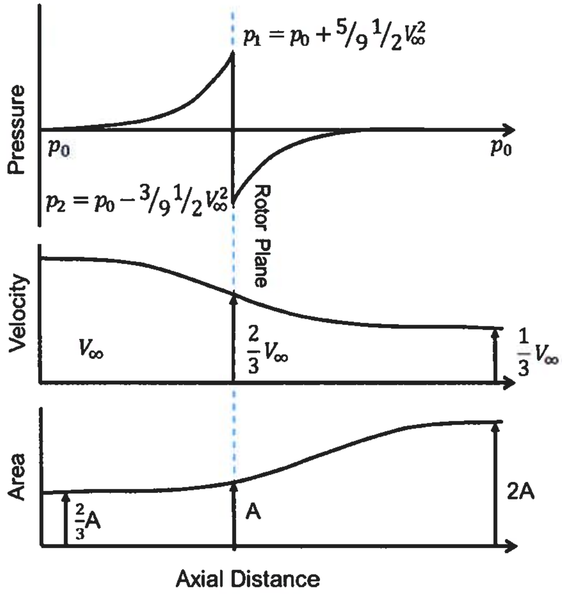

Figure 2.1: Ideal axial pressure, velocity and disk area variations over a bare wind turbine rotor [184].

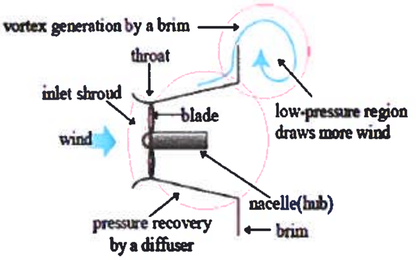

Figure 2.2: Flow around a wind turbine with a vortex generator [139].

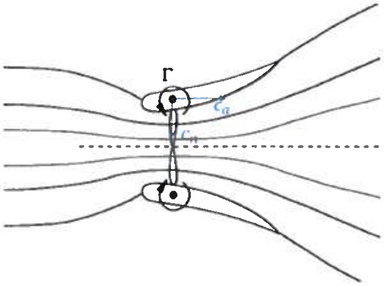

Figure 2.3: Flow around a wind turbine with a diffuser [88].

2.2. REVIEW OF DIFFUSER-AUGMENTED WIND TURBINES

In the 1920s, the first development of ducted wind turbines was acknowledged by Betz [24]. He had formulated the correct theory with a restrictive assumption in which he assumed the exit static pressure is equal to the ambient pressure. He concluded that ducted wind turbines were uneconomical for practical applications. In the 1950s, Sanuki [163] published the first experimental results for ducted wind turbines and was followed by Iwasaki [107]. They both found an increase in power output compared to bare wind turbines. Independently, Lilley et al. [124] demonstrated, based on the momentum and vortex theories for a ducted wind turbine, that the augmented power output was explained by an increase in axial velocity and a decrease of tip losses. In the report, they proposed the ideal shrouded windmill by considering the cost and stated an increase of 65% power output compared to the unshrouded windmill. Moreover, further increase of the power output could be achieved by adding an aerodynamic surface at the exit of the diffuser. Early in the 1960s, an Israeli group [114, 115] achieved a power augmentation by a factor of 3.5 with a longer shroud design which was inconvenient for commercial applications due to high cost of the duct length. A shorter duct with the same exit area ratio requires a rapidly diverging diffuser. As a drawback, this would cause the flow to separate, and hence, a reduction in the performance. To overcome the separation, gurney flaps were implemented at the duct outlet to reduce the exit pressure. Igra [102, 103, 104] realized that the power augmentation was due to sub-atmospheric pressure at the exit, thereby increasing the mass flow.

At the same time, Foreman [73, 76, 77] was focusing on Diffuser Augmented Wind Turbines (DAWTs) to find alternative energy sources due to the oil crisis in 1974. In contrast to other researchers, the attempt was to control the boundary layer to create a jet flow by applying slots. The energized flow entering through the slots helps to delay or prevent flow separation, which allows shorter duct lengths and larger outlet-to-inlet area ratio DAWTs. They also observed that the separation in the diffuser was delayed having an actual wind turbine within the duct instead of a gauze screen (sometime used to represent the rotor pressure drop) since the swirling flow at the wake of the rotor enhanced momentum transfer to the boundary layer. Gilbert et al. [77] emphasized that the new generation DAWTs could provide twice the power output and be 50% cheaper than a conventional wind turbine with the same diameter and same wind speed.

By consequence of these outcomes, DAWTs became economically attractive. However, despite a strong academic interest [55, 72, 121, 127, 128, 193] the commercial exploitation of DAWTs wasn't attempted before 1995. Vortec Energy Limited took the initiation on the development of Vortec 7 DAWT. Based on Foreman's design [149, 150], a prototype was built with a 17.3 meter height and optimization was performed by CFD with a comparison of small scale experiments. The power augmentation was expected to reach about a factor of 9, but the full-scale Vortec 7 achieved only a factor of about 2.4. One of the reasons was that the exit velocity was assumed to be uniform in the calculations. On the contrary, the full-scale model demonstrated high speed regions at the tip and lower at the hub, which reduced the power output [148].

Hansen et al. [90] compared the theoretical expression for the power coefficient as a function of thrust coefficient with CFD computations of a bare turbine and concluded that the actuator disk theory was applicable to model the rotor. Moreover, he confirmed that the Betz limit can be exceed using a diffuser. However, van Bussel [191] emphasized that the calculation of the power coefficient led to an unrealistic power augmentation. He suggested that the power coefficient must be normalized using the maximum shroud area, which reduces the power coefficient to below the Betz limit rather than the rotor area as in a bare wind turbine calculation. Jamieson [108] reformulated the momentum theory to define an optimal power extraction, equal to 0.89 of the power available in the rotor streamtube far downstream.

Another mechanism so-called "flanged diffuser" has been investigated both experimentally and numerically by Abe et al. [1], Abe and Ohya [2], Ohya et al. [140], and Ohya and Karasudani [139]. In this concept, a brim was attached to the exit of diffuser, creating a large scale flow separation. As a consequence of the separation, a low-pressure zone occurs which draws more mass through diffuser compared to a diffuser without a flange. The numerical results obtained by a custom turbulence model, developed and tuned for this purpose, showed an accurate prediction of velocity and pressure profiles in comparison with experimental data [1, 2]. The experimental prototype of "Wind-Lens structure" with a length-to-diameter ratio of 1.47 produces 4-5 times more power than a conventional wind turbine [140]. A new design of a compact brimmed diffuser with a length-to-diameter ratio from 0.1 to 0.371 achieved a power output of 2.5 times larger than a bare diffuser. Several wind turbines have been installed around China to examine the practical application [139] (see Fig. 2.4(a-b)) of this design.

Particle Image Velocimetry measurements were performed by Toshimitsu et al. [189] and Kardous et al. [112] for a diffuser with a flange. Toshimitsu et al. [189] found that the acceleration of the flow is due to the separation vortices behind the flange which led to a power increase of 2.6 times larger than a bare wind turbine. Similarly, Kardous et al. [112] compared several flange heights without the blade and concluded that the wind velocity increases by about 64% to 81% for a diffuser with a flange and 58% for a diffuser without a flange.

A semi-analytical method was developed by Bontempo and Manna [28] and Bontempo et al. [27] to determine an exact solution of an axisymmetric, potential flow using a Green's function. The difficulty of this approach is to determine the turbine loading as a function of a stream function. To overcome this, an iterative approach is applied to obtain the flow-field.

Recently, CFD calculations were performed by Aranake et al. [12, 13] for the same shrouded wind turbine as [27, 28], in order to compare the predictions of the existing low-order models. Later, axisymmetric RANS simulations were performed with an actuator disc model. It is found that the Betz limit is exceed by a factor of 1.43 based on the maximum shroud area [11].

The commercial ``donQi Urban Windmill´´has been developed extensively by the Delft University of Technology (see Fig. 2.4(c)) [184, 192]. This diffuser is an annular wing with the suction side pointing inwards which increases the velocity through the duct. The exit plane is equipped with a gurney flap to enhance the mass flow through the diffuser. Ten Hoppen [184] focused on the effect of the vortex generators placed at the diffuser trailing edge both numerically and experimentally. The aim of the vortex generator is to increase the power output by promoting the turbulent mixing of the wake and the free-stream flow which decreases the exit pressure, hence, the mass flow rate. He found that the power output increased up to 9% by adding the vortex generator. Later, van Dorst [192] performed an analysis of the rotor design on the existing wind turbine to improve the performance. A RANS simulation where the rotor was modelled as an actuator disc showed a good comparison with experiments [56]. An experimental study was performed with a porous screen to observe the turbine loading [181]. It is concluded that the relation between the thrust coefficient of the diffuser and the thrust coefficient of the screen is not linear. Thus, the axial momentum theory is not applicable when there is a high loading. The installation of the gurney flaps was found to be effective for aerodynamic performance [57].

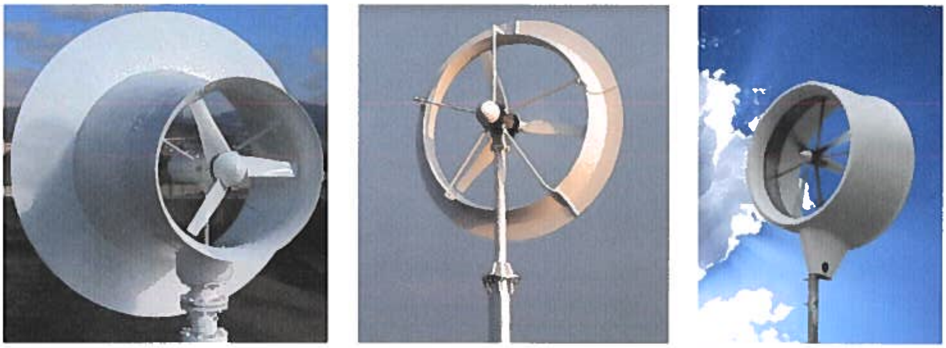

(a) 500W Wind-Lens turbine [139].

(b) 5kW Wind-Lens turbine (compact brimmed) [139].

(c) donQi Urban Windmill [192].

Figure 2.4: Commercial DAWTs.

There is another application that uses the same methodology. In this case, a horizontal axis wind turbine is placed through a building which acts as a duct. An EU funded Wind Energy in the Built Environment project in the framework of the Non Nuclear Energy Programme discussed several options for Building Integrated Wind Turbines (BIWT). They considered three different configurations: a stand-alone wind turbine, a retro-fitting wind turbine onto existing buildings, and fully integrated turbines into a (new) building [35]. A prototype of the latter, called WEB Concentrator (see Fig. 2.5(a)) was designed by performing CFD simulations, wind tunnel testing, and field-testing. It is observed that the performance was enhanced at low-speed [34]. Mertens [131] focused on the retro-fitting and full integration configurations by studying the wind turbine positioning that maximizes the energy output. He found that the most promising configurations are when the wind turbine is located on the roof of the building or in a duct placed through two buildings. Later, Watson et al. [195] performed three dimensional CFD simulations compared with 1D theory of a ducted wind turbine located on the top of the building. He found that the theory provides good results for a standing duct but shows some discrepancies when the building is present.

There are already existing applications of building-mounted ducted wind turbines. The Bahrain World Trade Center has two towers which are connected by skybridges, each has a 225 kW wind turbine with a 29 m diameter (see Fig. 2.5(b)). It was expected to deliver 11% to 15% of the tower energy needs [53]. The Strata Tower in London hosts three five-bladed, 9 m diameter wind turbines integrated into the top part of the building (see Fig. 2.5(c)). Each wind turbine is rated at 19 kW and produce approximately 8% of the building's estimated total energy consumption [3].

(a) WEB Concentrator [34]. (b) The Bahrain World Trade Center[53]. (c) The Strata Tower [3].

Figure 2.5: Existing BIWTs.

Even though in literature extensive studies were performed on the performance of ducted wind turbines, the assessment of noise emission from ducted wind turbines within an urban environment, including the effect of aerodynamic roughness on the inflow conditions is still ongoing. It must be noted that aerodynamic roughness varies depending on the type of terrain and rural structures, which would directly affect the turbulent inflow conditions and the power efficiency. Moreover, similar to the effect of inflow conditions, the siting of wind turbine also plays an important role on the power efficiency. Therefore, different siting positions should also be investigated. However, in the extend of our literature survey, relevant studies are missing in the literature, except only some preliminary experimental [35] and numerical [131, 195], focusing only on the power efficiency.

2.3. WIND TURBINE NOISE

The noise emitted from wind turbines can be divided into two main mechanisms: noise due to the machinery and aerodynamic. The former one is due to the noise generated by the gearbox, generator, cooling fans, and auxiliary equipments such as the oil coolers and hydraulic system for control purposes [151]. However, this noise is less of concern due to techniques such as anti-vibration mountings or acoustic damping of the components [60]. The aerodynamic noise mechanism is due to the interaction of the blade with the air which is considered as the dominant noise source of the wind turbine.

2.3.1. AERODYNAMIC NOISE GENERATION IN GENERAL

Before explaining each mechanism, a brief explanation of aeroacoustic analogies will be emphasized to ease the understanding of the sound generation by low Mach number flows. The aerodynamically generated sound is expressed by Lighthill [122] [123] who rearranged the Navier-Stokes equation to obtain a single wave propagation equation in the absence of external forces. He concluded that for free turbulent flows such as jets, the equivalent sound mechanism can be expressed as a quadrupole whose sound intensity scales with the eighth power of the Mach number (M^8). Later, Curle [51] extended this analogy for unsteady flows interacting with solid surfaces and expressed the sound generation in terms of quadrupole and dipole sources whose strengths are related to the turbulent stress tensor and unsteady forces exerted on the surface, respectively. At low Mach numbers, the sound intensity scales with the sixth power of the Mach number for a compact dipole source (M^6), thus, making it acoustically efficient than a quadrupole source. Finally, Ffowcs Williams and Hawkings (FW-H) [197] further generalized the classical analogy by considering moving surfaces and expressed the generated sound in terms of monopole, dipole and quadrupole sources. Furthermore, this analogy is also suitable for predicting the noise emitted by the rotating machinery [155]. At low Mach number flow applications, it is shown that the quadrupole sources become negligible and the monopole sources appear less effective in acoustic radiation than dipole sources. Accordingly, the unsteady aerodynamic forces on the blade surface is considered to be the main noise source which can be characterize as a dipole [118].

2.3.2. WIND TURBINE AERODYNAMIC NOISE

This noise generation can be divided into three mechanisms; low frequency noise, turbulent inflow noise and airfoil self-noise.

Low frequency noise is the noise emitted by the blade when it encounters a change in wind speed due to the presence of the tower and wind shear. In general, wind turbines have a cylindrical tower shape which creates a potential field around it if the turbine is upwind. When the tower is placed downwind, the flow cannot follow the curvature which leads to flow separations. Thus, depending on the blade being located upwind or downwind, it will experience a change in the angle of attack and the pressure distribution along the blade, which causes rapid change in the blade loading at the blade passage frequencies of the wind turbine. The radiated noise is dependent on the distance and the orientation of the tower and rotor. If the distance between them is larger, the blade will be less affected, resulting in lower noise levels. This noise is also reduced for upstream wind turbines compared with downstream ones, because the potential distortion decays much faster with distance than that due to the viscous wake [82]. Furthermore, the typical blade passage frequency is in the range of 1 Hz - 20 Hz which is less important since this range is below the audible range. However, this low frequency may excite the building structures [194].

Turbulent inflow noise or leading edge noise occurs when the turbulent eddies inside the atmospheric boundary layer interacts with the blade, thereby inducing an unsteady lift and noise. Therefore, the noise generation is altered by the turbulent properties and characteristics of the atmospheric boundary layer. The atmospheric turbulence is generated by two mechanisms; due to interaction of the flow with surface, which is referred to as aerodynamic turbulence, and due to the buoyancy of the air caused by the local heating by the sun which is referred to as thermal turbulence [194]. Additionally, each spatial component of turbulence is generated by different mechanisms. Wind shear drives the longitudinal component of turbulence, which is in the direction of the mean flow, while the vertical component normal to the surface, is affected by both wind shear and buoyancy. The lateral component may be larger than the longitudinal component.

Depending on the size of the eddy compared to the chord of the blade, the mechanism of noise generation is different. At low Mach number, when the eddy size (Λ) is larger than the chord of the blade (c), the whole blade segment will be affected, thus resulting in an acoustic dipole source where its strength is proportional to the sixth power of the relative velocity, U^6. However, if the eddy size is smaller than the chord of the blade, $\Lambda/c \ll 1$, the eddy will produce a local fluctuating pressure on the blade and will not affect the global aerodynamic force on it. Thus, the noise will be radiated at a higher frequency and the source strength will be proportional to the fifth power of the relative velocity, U^5. A sketch given in Fig. 2.6 explains the mechanism. This noise mechanism is considered to be dominant up to 1 kHz and is perceived as a swishing noise, and yet the mechanism has not been fully understood [194].

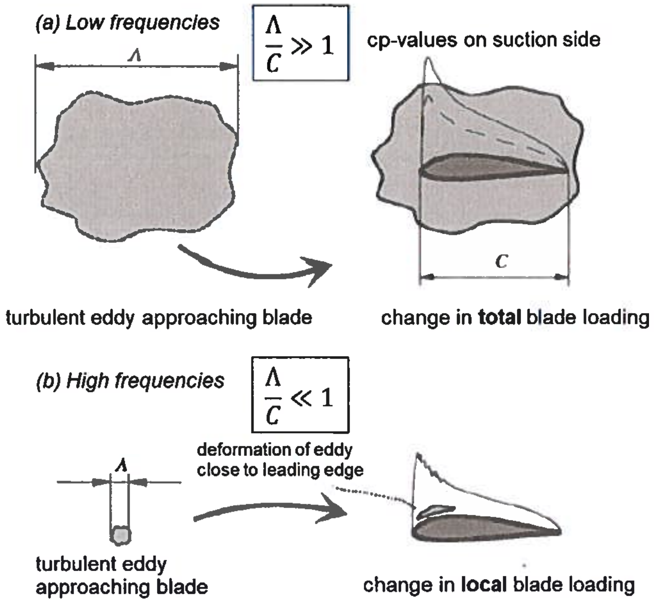

Figure 2.6: Schematic of the turbulent inflow noise depending on the eddy size [194].

Airfoil self-noise noise Airfoil self-noise is generated by the interaction of an airfoil with the turbulence that develops within its boundary layer and wake. According to Brooks et al. [31], this mechanism can be divided to five categories: trailing-edge noise, tip noise, laminar-boundary-layer-vortex-shedding noise (laminar boundary layer instability noise), separated / stalled flow noise, and blunt-trailing-edge noise. These are illustrated in Fig 2.7.

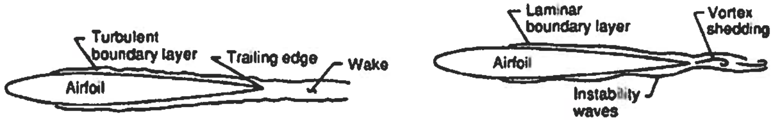

(a) Trailing-edge noise. (b) Laminar-boundary-layer-vortex-shedding noise.

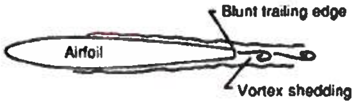

(c) Blunt-trailing-edge noise.

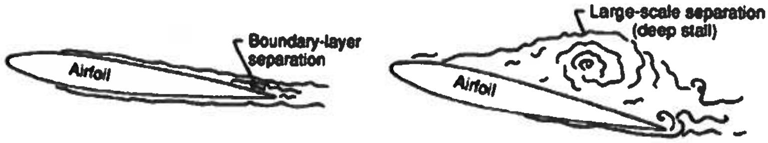

(d) Separated / stall flow noise.

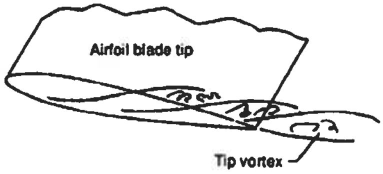

(e) Tip noise.

Figure 2.7: Self-noise mechanism [31].

- Trailing-edge noise is considered as the dominant source for modern wind turbines. The Reynolds number in the outer part of the blade is generally high $Re > 10^6$, thus the turbulent boundary layer developing on the blade surface contains wide range of scales. As the turbulent eddies within the boundary layer passes over the sharp edge, they scatter sound at the trailing-edge to the far-field.

  Trailing-edge noise also radiates a swishing noise reported in [17, 58] due to the combined effects of the directivity and convective amplification due to the rotation of the blades [86]. The demonstration of the directivity patterns with respect to the three different wavelength, which are shown in Fig. 2.8, are performed by Hansen et al. [86], by using Amiet's theory [6]. It is observed that when the airfoil chord (c) is much smaller than the acoustic wavelength (λ) which means that the airfoil is a compact source, the directivity pattern behaves as a dipole. Alternatively, when the airfoil chord is larger than the acoustic wavelength ($c \gg \lambda$), the airfoil acts as a semi-infinite half-plane and the directivity pattern behaves as a cardioid shape. When they are of the same order, the acoustic waves generated at the trailing-edge are also scattered from the leading-edge resulting an upstream-radiating pattern which produces the swishing noise coupled with the rotation of the blades [86]. The perceived noise amplitude will rise when the source approaches to the observer which is found to be the main contribution of the asymmetric radiation pattern for wind turbines [86, 138].

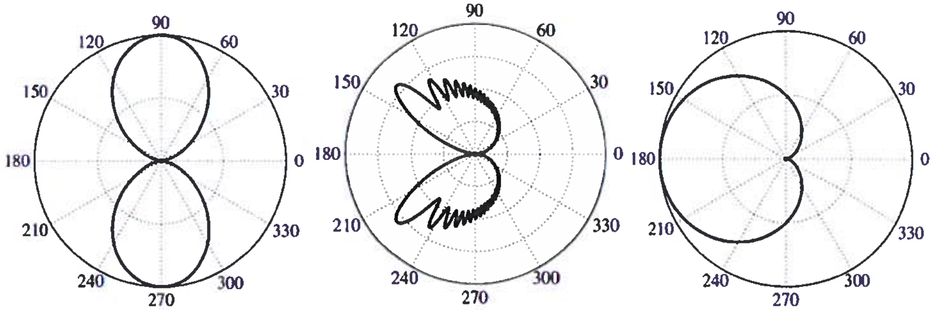

(a) $c/\lambda \ll 1$. (b) $c/\lambda \sim 1$. (c) $c/\lambda \gg 1$.

Figure 2.8: Directivity patterns of trailing-edge noise using the theory of Amiet [6]. The origin is at the trailing edge location and the flow is assumed from left to right; c is chord, λ is wavelength (taken from [86]).

- Laminar-boundary-layer-vortex-shedding noise occurs when the Reynolds number is moderate ($10^5 < Re < 10^6$), the laminar flow region may remain until the trailing-edge. A laminar separation bubble or separated shear layer might cause small perturbations in a laminar boundary layer. The instabilities, which are created by the coherently amplified small perturbations roll up into vortical structure, pass the trailing edge and generate the acoustic waves with the edge interaction. The acoustic wave travelling upstream toward the trailing-edge may trigger the laminar-turbulent transition or the boundary layer instabilities known as Tollmien-Schlichting waves. The pressure disturbances are created by these waves and radiate sound as they pass the trailing-edge. When this feedback loop is generated, high levels of tonal noise is radiated. To avoid this noise mechanism, the boundary layer can be tripped.
- Blunt-trailing-edge noise occurs when the turbulent boundary layer passing by the trailing-edge creates vortex shedding if the airfoil has a sufficient thickness. Therefore, alternating vortices near the wake will create unsteady pressure at the trailing-edge region, resulting in another dipole source.
- Separated / stalled flow noise occurs when the angle of attack is high enough to

separate the flow on the suction side of the airfoil due to the adverse pressure gradient. The separated region of the airfoil consists of large and coherent eddies whose interaction produces noise at a lower frequency but higher amplitude than trailing-edge noise [86]. However, this noise mechanism can be avoided by the pitch-control of wind turbines [29].

- Tip noise mechanism is related to tip vortex formation which is created by the pressure difference due to the three dimensional effect at the tip of the blade. The turbulent flow created in this region has a different nature than the one at the trailing edge since the turbulent boundary layer sweeps into the vortex resulting in a complex three-dimensional flow. Thus, two different sound mechanisms are observed in this case; the turbulence interaction near the tip edge and the turbulence created by the trailing edge vortex as it passes [86].

2.3.3. NUMERICAL NOISE PREDICTION APPROACHES

Trailing-edge noise prediction approaches can be distinguished along three categories; semi-empirical, direct and hybrid methods. The applicability of the semi-empirical models [31] is limited since the models need to be calibrated against experimental data, which can lead to poor prediction for other airfoil profiles and flow conditions [134]. The direct method based on the conventional Navier-Stokes equations [78, 161] as well as the Lattice-Boltzmann method [15, 162], provide accurate and reliable predictions and are applicable for industrial applications. However, when these high-fidelity methods are utilized as a design and optimization tool, they demand high computational cost [92]. Hybrid methods offer an interesting compromise in terms of accuracy vs. CPU cost, by decoupling the flow and acoustic calculations [153]. Hybrid methods usually consist of the following two steps: first, the unsteady flow field is computed in the region of the source term; secondly, an acoustic analogy is used to compute the acoustic source radiation towards the far-field. In order to further reduce the computational cost, Reynolds-Averaged Navier-Stokes (RANS) simulations can be preferred over scale-resolved simulations to provide a source model. In that case, complementary stochastic methods are necessary to synthesize the missing unsteady information about the flow. The Stochastic Noise Generation and Radiation (SNGR) [37, 71, 92] and Random Particle-Mesh (RPM) [70] were developed to this end. Finally, purely statistical methods (not involving any stochastic reconstruction) offer the cheapest solution amongst the hybrid methods. The RANS-based Statistical Noise Model (RSNM) [59] follows this path; the acoustic far-field is computed using a semi-infinite half plane Green's function combined with a model for the turbulent velocity cross-spectrum in the vicinity of the trailing-edge. Alternatively, the wall-pressure based models compute the acoustic far field using a diffraction analogy technique [40] or Amiet's theory [5].

Amiet's theory requires the wall-pressure spectra information which can be obtained directly from Scale-Resolving Simulation (SRS). However, SRS computations require significant computational cost that is unappealing for industrial design and optimization tools. Kraichnan [116] was the first to express the wall-pressure fluctuations for a flat plate based on the solution of the Poisson equation. The method expresses the pressure fluctuations in terms of the two-point correlation of the wall normal velocity fluctuations and the mean velocity profile. Following this approach, the TNO model was developed by Parchen [144], which is based on the turbulent boundary layer and the wall-pressure wavenumber frequency spectrum, where Blake's equation [25] is used for the prediction of the wall-pressure wavenumber frequency spectrum. This model was observed to yield an under-prediction of the noise level compared to some experimental results [22, 111], even though it shows a correct behavior with respect to incoming velocity and angle of attack. Lilley and Hodgson [125] developped an extended version of the Kraichnan [116] method by considering the pressure gradient in the streamwise direction with empirically obtained inputs. Later, Panton and Linebarger [142] expressed these inputs by empirically determined analytical expressions, yet this was insufficient to apply for more complex non-equilibrium turbulent boundary layers. Lee et al. [120] showed that the Kraichnan model is still applicable for more complex flows by obtaining the input parameters through RANS simulations of the reattachment after a backward-facing step. Lately, Remmler et al. [154] applied this technique to zero and adverse pressure gradient flows. Besides simplified theoretical approaches, the development of the semi-empirical relationships has served to describe the pressure fluctuations beneath the boundary layer based on a theoretical basis. These models are derived by fitting the experimental wall-pressure spectra rescaled with the boundary layer variables. From Fig 2.9, four frequency regions are observed when rescaled by different boundary layer variables. Hwang et al. [101] summarized these regions as the low frequency region, the mid-frequency region, the overlap region, and the high frequency region. The low frequency region, $\omega\delta/u_\tau \le 5$, is proportional to ω^2. The mid-frequency region, $5 \le \omega\delta/u_\tau \le 100$, has the peak region which occurs around $\omega\delta/u_\tau = 50$. The universal range or overlap region, $100 \le \omega\delta/u_\tau \le 0.3(u_\tau\delta/\nu)$ is proportional to $\omega^{-(0.7-1.1)}$. The high frequency region, $0.3 \le \omega\nu/u_\tau^2$ varies from ω^{-1} to ω^{-5} where ω is angular frequency, δ is the boundary thickness, u_τ is the friction velocity and ν is the kinematic viscosity.

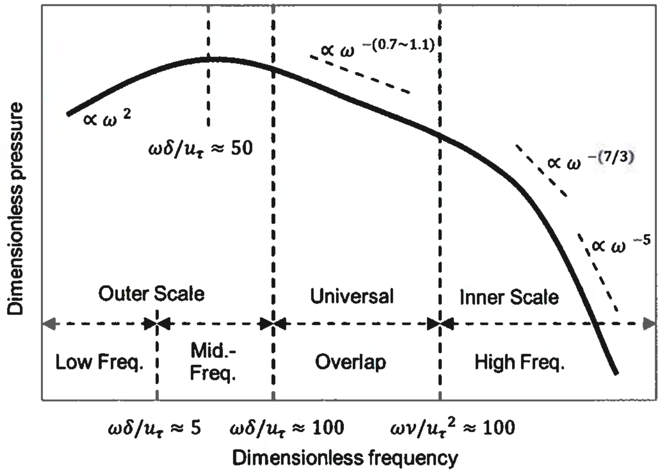

Figure 2.9: General spectral characteristics of a turbulent boundary layer wall-pressure spectrum at various frequency regions with different scaling parameters [101].

The model proposed by Schlinker and Amiet [165] used the external variables to fit the experimental data obtained from Willmarth and Roos [198]. Later, Howe [97] reformulated the wall-pressure model proposed by Chase [41] by re-scaling with the mixed boundary layer variables. The model exhibited better performance by capturing the ω^{-1} decay at high frequencies. However, this model does not take into account the Reynolds number effects where the overlap region increases at the intermediate frequencies. Moreover, this model does not capture the ω^{-5} decay for the highest frequencies. Goody [79] improved this model by adding a term in the denominator which satisfies the decay for high frequencies. He also added a non-dimensional variable that sets the overlap region depending on the Reynolds number. This model and earlier ones perform better for simple flows, however, they exhibit significant differences for Adverse Pressure Gradient (APG) and separated flows. Rozenberg et al. [159] developed the Goody model for APG flow by introducing two additional parameters which are Coles' wake, Π and Clauser's parameters, β_c. Catlett et al. [39] extended the Goody model for APG flows by introducing non-dimensional parameters involving the Reynolds number and the Clauser's parameter. Kamruzzaman et al. [110] proposed another model based on the Goody model by using airfoil measurement data. Hu and Herr [98] claimed that using the shape factor, $H = \delta^*/\theta$, where δ^* is the displacement and θ is the momentum thickness, is more suitable for characterizing APG flows. Moreover, they suggested that the proper scaling for the spectrum should be the dynamic pressure as a better fitting is observed with their experimental data. Later, Lee and Villaescusa [119] extended the Rozenberg model by modifying some of the terms to provide a better universal approach.

In this thesis, several different state-of-the-art wall pressure models, which are being extensively used in far-field trailing edge noise predictions, are tested and their performances are evaluated by two-dimensional RANS simulations for various grid resolutions with respect to an experimental data [92]. Furthermore, among these models, three best performing models are applied to three-dimensional ducted wind turbine simulations. However, the scattering from the diffuser is not taken into account in the present investigation. Nevertheless, based on two-dimensional simulations, an approach is developed to include the effect of diffuser by modifying the inflow conditions. Finally, the performance of this approach with respect to three-dimensional full rotor simulation is assessed.

I

NUMERICAL MODELLING

3

METHODOLOGY

3.1. AMIET'S ANALYTICAL MODEL FOR TRAILING EDGE NOISE

A semi-analytical model is provided by Amiet [8] to compute the broadband trailing-edge noise for an airfoil. Since the model is based on a linearized gust-airfoil response, the airfoil is assumed to have negligible thickness, camber and angle-of-attack (a.o.a). Assuming that the chord is infinite in the upstream direction, the main trailing-edge scattering is obtained as a solution of a Schwartzchild problem [8], which was further extended by Roger and Moreau [156] by applying a leading-edge back-scattering correction to account for finite-chord effects. For a large span airfoil and an observer located in the midspan plane at the acoustical and geometrical far-field position $\mathbf{x} = (x, 0, z)$ for a given angular frequency ω, the acoustic power spectrum density (PSD) can be written as:

$$S_{pp}(\mathbf{x}, \omega) = \left(\frac{\sin\Theta_r}{2\pi R}\right)^2 (kc)^2 \frac{d}{2} |\mathcal{L}|^2 \, l_y(\omega) \, \phi_{pp}(\omega) \tag{3.1}$$

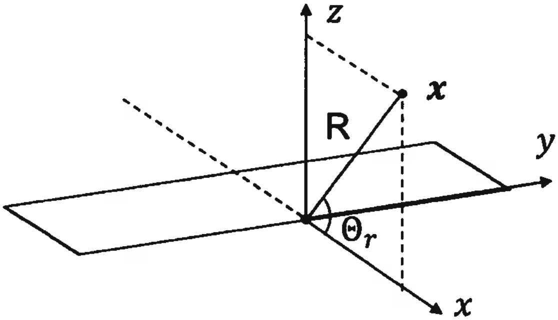

Figure 3.1: Sketch of the observer and source for a flat plate.

where $k = \omega/c_0$ with c_0 the speed of sound, Θ_r is the polar observation angle, R is the distance between source and observer as shown in Fig. 3.1, c is the chord length, d is the span, l_y is the spanwise correlation length, ϕ_{pp} is the wall-pressure spectrum, $\mathcal{L} = \mathcal{L}_1 + \mathcal{L}_2$ is the aeroacoustic transfer function [156] for the main contribution term from the trailing-edge, $\mathcal{L}_1$, and the leading edge back-scattering term, $\mathcal{L}_2$. The Corcos [49] model is used to compute the spanwise correlation length as:

$$l_y(\omega) = \frac{bU_c}{\omega} \tag{3.2}$$

where U_c is the convection velocity and b is a parameter of the model. As the focus here is placed on the sensitivity of the wall-pressure spectrum, both the convection velocity and spanwise correlation length are assumed constant. In this instance, the values $U_c/U_\infty = 0.7$ and b = 1.47, reported in Ref. [159], respectively, have been adopted. More accurate models accounting for some frequency dependence have been developed, such as proposed by Efimtsov [69] for the spatial correlation, and Smolyakov [172] for the convection velocity, but haven't been considered in this work.

3.2. THE DOPPLER EFFECT

The trailing-edge noise prediction for an isolated airfoil mentioned in the previous section can be extended for wind turbines by dividing the blade into n segments and taking into account the rotation. Based on the analysis of Lowson [129], Amiet [7] discussed that a dipole source in a circular motion can be approximated as a rectilinear motion if the angular velocity (Ω_{rot}) is much smaller than the source frequencies (ω). In this case, the acceleration of the source in the direction of the observer is negligible. Initially, the analytical formulation was developed by Schlinker and Amiet [165] for a high-speed low-solidity helicopter blade and later, extended for low Mach number rotor blades [133] operating in a medium at rest.

The sound frequency at the observer location, ω_0 is shifted compared to the emitted frequency from the source, $\omega_e(\Psi)$ where $\Psi = \Omega_{rot}t$ is the azimuthal angle. The ratio between is known as the Doppler shift and is given by [133]:

$$\frac{\omega_e}{\omega_0} = 1 + M_t \sin\Psi \sin\Theta \tag{3.3}$$

where $M_t = \Omega_{rot} r/c_0$ is the Mach number of the source relative to the observer, respectively. The observer is placed at the XZ plane with a distance of R_0 and an angle of Θ as shown in Fig. 3.2. The far-field noise should be determined by averaging all the possible azimuthal positions of the blade segments and weighting it with the Doppler factor. The formulation is given for a rotating machine with B independent blades and low-solidity, thus the blade to blade interaction can be assumed negligible:

$$S_{pp}(X,Y,Z,\omega_0) = \frac{B}{2\pi}\int_0^{2\pi}\left(\frac{\omega_e}{\omega_0}\right)^n S_{pp}^{\Psi}(x,y,z,\omega_e)\,\mathrm{d}\Psi \tag{3.4}$$

where S_{pp}^{Ψ} is the noise emitted from a source located at Ψ neglecting the Doppler effect and is thus the same as the isolated airfoil given in Eq. 3.1. The exponent n is defined as 1 for instantaneous spectrum and 2 for the time averages spectrum [170, 171].

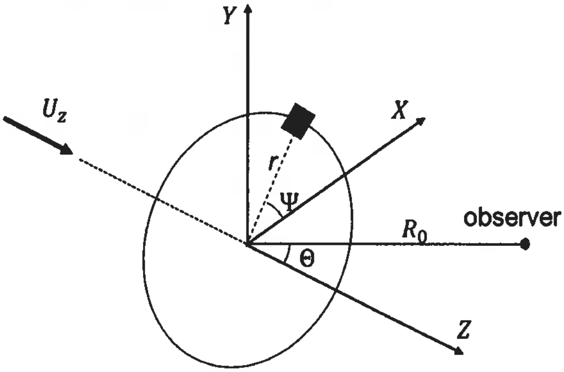

Figure 3.2: Sketch of the observer and source for a rotating machine.

3.3. COORDINATE TRANSFORMATION

To calculate the acoustic field of a blade strip by using the isolated airfoil theory, the reference frame has to be attached to the strip. Thus, a coordinate transformation is necessary from the observer position (X, Y, Z) to the blade strip location (x, y, z) by taking into account the blade geometry. The same transformation used in [158] is explained in the following section and shown in Fig. 3.3.

The source is positioned at S which is the midspan of a blade strip located at r, whose local coordinate system is defined as x, y, z which are chordwise, spanwise and wall-normal components, respectively. The first transformation is applied from the fixed coordinate system (X, Y, Z) to the angular position of the midspan of the blade strip by keeping the origin fixed as Z=W. The coordinate system at this region is defined as (U, V, W) where U is the coordinate system that passes through the trailing-edge of the blade strip midspan. Thus, the transformation can be performed as the following:

$$\begin{pmatrix} U \\ V \\ W \end{pmatrix} = \mathcal{M}_{UVW\rightarrow XYZ} \begin{pmatrix} X \\ Y \\ Z \end{pmatrix} = \begin{pmatrix} \cos\Psi & \sin\Psi & 0 \\ -\sin\Psi & \cos\Psi & 0 \\ 0 & 0 & 1 \end{pmatrix} \begin{pmatrix} X \\ Y \\ Z \end{pmatrix}$$

The second transformation is performed with an angle ζ to shift the center of rotation to the trailing-edge at the midspan:

$$\begin{pmatrix} u \\ v \\ w \end{pmatrix} = \mathcal{M}_{uvw\rightarrow UVW} \begin{pmatrix} U \\ V \\ W \end{pmatrix} = \begin{pmatrix} \cos\zeta & \sin\zeta & 0 \\ -\sin\zeta & \cos\zeta & 0 \\ 0 & 0 & 1 \end{pmatrix} \begin{pmatrix} U \\ V \\ W \end{pmatrix}$$

To take into account the pitch angle β, another transformation is applied from (u, v, w) to (m, n, p):

$$\begin{pmatrix} m \\ n \\ p \end{pmatrix} = \mathcal{M}_{mnp\rightarrow uvw} \begin{pmatrix} u \\ v \\ w \end{pmatrix} = \begin{pmatrix} 0 & -\cos\beta & -\sin\beta \\ 1 & 0 & 0 \\ 0 & -\sin\beta & -\cos\beta \end{pmatrix} \begin{pmatrix} u \\ v \\ w \end{pmatrix}$$

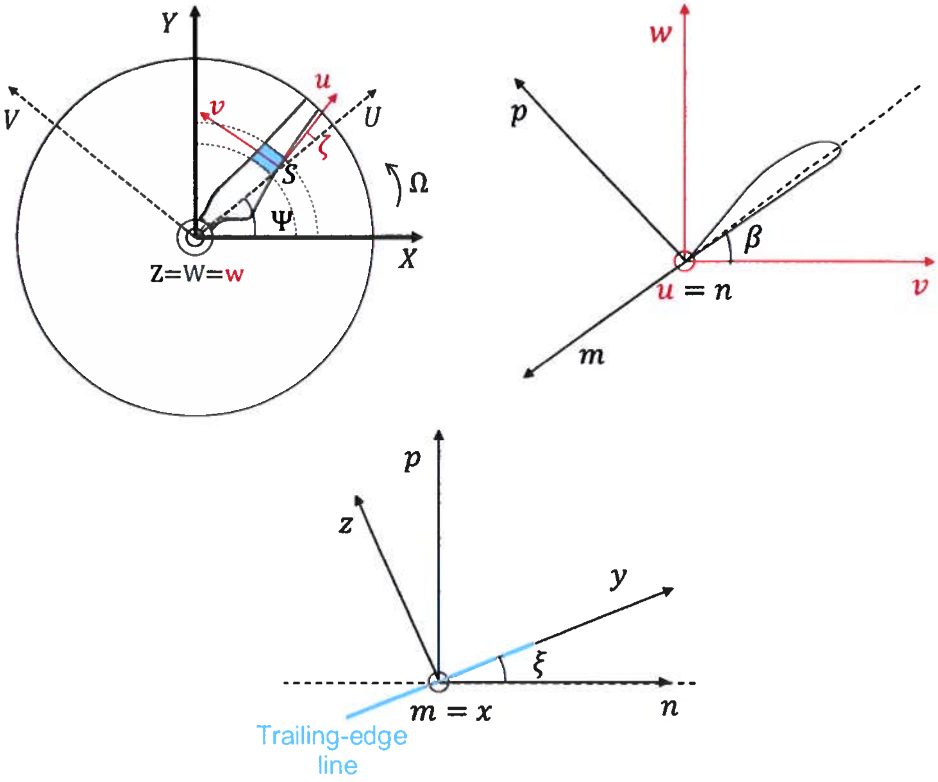

Figure 3.3: Sketch of the transformation matrices.

A final transformation is performed by considering the twist angle ξ from (m, n, p) to (x, y, z):

$$\begin{pmatrix}x\\y\\z\end{pmatrix} = \mathcal{M}_{xyz\to mnp}\begin{pmatrix}m\\n\\p\end{pmatrix} = \begin{pmatrix}1&0&0\\0&\cos\xi&\sin\xi\\0&-\sin\xi&\cos\xi\end{pmatrix}\begin{pmatrix}m\\n\\p\end{pmatrix}$$

The observer position can be transformed to the blade strip coordinate system defined in Sec. 3.1:

$$\begin{pmatrix}x\\y\\z\end{pmatrix} = \mathcal{M}_{xyz\to UVW}\begin{pmatrix}-r\\0\\0\end{pmatrix} + \mathcal{M}_{xyz\to XYZ}\begin{pmatrix}R_0\sin\Theta\\0\\R_0\cos\Theta\end{pmatrix}$$

3.4. WALL PRESSURE SPECTRUM MODELS

Amiet's theory requires the wall-pressure spectrum upstream of the trailing-edge, which can be obtained directly from any resolved-scale simulations. However, the computational cost is demanding since a long time signal is needed to have a sufficient convergence for the low frequencies, and also due to the mesh size and numerical schemes that are required for the high frequencies in particular. Therefore, this section presents models which are governed by the boundary layer profiles that can be obtained from RANS simulations. The first two approaches are based on fitting the experimental wall pressure spectra rescaled with the boundary layer variables. The last one is based on reconstructing the wall-pressure fluctuations by integrating the Poisson equation for pressure. Semi-empirical wall-pressure spectrum (WPS) models often have the form [39, 98, 119]:

$$\frac{\phi_{pp}}{\phi^*} = \frac{a(\omega^*)^b}{[i(\omega^*)^c + d]^e + [fR^g\omega^*]^h}. \tag{3.5}$$

The shape of the spectra is modified through the parameters $a-h$ given in Eq. (3.5). The overall amplitude of the spectra is altered by a. The slopes corresponding to different frequencies are adjusted by the parameters b, c, e and h. The parameter b determines the slope at low frequencies. The overlap region is modified by the parameters b, c and e. The high slope region is adapted by the parameters b and h. The onset of the transition between the overlap and high frequency region is adjusted by the parameters f and g in combination with timescale ratio R. The location of the low-frequency maxima is weakly dependent on the parameter d. Lastly, the parameter i is 1.0 for all except the Rozenberg model. For that model, a constant of 4.76 is introduced when the boundary layer thickness is replaced by the displacement thickness by assuming $\Delta = \delta/\delta^* = 8$. The scaling factor for the spectrum is ϕ^* and for the frequency it is ω^*.

In this work six different semi-empirical wall-pressure spectrum models are investigated: Goody, Rozenberg, Catlett, Kamruzzaman, Hu & Herr and Lee. The parameters and the scaling factors are summarized in Table 3.1 excepted for the Lee model that is an extension of the Rozenberg model. In the following section, the governing variables and the spectral behavior of each model are discussed.

3.4.1. SEMI-EMPIRICAL MODELS

Goody model

The Goody model extends the overlap region by introducing the timescale ratio, R_T, which accounts for Reynolds number effects for Zero Pressure Gradient (ZPG) boundary layers. The wall-pressure spectrum is scaled by mixed variables: δ is the boundary layer thickness, U_e is the velocity at the edge of the boundary layer, and τ_w is the wall shear stress. The timescale ratio is defined as the ratio of the outer time scale to the inner time scale, $R_T = (\delta/U_e)/(\nu/u_\tau^2)$ where u_τ is the friction velocity and ν is the kinematic viscosity. The frequency is scaled by δ/U_e. The spectrum has a slope of ω^2 at low frequencies. It decays with a slope of $\omega^{-0.7}$ at mid-frequencies and ω^{-5} at high frequencies. This model is accurate over a wide range of Reynolds numbers [101]. Furthermore, it is considered as a basis for the Adverse Pressure Gradient (APG) wall-pressure spectrum models.

Rozenberg model

Rozenberg et al. [159] proposed a wall-pressure model based on the Goody model by considering the variations between ZPG and APG flows. Firstly, the scaling factor for both spectrum and frequency was replaced by the displacement thickness, δ^*, instead of the boundary layer thickness, δ, since the former was found to be more accurate. Secondly, the scaling for the pressure fluctuations was changed to the maximum shear stress along the normal distance, τ_{max}. In addition, to characterize the effect of the APG, three parameters are defined: Zagarola-Smits' parameter [200], $\Delta_* = \delta/\delta^*$, the Clauser equilibrium parameter [46], $\beta_c = (\theta/\tau_w)(dp/dx)$, where θ is the momentum thickness, and the Coles wake parameter [47], Π. It is found that Zagarola-Smits' defect law provides a better collapse than the defect law and exhibits an auto-similarity of the velocity profile for the outer region. Thus, Zagarola-Smits' parameter, $\Delta_* = \delta/\delta^*$, is chosen as a driving parameter for the APG. β_c is used to quantify the local pressure gradient even though the tested boundary layers were non-equilibrium flows. Π represents the large-eddy structures in the outer region of the turbulent boundary layer. Coles [47] modified the law of the wall with an additional wake parameter as:

$$u^+ = \frac{1}{\kappa}\ln(y^+) + C + \frac{2\Pi}{\kappa}\sin^2\left(\frac{\pi}{2}\frac{y}{\delta}\right) \tag{3.6}$$

where $u^+ = u/u_\tau$, $y^+ = yu_\tau/\nu$, $\kappa = 0.41$ is the von Karman constant, $C = 5.1$ and the Coles' wake parameter, Π, can be obtained by solving the following implicit equation numerically:

$$2\Pi - \ln(\Pi + 1) = \frac{\kappa U_e}{u_\tau} - \ln\left(\frac{\delta^* U_e}{\nu}\right) - \kappa C - \ln\kappa. \tag{3.7}$$

Alternatively, Π can be estimated through an empirical formula proposed by Durbin and Reif [67]:

$$\Pi = 0.8(\beta_c + 0.5)^{3/4}. \tag{3.8}$$

It is pointed out that Δ_* and Π are influenced by the boundary layer history whereas β_c is a local parameter. As Δ_* decreases, the amplitude of the spectrum increases at mid and high frequencies and decreases for low frequencies. β_c and Π are correlated; when they increase, the peak amplitude gets higher and the slope of the overlap region gets steeper.

Catlett model

Catlett et al. [39] developed a new empirical approach for APG boundary layers based on the Goody model by testing three different trailing edge configurations for a flat plate. The scaling factor for the wall-pressure spectrum and frequency are kept the same as Goody's model. Similar to the Rozenberg model, the local pressure gradient is defined in the form of the Clauser equilibrium parameter, β_c. However, the length and pressure are scaled with outer boundary layer variables, $\beta_\delta = \frac{\delta}{q}\frac{dP}{dx}$ where $q = 0.5\rho U_0^2$ is the dynamic pressure and U_0 is the local free-stream velocity. They found that when the parameters a and $c - h$ are plotted as a function of $\beta_{\delta,\Delta} Re_{\delta,\Delta}$ or $\beta_\delta H$, they fit into a power-law function. Δ is the Rotta-Clauser parameter [46, 157] defined as $\Delta = \delta^*\sqrt{(2/C_f)}$, $C_f = \tau_w/q$ is the skin friction coefficient, $Re_{\delta,\Delta} = \frac{(\delta,\Delta)U_e}{\nu}$ are the Reynolds numbers and $H = \delta^*/\theta$ is the shape factor. Contrary to all the semi-empirical models investigated in this study, the boundary layer thickness is deduced by a percentage of the turbulent kinetic energy,

$TKE(y=\delta) = 0.0002U_0^2$ [164].

Kamruzzaman model

Kamruzzaman et al. [110] modified the Goody and Rozenberg models to present a new wall-pressure spectrum model for the airfoil trailing-edge noise prediction. Various airfoils with different angles of attack and Reynolds number were used to develop the model. They perform the same scaling factors for the normalization of the wall-pressure spectra and frequency as in the Rozenberg model except that τ_{max} is replaced with τ_w. The spectral amplitude for all frequencies are modulated by the parameter a which is a combination of β_c, Π and H while the rest of the parameters are kept constant by fitting to the experimental data. Furthermore, the definition of R_T is modified to $R_T^{'} = \frac{\delta^* u_\tau^2}{U_e \nu}$, to account for the boundary layer loading effects. The β_c parameter is obtained by a curve-fit proposed by Nash [136]:

$$G = 6.1\sqrt{\beta_c + 1.81} - 1.7, \quad \text{where} \quad H = \left(1 - \frac{G}{\lambda}\right)^{-1} \quad \text{with} \quad \lambda = \sqrt{2/C_f}. \tag{3.9}$$

Finally, the Coles wake parameter is computed from Eq. 3.8 which is the same way as in the Rozenberg model.

Hu & Herr model

Hu and Herr [98] developed a new model based on the Goody model by measuring the unsteady pressure fluctuations on a flat plate. The adverse and favorable pressure gradients were created by a NACA0012 airfoil set at different angles of attack. Contrary to the other models, they argued that the scaling factors for the wall-pressure spectra, $\frac{u_\tau}{q^2\theta}$ and the frequency, $\frac{\omega\theta}{U_0}$ are more suitable for APG flow. As a consequence, a better agreement is observed when the timescale ratio, R_T, is replaced by Re_τ. Moreover, it is acknowledged that the boundary layer profile is a main driving parameter for the wall-pressure fluctuations. Thus, the spectral slope at medium frequencies is characterized by the shape factor H, rather than the form of a Clauser's equilibrium parameter β, which fails at accounting for rapid pressure gradient alterations. Lastly, it is explained that the low frequency slope, ω^2, does not hold in the case of non-frozen turbulence and is better modelled using $b = 1.0$. They also pointed out that the turbulence-turbulence term in the Poisson equation gains importance over the mean-shear source term and exhibits a plateau at low frequencies.

Lee model

Lee and Villaescusa [119] suggested an extended version of the Rozenberg model to provide an accurate prediction for extensive applications. For convenience, the scaling factor used in the normalization of the spectra, τ_{max} is replaced by τ_w while keeping the other scaling parameters the same. They found that the Rozenberg model performs an early transition from the overlap region to high frequency region. Furthermore, at high frequencies for zero and low pressure gradient flows, a rapid decay rate is observed. To overcome this, the parameter h is modified as follows:

$$h = \min(5.35, 0.139 + 3.1043\beta_c, 19/\sqrt{R_T}) + 7, \tag{3.10}$$

and if h is equal to 12.35, the following expression is used:

$$h = \min(3, 19/\sqrt{R_T}) + 7. \tag{3.11}$$

The Rozenberg model exhibits higher amplitudes at low and mid-frequencies for low pressure gradient flows. Thus, the parameter d at the denominator is modified as $d = \max(1.0, 1.5d)$ if $\beta_c < 0.5$ to alter the trend. It should be noted that the parameter d in the calculation of the parameter a is kept as in the original model. Lastly, a correction is suggested for the parameter a to adjust the amplitudes for high β as $a^* = \max(1, (0.25\beta_c - 0.52)a)$.

Table 3.1: The parameters and scaling factors for the semi-empirical models

	Goody	Rozenberg	Catlett	Kamruzzaman	Hu & Herr
a[1]	3.0	$\left[2.82\Delta_*^2(6.13\Delta_*^{-0.75}+d)^e\right]$ $\times\left[4.2\left(\frac{\Pi}{\Delta_*}\right)+1\right]$	$e^{7.98(\beta_\Delta Re_\Delta^{0.35})^{0.131}-10.7}+3.0$	$0.45\left[1.75(\Pi^2\beta_c^2)^m+15\right]$ $m=0.5\left(\frac{H}{1.31}\right)^{0.3}$	$(81.004d+2.154)\cdot 10^{-7}$
b	2.0	2.0	2.0	2.0	1.0
c	0.75	0.75	$20.9(\beta_\delta Re_\delta^{0.05})^{2.76}+0.912$	1.637	$1.5(1.169\ln(H)+0.642)^{1.6}$
d	0.5	$4.76\left(\frac{1.4}{\Delta_*}\right)^{0.75}[0.375e-1]$	$0.328(\beta_\Delta Re_\Delta^{0.35})^{0.310}+0.397$	0.27	$10^{-5.8\cdot 10^{-5}Re_\theta H-0.35}$
e	3.7	$3.7+1.5\beta_c$	$-1.93(\beta_\delta Re_\delta^{0.05})^{0.628}+3.872$	2.47	$1.13/(1.169\ln(H)+0.642)^{0.6}$
f	1.1	8.8	$-2.57(\beta_\delta Re_\delta^{0.05})^{0.224}+2.19$	$1.15^{-2/7}$	7.645
g	-0.57	-0.57	$38.1(\beta_\delta H^{-0.5})^{2.11}-0.5424$	-2/7	-0.411
h	7	$min(3,19/\sqrt{R_T})+7$	$0.797(\beta_\Delta Re_\Delta^{0.35})^{0.0724}+7.310$	7	6
i	1.0	4.76	1.0	1.0	1.0
R	R_T	R_T	R_T	R_T'	R_τ
ϕ^*	$\tau_w^2\delta/U_e$	$\tau_{max}^2\delta^*/U_e$	$\tau_w^2\delta/U_e$	$\tau_w^2\delta^*/U_e$	$q^2\theta/u_\tau$
ω^*	$\omega\delta/U_e$	$\omega\delta^*/U_e$	$\omega\delta/U_e$	$\omega\delta^*/U_e$	$\omega\theta/U_0$

[1] The parameter a in the Lee and Villaescusa [119] model is replaced by a^*.

3.4.2. THE INTEGRAL MODEL

As an alternative to the previously described models, the following statistical model proposed by Panton and Linebarger [142] and later by Remmler et al. [154] is also used in the present paper. The incompressible Navier-Stokes equation is reformulated in the form of a Poisson equation for pressure to express the wall-pressure fluctuations beneath the turbulent boundary layer. With the assumption of statistically stationary and homogeneous flow in the streamwise and spanwise directions, the Poisson equation can be solved by using a Green's function technique as:

$$\phi(k_1) = 8\rho^2 \int \int \int_0^\infty \frac{k_1(\omega)^2}{|k|(\omega)^2} \mathrm{e}^{-|k|(\omega)(y+\tilde{y})} S_{22}(y,\tilde{y},\omega) \frac{\partial\langle U_1\rangle}{\partial y} \frac{\partial\langle U_1\rangle}{\partial \tilde{y}} \mathrm{d}y \mathrm{d}\tilde{y} \mathrm{d}k_3 \tag{3.12}$$

where $|k| = \sqrt{k_1^2 + k_3^2}$, U_1 is the streamwise velocity and y is the wall normal direction. The energy spectrum of the vertical velocity fluctuations S_{22} is given as:

$$S_{22}(y,\tilde{y},\omega) = \frac{\overline{u_2'}(y)\overline{u_2'}(\tilde{y})}{\pi^2} \Lambda^2 \int \int_0^\infty R_{22} \cos(\alpha \tilde{k}_1(\omega) \tilde{r}_1) \cos(\alpha \tilde{k}_3 \tilde{r}_3) \mathrm{d}\tilde{r}_1 \mathrm{d}\tilde{r}_3 \tag{3.13}$$

where $\overline{u_2'}$ is the root mean square of the wall-normal velocity fluctuations, Λ is the integral length scale and α is the scale anisotropy factor which is the ratio of streamwise to spanwise turbulent length scales which is defined by Remmler et al. [154] as:

$$\alpha = \begin{cases} 3, & k_1\delta < 1 \\ 0, & 1 \le k_1\delta \le 5 \\ 1, & k_1\delta < 5 \end{cases} . \tag{3.14}$$

The velocity correlation function R_{22} is modeled according to Panton & Linebarger [142]:

$$R_{22} = \left[1 - \frac{\tilde{r}^2}{2\sqrt{\tilde{r}^2 + \tilde{y}^2}}\right] \mathrm{e}^{-\sqrt{\tilde{r}^2 + \tilde{y}^2}} \tag{3.15}$$

with $\tilde{r}^2 = \tilde{r_1}^2 + \tilde{r_3}^2$. Non-dimensionalisation of the integration coordinates and the wave numbers was performed by the integral length scale, $\tilde{r}_i = r_i/\Lambda$, $\tilde{k}_i = k_i\Lambda$ and $\tilde{y} = (y - \hat{y})/\Lambda$. The five dimensional integration in Eq. (3.12) is performed with a Monte Carlo method using importance sampling for enhancing convergence to reduce the computational cost of the numerical integration of the fivefold integration. The reader is referred to Ref. [154] for further details on the Monte Carlo method.

The vertical velocity fluctuations cannot be obtained from the $k-\omega$ turbulence model which assumes isotropic turbulence. However, the measurements performed by Klebanoff [113] for a zero pressure gradient boundary layer demonstrate that the velocity fluctuation components, $\overline{u'}^2_i$, are not constant fractions of $2k$. He proposed an anisotropy factor for each component as $\beta_i = \overline{u'}^2_i/(2k_t)$ where β_i is a non-universal parameter depending on the types of boundary-layer flows. As a first approximation, Remmler et al. [154] proposed to use an anisotropy factor, which is obtained from a flat plate boundary layer simulation using a Reynolds stress transport model in which the velocity fluctuation components can be obtained directly.

Panton & Linebarger have specified the length scale, Λ, as 1.5 times the Prandtl mixing length, l_m, $\Lambda = 1.5 l_m$ which can be calculated as $l_m = LC_m$ where L is the turbulence length scale. C_m is a turbulence model constant and was chosen as 1.9 for the $k-\Omega$ SST [154]. The turbulence length scale, L, can be computed directly from the numerical simulations in which the turbulence model provides the turbulent kinetic energy and turbulent dissipation rate as:

$$L = C_\mu \frac{k_t^{3/2}}{\epsilon}. \tag{3.16}$$

C_μ is given as 0.09 and the turbulent dissipation, ϵ, is calculated as $\epsilon = k_t \cdot \omega$.

The crucial parameters for the semi-empirical models are the boundary layer thickness, δ, the boundary layer edge velocity, U_e, the wall-shear stress, τ_w and the friction velocity, U_τ, which are the only variables in the Goody model. All the other non-dimensional parameters can be derived from the boundary layer variables. In addition, the Rozenberg, Kamruzzaman and Lee models used the Coles' wake parameter, Π and the Clauser equilibrium parameter, β_c. Similarly, Catlett used a form of the Clauser parameter in their model. The appeal of these approaches is that only the velocity profile normal to the surface is needed. In addition to the velocity profile, the Panton & Linebarger model requires the turbulent kinetic energy and the specific dissipation profiles.

3.5. COUPLING WITH CFD

The wall-pressure models require a description of the turbulent boundary layer at the trailing-edge which can be obtained by a panel method coupled with an integral boundary layer formulation as in the XFOIL software [61] or through a RANS simulation. The first approach is found to be rapid and accurate at low Reynolds number [167] and has been used for wind turbine [22, 186] trailing-edge noise applications. The global turbulent boundary layer variables (except the boundary layer thickness) can be obtained directly as an output, and the boundary layer thickness and velocity profile along the wall-normal direction are approximated. In contrast, the latter approach provides the turbulent boundary layer profile in which the required variables can be derived from RANS simulations. Since the prediction of the wall-pressure spectrum depends on the turbulent boundary layer just upstream of the trailing edge, it is important to correctly simulate the physics and determine the adequate mesh resolution for the turbulence model to increase the accuracy [44]. This numerical procedure has proved to be successful for low-speed fan applications [154, 159]. In this thesis, this approach is further extended for wind turbine applications.

The coupling between the RANS simulation and the acoustic prediction is given in Fig. 3.4. After performing the RANS simulations, the BATMAN (Broadband And Tonal Models for Airfoil Noise) in-house code of the von Karman Institute for Fluid Dynamics (VKI) is used to perform the acoustic part. The BATMAN code is based on MATLAB and Python routines. The *VisualizationToolkit* [166] libraries in Python are used to read,

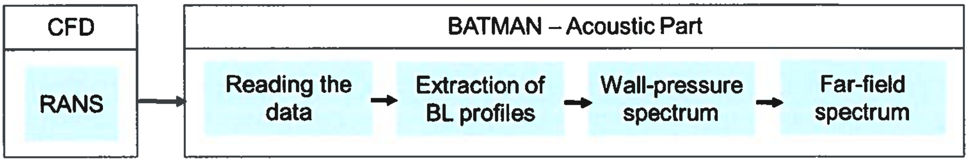

Figure 3.4: Schematic of the coupling between the acoustic part and CFD.

modify and perform the necessary operation on the blade obtained from a geometry or the RANS data in order to extract the boundary layer characteristics. Then, from a given boundary layer profile input, it computes the wall-pressure spectrum based on the selected model and the corresponding far-field spectrum using Amiet's theory.

3.5.1. RANS APPROACHES FOR WIND TURBINES

The general methodology for wind turbine performance is to use a Blade Element Momentum (BEM) model which is based on 1D momentum theory by discretizing the blade into annular sections. In general, the experimental data for a stationary airfoil is used to calculate the lift and drag coefficients as a function of angle of attack (a.o.a) and the Reynolds number. Even though this method is widely used due to its simplicity, it is unable to predict the off-design conditions [68] and high a.o.a at stall conditions due to lack of reliable experimental data [87, 89, 185]. Alternatively, the panel method and 2D RANS simulation mentioned in Sec. 3.5 can be used as an input for this method. However, amongst them only 2D RANS simulation can provide a boundary layer profile as an output for the wall-pressure spectrum models. For 2D RANS modelling, the $k-\Omega$ SST turbulence model proposed by Menter [130] was proven to perform better than other models for flows with strong pressure gradients [38, 117, 190], including flows around isolated wings [83, 173]. However, all the aforementioned methods are based on a stationary 2D airfoil which disregards 3D flow around the tip and hub as well as the rotational effects.

The 3D flow and rotational effects have been noticed by Himmelskamp [94] through experimental investigations of a rotating propeller. It is observed that the rotating blades experience stall at a higher a.o.a than the equivalent 2D airfoil section resulting in a higher lift which is known as rotational augmentation. In literature, several explanations have been proposed to explain this phenomenon; however the discussion remains open. Carcangiu et al. [36] suggest that the centrifugal force induced a radial velocity. Coriolis forces couple with this radial component and act as a favorable pressure gradient in the chordwise direction and thus delay the separation point toward the trailing edge. However, both effects are found to be smaller at the outward region [43, 168]. To take into account the rotational effect, the correction factors for lift and/or drag coefficients are proposed by Snel at al [85], Du & Selig [62, 63], Chaviaropoulos & Hansen [43], Lindenburg [126] and Dumitrescu & Cardos [65, 66]. Alternatively, another correction based on the pressure coefficient is proposed by Bak et al. [16].

3D wind turbine simulations can be handled under different modelling approaches depending on the complexity and the flow properties under investigation. When the rotating part is considered in a moving reference frame, the problem can be modelled as a steady-state problem. In this case, the moving parts can be solved in the rotating reference frame by accounting for the centrifugal and Coriolis force source terms in the momentum equation. A **Single Reference Frame** (SRF) can be used if the entire computational domain rotates with the same speed with respect to a specified single axis. The **Multiple Reference Frame** (MRF) method is a steady-state approach in which the cell zones can be assigned at different rotational or translational speeds. The moving cell zones are solved in the rotating frame while the stationary cell zones are solved in the stationary frame. In this approach, the flow information passes directly between the subdomains which means that the relative motion between the moving zone with respect to the adjacent domain is not considered. This method is also referred to as a ``frozen rotor approach´´since the rotor is fixed in a specific location and the instantaneous flow field is observed. When the unsteady interaction between the moving and stationary part is of interest, a **Sliding Mesh Method** (SMM) can be implemented to capture the transient phenomena. The sliding mesh method is the most accurate amongst these methods to simulate the multiple rotating reference frames, but it is demanding in terms of computational cost [187]. Since the mean boundary layer profiles are needed in order to predict the wall-pressure spectrum, the MRF method has been chosen for the 3D simulation.

For the turbulence model, as it is stated by Tachos et al. [180], the $k-\Omega$ SST turbulence model performs better than the Spalart-Allmaras [175] and Renormalization Group (RNG) k-ϵ [199] models for the NREL Phase VI rotor blade. Moreover, it has been found in the literature that this model has been used extensively for wind turbines [81, 135, 143, 174].

It should be also taken into consideration that the RANS models are based on the Boussinesq approximation, which assumes isotropic flow even though the flow is mostly anisotropic. Moreover, the viscosity within the boundary layer is over-predicted, which tends to artificially delay separation.

3.5.2. 3D AND 2D RANS APPROACH FOR FAR-FIELD NOISE OF A WIND TURBINE

This section describes the coupling of RANS simulations and the far-field acoustic calculation. As a first step, the 3D simulation of a wind turbine will be performed with the $k-\Omega$ SST turbulence model using the MRF method. Next, the RANS data will be read by the BATMAN in-house code. Then, the blade will be divided into equidistant strips and the midspan of each section will be identified. The boundary layer profiles; the mean axial velocity, the turbulence kinetic energy and the specific dissipation rate are extracted at a specified point near the trailing-edge normal to the blade surface on the midspan location. By obtaining the boundary layer profiles, the wall-pressure spectrum (ϕ_{pp}) can be predicted at each strip location. For the far-field noise prediction, each strip is approximated as a flat plate to obtain linearized strips, then the acoustic transfer function is calculated at the observer position. This will be performed for sufficient azimuthal positions for each strip locations and averaged.

The drawback of this approach is the time it takes to obtain a reliable simulation and the post-processing of a 3D geometry. To this end, a 2D approach similar to BEM is proposed as a simplification. The 3D and rotational effects are neglected in this case, which leads to obtain isoradius blade cuts. Therefore, from the geometry file, the blade can be divided into several isoradius cuts to obtain the same relative velocity for the 2D simulation. However, as the blade cut is performed at a certain radius from the center, the obtained blade cuts are not planar but rather a curved surface. To obtain a planar surface, the unwrapping process shown in Fig. 3.5 is applied. At each strip location (n), the blade is cut with a cylinder having a radius of R_n. The angle α_{mn} is calculated for each point (m), x_{mn}, y_{mn}, z_{mn}, which is obtained by the intersection of the cylinder with blade. Then, each new point location is found and projected on to the yz plane for 2D simulations $(x'_{mn}, y'_{mn}, z'_{mn} = (R_n\alpha_{mn}, z_{mn}, 0))$.

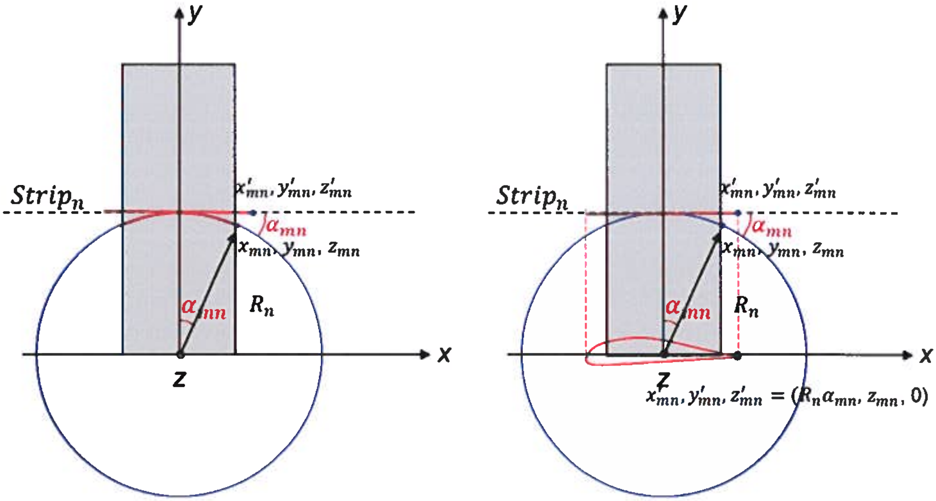

Figure 3.5: Unfolding procedure for an isoradius cut.

After performing the 2D simulations for each strip location, the boundary layer profiles are extracted at the same region as the 3D simulations and are imposed on the BATMAN code as boundary layer profiles to follow the same procedure. The flowcharts of these two processes have been demonstrated for 3 strips in Fig. 3.6. It should be noted that all processes shown in the flowchart for the 2D approach are done by the geometry file, so only a 2D mesh and 2D simulations are needed for the number of strips. The results from these 2D simulations are then fed into the BATMAN code to perform the far-field noise prediction at a given observer point.

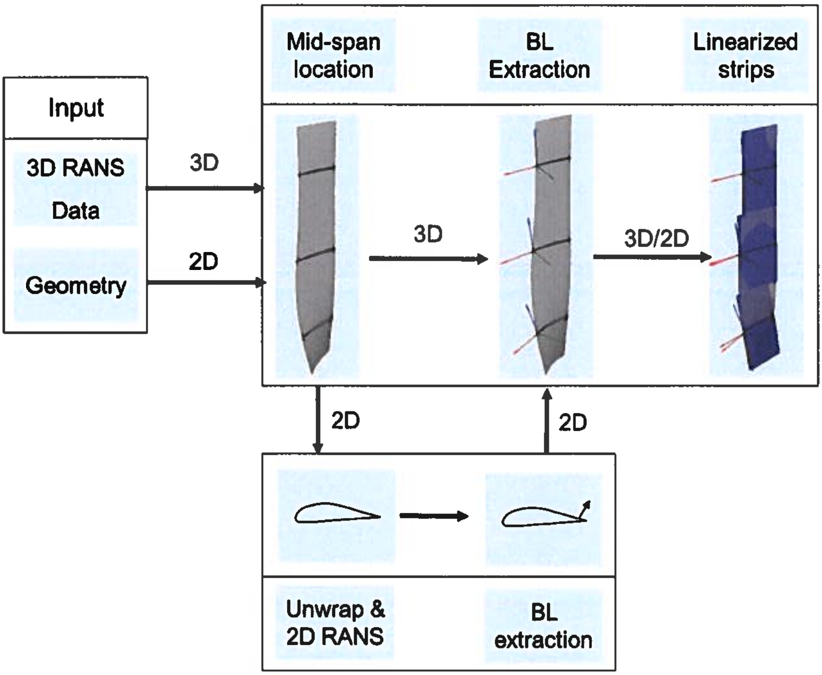

Figure 3.6: Implementation of the 2D approach.

4

ACCURACY AND MESH SENSITIVITY OF RANS-BASED TRAILING-EDGE NOISE PREDICTION USING AMIET'S THEORY FOR AN ISOLATED AIRFOIL

Airfoil self-noise is generated by the interaction of an airfoil with the turbulence that develops within its boundary layers and wake. According to Brooks et al. [31], it constitutes the dominant noise producing mechanism in applications such as low-speed cooling fans [45], wind turbines [20, 138] or high-lift devices [147].

Following the framework developed by Amiet [8], the mechanism of trailing edge noise generation can be represented as a scattering problem, where the convected wall-pressure disturbances associated with the turbulent boundary layer radiate acoustic waves to the far-field when they approach the trailing-edge discontinuity. In this model, the prediction of the acoustic field is based on a statistical description of the pressure field underneath the incoming turbulent boundary layer. To this end, two families of methods can be distinguished: *i)* based on a solution of the Poisson equation by integrating velocity statistics over the boundary layer thickness, or *ii)* directly addressing wall-pressure statistics through ad-hoc empirical models calibrated on experimental databases. In both cases, a Reynolds-Averaged Navier-Stokes (RANS) simulation of the flow field around the airfoil is in principle sufficient to provide the necessary input data, as long as the near-wall boundary layer is resolved well enough. An objective of this work is the comparison of the accuracy and numerical robustness that can be obtained by both approaches, depending on the near-wall resolution of the RANS model.

The commonly recommended wall-normal resolution for a correct modelling of boundary layer flows is $y^+ < 1$ for the first mesh node adjacent to the wall, where $y^+ = y\,u_\tau/\nu$ is the non-dimensional wall-normal coordinate with ν the kinematic viscosity and $u_\tau = \sqrt{\tau_w/\rho}$ the friction velocity based on the wall friction τ_w and fluid density

ρ. However, to authors' knowledge, the influence of the grid near-wall resolution on the determination of the wall-pressure spectrum models and far-field predictions have not been addressed in the literature, despite the practical importance of the issue in terms of cost vs. accuracy. Furthermore, the wall-pressure model is reconstructed near the trailing edge ($x/c > 0.98$) at where the applicability of some of the models is questionable. This chapter addresses this aspect. Two paths are followed to estimate the wall-pressure spectrum near the trailing edge, on the basis of RANS data. The first approach consists in re-scaling non-dimensional wall-pressure models which are the Goody, Rozenberg, Kamruzzaman and Lee models described in the previous chapter. The second approach uses the Panton and Linebarger [142] model based on an integration of the Poisson equation, also described in Chapter 3. It involves *a priori* less restrictive assumptions about the flow and should thus be more generally applicable. The wall-pressure spectra predicted by those methods with different grid resolutions are then used to predict the far-field noise prediction with Amiet's theory.

4.1. NUMERICAL SIMULATIONS

4.1.1. AIRFOIL CONFIGURATIONS

The two following airfoils, chosen from the BANC benchmark database [92], have been considered in this study: NACA0012 and DU96-W-180 with a sharp trailing edge. The NACA0012 is a zero cambered airfoil with 12% maximum thickness. The DU96-W-180 airfoil has a maximum thickness of 18% and has a 25% maximum camber at the 36.4% position of the chord. The dimensions and the operating conditions are given in Table 4.1. The NACA airfoil is tripped at 0.065% of the chord, both on the suction side and the pressure side, and is measured in the Laminar Wind Tunnel (LWT) of the University of Stuttgart [91]. For the DU96-W-180 airfoil, a trip strip is located at $x/c = 0.05$ for the suction side and $x/c = 0.1$ for the pressure side [91]. The NACA0012 experimental database includes the pressure distribution along the airfoil, velocity profiles, wall-pressure spectra and far-field noise measurements, while the DU96-W-180 database is restricted to far-field acoustic measurements [91]. The far-field spectra are computed at an observer distance of $r = 1\ m$ and for a wetted span of $b = 1\ m$. θ_r is the angle from the listener with the origin along the streamwise direction.

Table 4.1: Airfoil configuration

Airfoil	a.o.a	c	Re	U_∞	ρ_∞
	°	m	-	m/s	kg/m^3
NACA0012	0	0.4	1.5×10^6	56	1.181
DU96-W-180	4	0.3	1.13×10^6	60	1.164

4.1.2. COMPUTATIONAL SETUP

Steady two dimensional (2D) RANS simulations are performed with the open source CFD solver OpenFOAM 4.0 using the $k-\Omega$ SST turbulence model proposed by Menter [130]. The simulations are performed assuming turbulent flow along the full chord of the airfoils. A turbulence intensity of 0.1%, is applied at the inlet of the computational domain. The boundary conditions at the inlet are chosen as Dirichlet boundary conditions for all the variables except the pressure for which the gradient is set to zero. At the airfoil surface, low-Reynolds number wall functions are used for the kinetic energy k, the turbulent viscosity ν_t and the specific dissipation Ω. A no-slip condition is applied for the velocity and the pressure gradient is set to zero. At the outlet,the gradients of all variables are set to zero expect for the pressure that is imposed to be zero. Symmetric boundary conditions are applied at the top and bottom boundaries. The incompressible solver *simpleFoam* is used to perform the simulations. Second order accurate schemes are used with the under-relaxation of 0.7 for U, k_t, Ω and 0.3 for p.

4.2. MESH SENSITIVITY

The mesh is created with ANSYS ICEM. The mesh topology is based on the C-Grid type, which is here combined with an H-Grid, to optimize the skewness of the cells. The growth rate is chosen as 1.05 and the number of hexahedral cells can be found in Table 4.2 depending on the mesh refinement.

The domain size convergence is tested with two different configurations. The first configuration has a $10c$ length in the wall normal direction, $5c$ and $10c$ in the upstream and downstream directions, respectively. The second configuration is increased to $20c$ in the wall normal direction, $10c$ and $30c$ in the upstream and downstream directions, respectively. It is verified that the two domain sizes yield the same pressure coefficient along the airfoil and vertical velocity profile at $x/c = 0.99$. As a result, the domain with $10c$ lateral extent has been retained for the further calculations.

The generally recommended wall normal spacing for wall bounded flows is $y^+ < 1$, i.e. well within the laminar sublayer. In this study different values starting from the coarsest, $y^+ = 10$, to the finest, $y^+ < 1$, are investigated for both airfoils as listed in Table 4.2. It can be seen that for the DU96-W-180 airfoil, having $y^+ = 0.35$ on the suction side does not ensure yet the condition $y^+ < 1$ on the pressure side, so that the finest mesh has been further refined to obtain $y^+ < 1$ on both sides.

4.2.1. PRESSURE DISTRIBUTION AND BOUNDARY LAYER PROFILES

As mentioned in Section 3.4, the semi-empirical models require as input only the mean velocity profile, and the streamwise pressure gradient for those models that account for its effect, whereas the Panton & Linebarger model necessitates also turbulence profiles. Both pressure distributions along the airfoil and boundary layer statistics have thus been considered in the analysis below.

NACA0012 RESULTS

The pressure coefficient along the NACA0012 airfoil and the boundary layer profiles at $x/c = 0.99$ are investigated with respect to different wall normal spacings given in Table 4.2. The pressure distribution given in Fig. 4.1(a) appears insensitive with respect to

Table 4.2: Wall normal spacing for two airfoils

Airfoils	$\Delta y/c \times 10^3$	Number of cells	Min. y^+	Max. y^+	y^+ at $x/c = 0.99\%$	
					Suction side	Pressure side
NACA0012	0.6	81876	4	21	11.31	
	0.3	93368	2.92	13.5	5.34	
	0.05	125192	0.5	2.5	0.82	
	0.01	154364	0.1	0.5	0.17	
DU96-W-180	2	76363	7	37.5	10	23.2
	0.8	89636	3	22	4.2	13.8
	0.4	100867	1.11	15	1.53	8.14
	0.1	126392	0.13	5	0.35	2.1
	0.01	173358	0.019	0.5	0.04	0.2

the different grid refinements. A good match with the experiment [91] is obtained except for the transition region, $x/c \simeq 0.05$, which is expected as the present simulations assume fully turbulent flows. The velocity profile shown in Fig. 4.1(b) is also pretty much insensitive to the mesh refinement and matches fairly well the experimental data too [93]. The maximum turbulent kinetic energy (Fig. 4.1(c)) is seen to vary more significantly, furthermore its convergence cannot be definitely concluded considering its non-monotonous evolution with respect to the grid spacing. The difference between the finest mesh to the coarsest mesh is found to be 11%. The specific dissipation profile (Fig. 4.1(d)) exhibits insensitivity to the mesh resolution from the wall till $y/c \simeq 0.01$. Above this value, small changes are observed with respect to different grid sizes.

DU96-W-180 RESULTS

The results obtained for the DU96-W-180 airfoil with the mesh refinements given in Table 4.2 are shown in Fig. 4.2. As for the NACA0012 airfoil, the pressure distribution appears insensitive with respect to the grid size (Fig. 4.2(a)). The profiles of mean axial velocity, turbulent kinetic energy and specific dissipation extracted at $x/c = 0.99$ are given in Fig. 4.2(b),(c) and (d), respectively. It appears that the results obtained for the pressure side are less mesh-dependent than for the suction side, with the exception of the specific dissipation. The suction side boundary layer tends to thicken with the mesh refinement, while the pressure side boundary layer thickness remains overall unaffected. It is also observed that the coarsest mesh is unable to capture the velocity profile below $y/c < 0.002$. Consistently with the NACA0012 results, the turbulent kinetic energy profile exhibits a somewhat larger mesh sensitivity than the other quantities, with a maximum at the suction side that increases and shifts slightly upwards with finer meshes. The difference between the coarsest and the finest grids is around 16%. The kinetic energy profile on the pressure side is less affected. In contrast with the other quantities, the specific dissipation profile displays a slightly larger sensitivity on the pressure side than on the

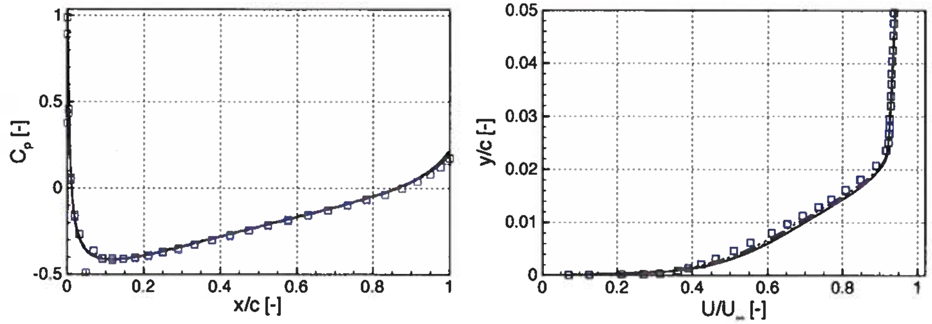

(a) Pressure coefficient.

(b) Mean axial velocity.

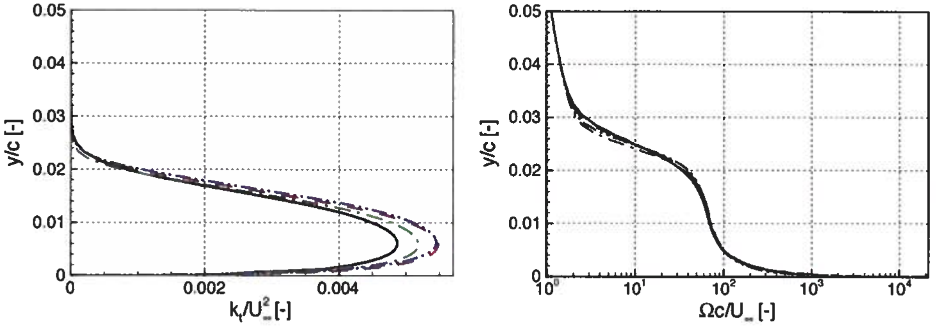

(c) Turbulent kinetic energy.

(d) Specific dissipation.

Figure 4.1: Pressure coefficient along the airfoil and non-dimensional boundary layer profiles at $x/c = 0.99$ from the leading edge with different grid sizes for the NACA0012 airfoil; suction side; (——), $y^+ \simeq 5$ (- - -), $y^+ \simeq 1$ (-·-·), $y^+ \simeq 0.2$ (-··-) and experiments (□) from Ref. [92].

suction side (Fig. 4.2(d)).

4.2.2. CALCULATION OF THE GLOBAL VARIABLES

In Section 3.4, it is noted that the commonly used approach to determine the boundary layer thickness, δ, is to find the location where the boundary layer edge velocity, U_e, is 0.99 % of the free-stream velocity $U_e = 0.99\,U_\infty$. However, this approach is not applicable in the presence of the adverse pressure gradient due to the fact that the free stream velocity, U_∞, does not converge to a certain value. In the following, three different approaches for defining the boundary layer thickness are presented:

1. Herr et al. [92] proposed to determine the boundary layer thickness at the inflection point.
2. the boundary layer thickness is defined as the distance where the turbulent kinetic energy is equal to $\mathrm{TKE}(\delta) = 0.0002U_0^2$ [39].
3. the boundary layer thickness is defined as the position at which the total pressure

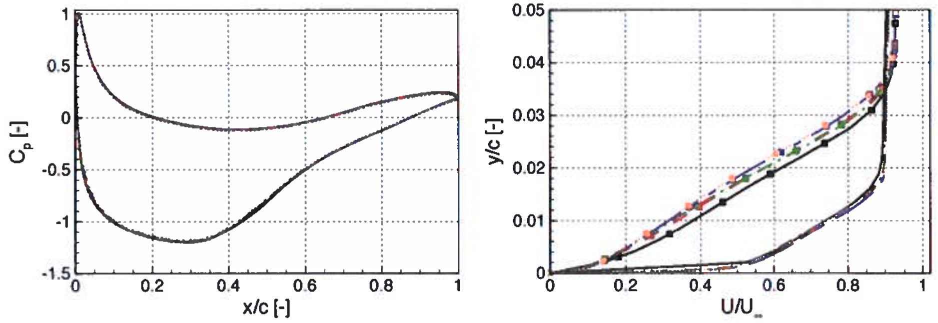

(a) Pressure coefficient.

(b) Mean axial velocity.

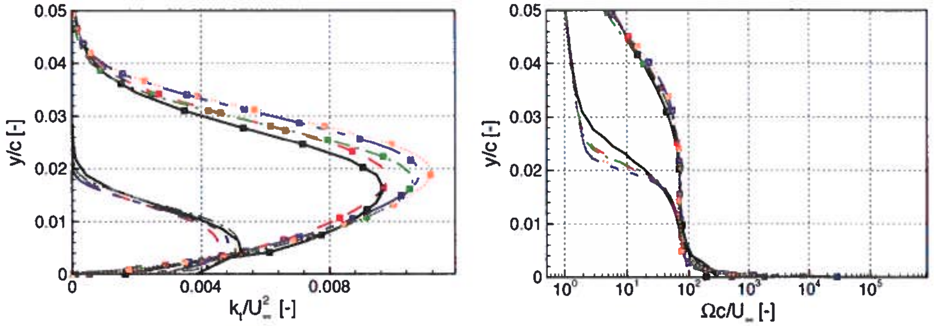

(c) Turbulent kinetic energy.

(d) Specific dissipation.

Figure 4.2: Pressure coefficient along the airfoil and non-dimensional boundary layer profiles at $x/c = 0.99$ from the leading edge with different grid sizes for the DU96-W-180 airfoil; $y^+ \simeq 23$ (——), $y^+ \simeq 14$ (- - -), $y^+ \simeq 8$ (-·-), $y^+ \simeq 2$ (-··-), $y^+ \simeq 0.2$ (·····) and (line-symbols: suction side, line: pressure side).

is 99% of the maximum total pressure.

The boundary layer profile normal to the surface is extracted at $x/c = 0.99$ from the leading edge. Figure 4.3 represents the position of the boundary layer thickness and the corresponding edge-velocity for NACA0012 at 0° angle of attack with three different approaches mentioned previously. The inflection point method in Fig. 4.3(a), where the second derivative of the streamwise velocity with respect to the wall-normal distance changes the sign, proposed by Herr et al. [92] is challenging since the second derivative is noisy and over-estimated the value which is not shown in the Fig. 4.3. Thus, the inflection point is determined from the minimum value of the first derivative. The second approach is to assign the boundary layer thickness from the kinetic energy where $\mathrm{TKE}(\delta) = 0.0002U_0^2$ [39] (Fig. 4.3(b)). This method is more straightforward since the right-hand side of the equation is a known value. The last method considered in this paper is to locate δ at which the total pressure is 99% of the maximum total pressure. Even though the approach seems similar to the commonly used method, $U_e/U_\infty = 0.99$, it guarantees that the total pressure becomes constant above the boundary layer thick-

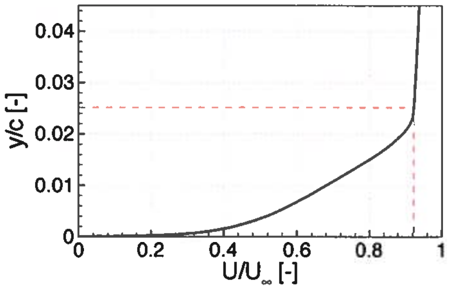

(a) First method.

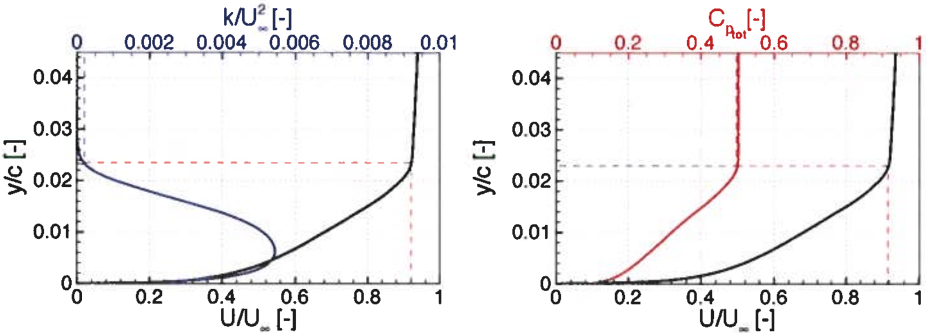

(b) Second method.

(c) Third method.

Figure 4.3: Determination of the boundary layer thickness and the corresponding boundary layer edge velocity with three different methods for the NACA0012 airfoil at 0° angle of attack obtained at $x/c = 0.99$ from the leading edge.

ness (Fig. 4.3(c)). The values obtained using each methods are given in Table 4.3. The next step is to investigate the sensitivity of the semi-empirical methods to the boundary layer thickness and the boundary layer edge velocity obtained from three different approaches. The momentum thickness, θ, and displacement thickness, δ^*, are computed for each method. The friction velocity, u_τ, and Coles' wake parameter, Π, are found by fitting the velocity boundary layer to the law of the wake.

The effect of the different boundary layer thicknesses and edge velocities on the wall-pressure spectra predicted by the Goody, Rozenberg and Catlett models are shown in Fig. 4.4, and are compared with experimental data. The other models are found to be insensitive to these parameters and not presented in the paper. It is observed that the Goody and Catlett models exhibit a similar behavior. The models are insensitive to the boundary layer parameters at moderate and high frequency whereas 1 dB deviations occurs at low-frequencies. On the contrary, the Rozenberg model is sensitive to the boundary layer parameters for the low frequencies. From the point of maximum of ϕ, up to the highest frequency a deviation of up to 2 dB occurs. The other models mentioned in Sec-

Table 4.3: Boundary layer thickness and boundary layer edge velocity obtained by three different methods for the NACA0012 airfoil at 0° angle of attack obtained at $x/c = 0.99$.

Method	δ/c	U_e/U_∞	δ^*/c	θ/c
1	0.0252	0.9231	0.0058	0.0035
2	0.0235	0.9202	0.0057	0.0034
3	0.0229	0.9186	0.0057	0.0034

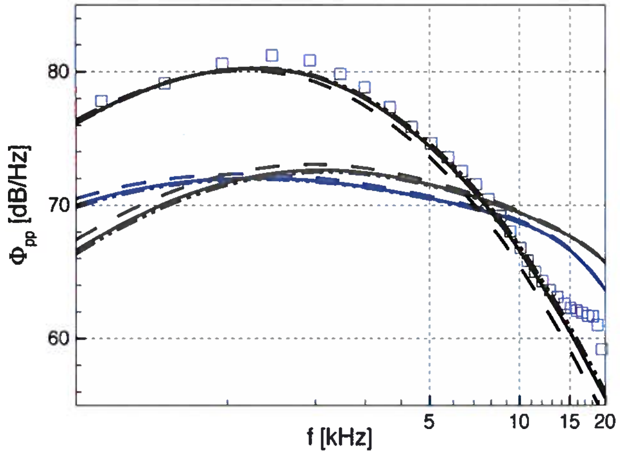

Figure 4.4: Wall-pressure spectra prediction by different models at $x/c = 0.99$ from the leading edge for the NACA0012 airfoil at 0° angle of attack; Rozenberg (——), Goody (——), Catlett (——) models and experimental data from LWT (□) [92]; 1^{st} method (- - -); 2^{nd} method (-·-·) and 3^{rd} method (——).

tion 3.4 are disregarded since they do not exhibit any sensitivity to the boundary layer parameters. When the scaling parameters for the spectrum and the frequency are considered, Goody and Catlett models are the only ones who used the same scaling. This could be a possible explanation of their similar behavior even though their parametrization is completely different. For the Rozenberg model, the driving parameter for the trend is mainly Δ_* which appears only in this model. Overall, it is observed that the first method over-predicts the boundary layer parameters and under-estimates the high frequency part for the Rozenberg model. The drawback of the Catlett et al. [39] method is that when the simulations are performed by a two-equation turbulence model, it is not always possible to acquire the turbulent kinetic energy, k_t accurately. Thus, in terms of ease and direct comparison to experimental data, it is suggested that the boundary layer thickness obtained by the total pressure method is more suitable. Consequently, this method has been applied to all the results presented herein after. Furthermore, the experimental data is dominated by the background noise after 15 kHz, thus the frequencies higher than this will be neglected for the following parts.

The other discrepancy found in Section 3.4 regarding the semi-empirical models is the determination of Π and β_c. These parameters are only in the Rozenberg and Kamruzzaman models. In both models, Π is calculated from Eq. 3.8 whereas β_c is calculated from Eq. 3.9 for the Kamruzzaman model. However, in the present study, Π is obtained from solving Eq. 3.7 implicitly as well as finding the best fit with the law of the wake whereas the β_c value is calculated directly from the definition of the Clauser's equilibrium parameter, which is the same method as the Rozenberg model. The corresponding values for two models are given in Table 4.4 and compared with the experimental data in Fig. 4.5.

Table 4.4: Values of Π and β_c obtained from different equations.

Models	β_c	Π	β_c	Π
	$(\theta/\tau_w)(dp/dx)$	Eq. 3.7	Eq. 3.9	Eq. 3.8
Rozenberg	5.2832	2.2931	-	2.9834
Kamruzzaman			5.1670	

In the general form of the wall-pressure spectrum given in Eq. 3.5, the parameter a, which alters the amplitude of the spectrum, is driven by Π for the Rozenberg model while Π and β_c for the Kamruzzaman model. The corresponding values are given in Table 3.1. Figure 4.5(a) shows an increment of 1 dB over the whole range of the spectrum when the Π value is increased by 30%. For the Kamruzzaman model, even though β_c value is reduced by 2%, which should result in a decrease on the amplitude of the spectra, an increment of less than 1 dB is observed since the increment of Π is more dominant. Furthermore, the comparison with the experimental data reveals that the amplitude for the low and mid frequencies are captured better with the newly calculated variables. However, the higher frequency part is over-estimated for both models. In conclusion, this analysis demonstrates that there is not a certain method that gives the most accurate prediction. Depending on the definition of the variable the spectrum of the amplitude changes around ±1 dB. The wall-pressure spectra presented herein after are calculated by the methods considered in the current study which provide better predictions for the higher frequencies. The comparison of the models with respect to the experimental data is investigated in the Sec. 4.2.3.

4.2.3. PREDICTION OF THE WALL-PRESSURE SPECTRA AND FAR-FIELD TRAILING EDGE NOISE

Based on the above results, the impact of the mesh resolution on the noise obtained by means of the semi-empirical models is evaluated for the DU96-W-180 airfoil only, since the NACA0012 pressure distribution and mean velocity profiles are fairly mesh-insensitive. In contrast, the boundary layer turbulent kinetic energy profiles, used as input for the Panton & Linebarger model, showed more significant discrepancies for both the NACA0012 and DU96-W-180 airfoils.

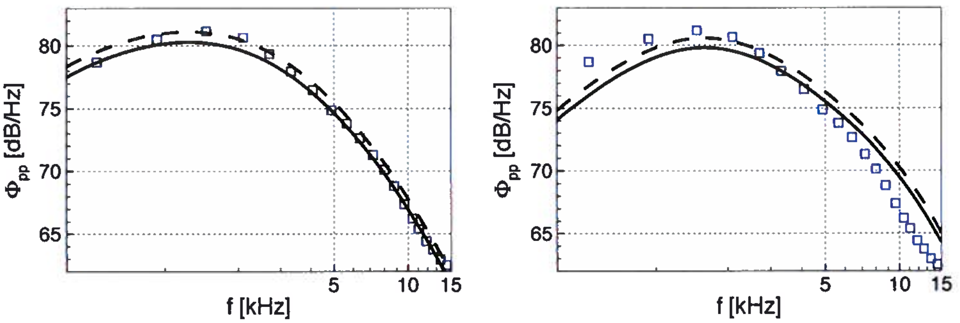

(a) Rozenberg model.

(b) Kamruzzaman model.

Figure 4.5: The comparison of the wall-pressure spectra which is calculated by different definition of β_C and Π; (——) is calculated by Π obtained from the Eq. 3.7 and β_C from $(\theta/\tau_w)(dp/dx)$; (- - -) is calculated by Π obtained from the Eq. 3.8 for both models and β_C is calculated from Eq. 3.9 for only Kamruzzaman model; experimental data from LWT(□) [92].

NACA0012 RESULTS OBTAINED USING PANTON & LINEBARGER INTEGRAL APPROACH

The wall-pressure spectra predicted by the Panton and Linebarger [142] model is shown in Fig. 4.6(a) where the dimensionless frequency is obtained by the values in Table 4.5. Only the suction side results are displayed for this symmetric airfoil at 0° angle of attack. It has been verified that the variations that can be observed for dimensionless frequencies below 0.7 are due to an insufficient convergence of the Monte-Carlo integration leading to uncertainties of around 3 dB, and the results below that frequency will not be further discussed.

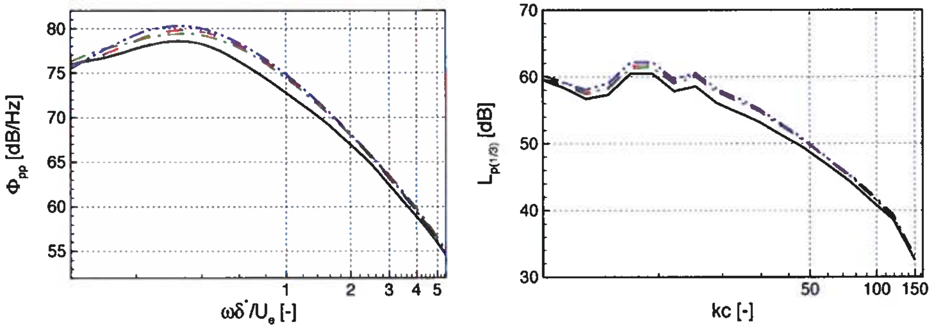

(a) Wall-pressure spectrum at $x/c = 0.99$.

(b) Far-field third-octave noise spectrum.

Figure 4.6: Wall-pressure spectra prediction by the Panton and Linebarger [142] model and the corresponding far-field noise prediction with different grid sizes: $y^+ \simeq 11$ (——), $y^+ \simeq 5$ (- - -), $y^+ \simeq 1$ (-·-), $y^+ \simeq 0.2$ (-··-).

It is observed that the fluctuation amplitude obtained with $y^+ \simeq 11$ deviates from the others by about 3 dB for middle frequencies. The difference decreases for higher frequencies. Logically, the same observation can be made for the 1/3-octave band far-field trailing edge noise prediction. This must be attributed to the differences observed in the turbulent kinetic energy profiles in Fig. 4.2(c). It can be concluded that $y^+ < 5$ yields a convergence towards the finest mesh sound spectra within 1 dB.

NACA0012 RESULTS OBTAINED USING THE SEMI-EMPIRICAL AND INTEGRAL APPROACHES

In terms of absolute validation, the wall-pressure spectra predicted by the seven models depicted in this paper for the NACA0012 airfoil, and the corresponding 1/3-octave band far-field noise spectra, are compared in Fig. 4.7 with experimental data obtained in DLR's Acoustic Wind-Tunnel Braunschweig (AWB), IAG Laminar Wind Tunnel (LWT) and UF Aeroacoustic Flow Facility (UFAFF) [92]. Considering the wall-pressure spectra firstly, it can be first observed that the ZPG model of Goody performs poorly as shown in Fig. 4.7(a), which is sensible considering the non-negligible APG near the trailing edge of this airfoil. Models including an APG correction proved to yield much better agreement with experimental data except for the Catlett and Herr & Hu models. They share a common point; both of them performed their experiments on a flat-plate where a APG flow is created with trailing-edge sections [39] or a rotational airfoil [98] and obtained satisfactory results. Even though, they compared their model with Rozenberg's model, they have not performed any predictions for airfoil flows. There, it can be deduced that these models are unrepresentative for airfoils. The Rozenberg model demonstrates a good match for the high frequencies whereas the maximum amplitude is underestimated.

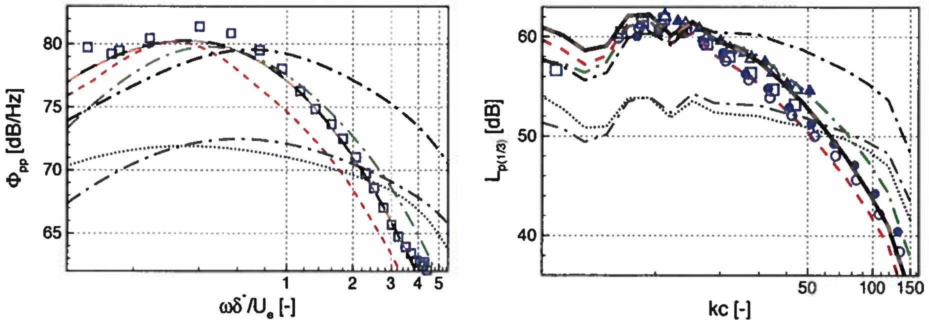

(a) Wall-pressure spectrum at $x/c = 0.99$.

(b) Far-field third-octave noise spectrum.

Figure 4.7: Far-field noise prediction by different wall-pressure spectrum models for the NACA0012; Goody (·····), Rozenberg (——), Catlett (-·-·), Kamruzzaman (-·-), Herr & Hu (-··-), Lee (-··-), Panton & Linebarger (- - -) models and experimental data from LWT (□), AWB (○), UFAFF (△).

Kamrazzuman model, which is developed by considering airfoil flows, performs better compared to the previous models. The model under-predicted below $\omega\delta^*/U_e < 0.7$ and over-predicts above that range. When the formalization is considered, all the parameters are constant except the parameter a which is a function of Π and β and only regulates the spectrum amplitude. Thus, increasing the amplitude by changing those parameters will perform a better match for the peak region whereas worsen the higher frequencies. Furthermore, it is observed that by reducing the parameter d, the peak point of the spectra shifts to the lower frequencies as well as the amplitude of the frequencies below the peak point increases which is lacking in this model. Thus, it can be concluded that this model provides a good prediction around ±3 dB above the middle frequency range regarding to its simplicity. The Lee model provides results identical to those of the Rozenberg model in this case. The reason as stated in Sec. 3.4 is that only the a, d and h parameters are modified to take into account the aforementioned issues. These parameters are a function of β_C or R_T. In this airfoil case, a and d parameters give the same value as in the Rozenberg model and the value of the h parameter is only slightly different (see Table 4.5 for the values.). The statistical model proposed by Panton & Linebarger, captures the trend for all the cases, however, under-predicts around 3 dB. The possible reason for the under-estimation is due to the anisotropy factor applied for the wall-normal velocity fluctuations which are obtained from a flat-plate. However, for APG flows, it is expected to be higher.

Table 4.5: Boundary layer parameters.

NACA0012	0°
U_e/U_∞	0.9186
δ/c	0.0229
δ^*/c	0.0057
θ/c	0.0034
u_τ/U_∞	0.0277
Δ_*	4.02
R_T	28.80
Π	2.2931
β_C	5.2832
H	1.676
Δ	0.2056

About the far-field noise predictions, the results shown in Fig. 4.7(b) confirm that the Goody, Catlett and Herr & Hu models model yield a poor agreement with experimental data. A good match is obtained using the Rozenberg and Lee models and the UAFF and AWB dataset for the highest frequencies $kc > 60$. The Kamruzzaman model performs well for the middle range but over-predicts the highest frequencies by about 2 dB. Comparison with the AWB data shows that the model of Panton & Linebarger gives good results below $kc < 20$ but under-predicts slightly the higher frequencies. A possible improvement could be the reconstruction of the streamwise velocity fluctuations with an anisotropy factor accounting for pressure gradient effects.

DU96-W-180 RESULTS

The variables required by the semi-empirical models have been determined processing the boundary layer profile data shown in Fig. 4.2, to yield the values given in Table 4.6. Noteworthy, the Clauser parameter for the pressure side is negative, indicating a FPG, while its value for the suction side is largely positive corresponding to a significant APG. This will lead to distinct observations concerning the respective contributions of the pressure side and suction side boundary layers to the far-field noise spectrum. In this section all the APG models except the Catlett and Hu & Herr models, which result in poor prediction with the mild APG flows, will be investigated with their base model, Goody.

Table 4.6: Global variables with different y^+ values.

side	y^+	δ/c	U_e/U_∞	u_τ/U_∞	δ^*/c	θ/c	Π	β
Suction side	10	0.0379	0.918	0.0149	0.0132	0.0059	8.42	15.05
	4	0.0407	0.922	0.0133	0.0153	0.0063	10.13	17.34
	1.5	0.0399	0.922	0.0122	0.0156	0.0061	11.30	20.84
	0.3	0.0414	0.922	0.0122	0.0165	0.0065	11.22	22.32
	0.04	0.0409	0.921	0.0118	0.0167	0.0065	11.54	21.11
Pressure side	23	0.0216	0.8908	0.0326	0.0034	0.0024	1.329	-1.95
	14	0.0187	0.892	0.0341	0.0034	0.0024	1.004	-2.06
	8	0.0194	0.894	0.0329	0.0038	0.0026	1.21	-2.32
	2	0.0182	0.895	0.0340	0.0036	0.0024	1.01	-2.36
	0.2	0.0189	0.897	0.0335	0.0039	0.0026	1.07	-2.55

The dimensionless frequency for wall-pressure spectrum is obtained by the global variables' values for the finest mesh size on the suction side given in Table 4.6. The wall-pressure spectra predicted by the Goody model are given in Fig. 4.8(a). Quite different mesh convergence behaviors are obtained for the suction and pressure sides. While on the pressure side the wall-pressure spectra appear to be fairly independent of the mesh resolution, for the suction side each mesh refinement leads to a significant reduction of the amplitude to eventually reach convergence for y^+ comprised between 0.3 and 0.04. But since the suction side contribution to the far-field is largely dominated by the pressure side contribution in this model, the far-field noise prediction turns out to be insensitive to mesh resolution. The result is a spectrum (Fig. 4.8(b)) that is only coincidentally matching the measurements at high frequencies, the overall trend being clearly missed. As remarked above for the NACA0012 airfoil, the fact that the Goody model neglects pressure gradients effects is the likely cause of a misrepresentation of both pressure and suction side wall-pressure spectra.

The Rozenberg model applied to the suction side data yields the wall-pressure spectra shown in Fig. 4.9(a). The mesh sensitivity is found weaker for the low frequencies than for the high frequencies, where the coarsest mesh resolution in particular deviates by up to 6 dB compared with the finer mesh results. The data for the pressure side

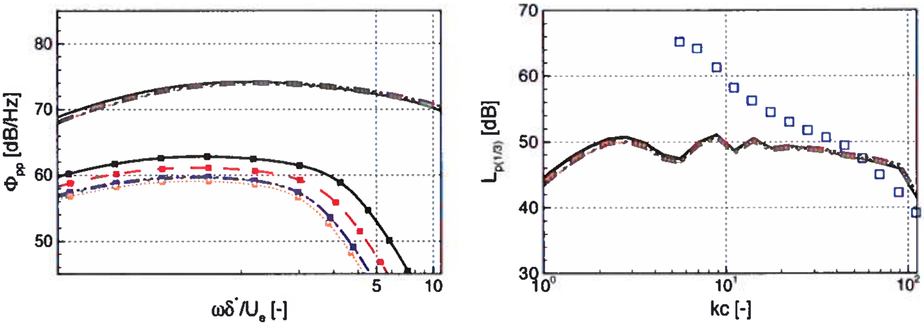

(a) Wall-pressure spectrum at $x/c = 0.99$.

(b) Far-field third-octave noise spectrum.

Figure 4.8: Wall-pressure spectra prediction by the Goody [79] model and corresponding the far-field noise prediction with different grid sizes for the DU96-W-180. Pressure side (plain): $y^+ \simeq 23$ (——), $y^+ \simeq 14$ (- - -), $y^+ \simeq 8$ (-·-·), $y^+ \simeq 2$ (-··-), $y^+ \simeq 0.2$ (·····); suction side (■): $y^+ \simeq 10$ (——), $y^+ \simeq 4$ (- - -), $y^+ \simeq 1.5$ (-·-·), $y^+ \simeq 0.3$ (-··-), $y^+ \simeq 0.04$ (·····); experiments [92]: □.

have not been used in the Rozenberg model following the recommendations of Rozenberg et al. [159] themselves, who advised against using their model for FPG. However, the Goody model has been presumed to be applicable to the pressure side, owing to the moderate FPG that is reported in Table 4.6. Consequently, the far-field noise prediction shown in Fig. 4.9(b) has been obtained using the Rozenberg model for the suction side and the Goody model for the pressure side. The result is a spectrum exhibiting higher levels at low frequencies than using the Goody model for both sides, thereby reducing somewhat the gap with the experimental data. The spectrum a high frequencies being dominated by the pressure side contribution, it is similar to that shown in Fig. 4.8(b). The combined model remains overall unable to capture both the trend and the amplitude of the measured sound field. In terms of mesh dependency, it is observed that the results are insensitive to the mesh size even though the coarsest mesh on the pressure side is around $y^+ \simeq 23$.

The wall-pressure spectra obtained using the Kamruzzaman model in Fig. 4.10(a) exhibit variations of about 4 dB between the coarsest and the finest grid sizes for the suction side, converging within 2 dB for y^+ less than 4. A smaller sensitivity is found for the pressure side, especially at high frequencies. Interestingly, for the suction side a mesh refinement induces an increase of the low-frequency levels and a reduction of the high-frequency content with little impact around $\omega\delta^*/U_e \approx 1.2$, while the effect is more uniformly distributed for the pressure side. The combination of the pressure and suction side sensitivities yields a far-field noise prediction in Fig. 4.10(b) that is fairly mesh-independent for frequencies above $kc > 10$, where the model provides also fair agreement with experimental data. The levels are under-predicted by about 3 dB at lower frequencies.

The Lee model performs similarly to the Rozenberg model in terms of mesh sensitivity (Fig. 4.11(a)), but gives significantly higher levels (up to 8 dB) as a result of modifying the A parameter. This model is also inapplicable to FPG flows so that the Goody model is

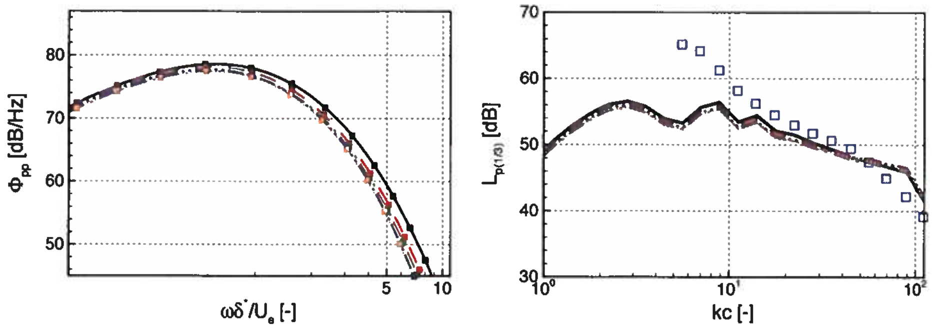

(a) Wall-pressure spectrum at $x/c = 0.99$.

(b) Far-field third-octave noise spectrum.

Figure 4.9: Wall-pressure spectra prediction by the Rozenberg [159] model on the DU96-W-180 airfoil suction side and far-field noise prediction combining this result with Goody's model for the pressure side. Suction side (■): $y^+ \simeq 10$ (——), $y^+ \simeq 4$ (- - -), $y^+ \simeq 1.5$ (-·-), $y^+ \simeq 0.3$ (-··-), $y^+ \simeq 0.04$ (·····); pressure side: see legend of Fig. 4.8; experiments [92]: □.

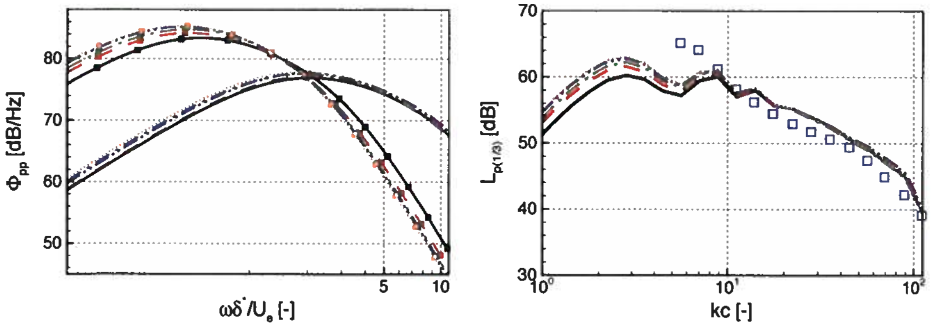

(a) Wall-pressure spectrum at $x/c = 0.99$.

(b) Far-field third-octave noise spectrum.

Figure 4.10: Wall-pressure spectra prediction by the Kamruzzaman [110] model and corresponding far-field noise prediction with different grid sizes for the DU96-W-180. Pressure side (plain): $y^+ \simeq 23$ (——), $y^+ \simeq 14$ (- - -), $y^+ \simeq 8$ (-·-), $y^+ \simeq 2$ (-··-), $y^+ \simeq 0.2$ (·····); suction side (■): $y^+ \simeq 10$ (——), $y^+ \simeq 4$ (- - -), $y^+ \simeq 1.5$ (-·-), $y^+ \simeq 0.3$ (-··-), $y^+ \simeq 0.04$ (·····); experiments [92]: □.

again used for the pressure side contribution. The far-field noise prediction reveals that small mesh-induced variations occur for frequencies below $kc < 10$, where the measured acoustic levels are again under-predicted. The change of slope at higher frequencies is due to the switch of predominance from the suction side to pressure side.

Finally, the wall-pressure spectrum prediction by the Panton & Linebarger integral model is given in Fig. 4.12(a). The suction side contribution dominates the radiated spectrum for dimensionless frequencies below 2, consistently with the results obtained using the Kamruzzaman model. The finest mesh size yields higher amplitudes for dimensionless frequencies below 2 and reduced levels above it. The overall amplitude dif-

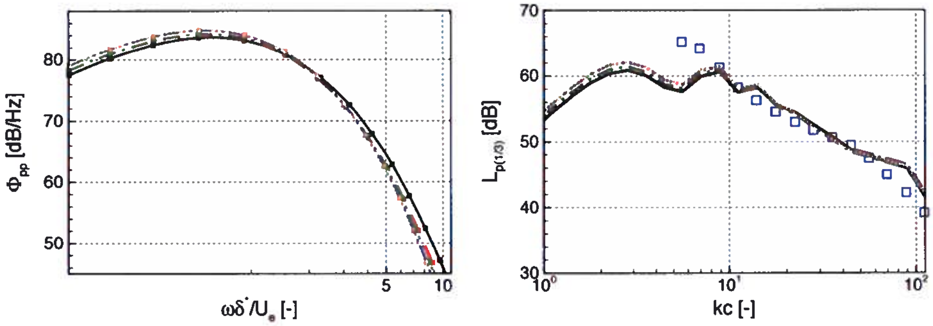

(a) Wall-pressure spectra prediction.

(b) Far-field noise prediction.

Figure 4.11: Wall-pressure spectra prediction by the Lee [119] model on the DU96-W-180 airfoil suction side and far-field noise prediction combining this result with Goody's model for the pressure side. Suction side (■): $y^+ \simeq 10$ (——), $y^+ \simeq 4$ (- - -), $y^+ \simeq 1.5$ (-·-), $y^+ \simeq 0.3$ (-··-), $y^+ \simeq 0.04$ (·····); pressure side: see legend of Fig. 4.8; experiments [92]: □.

ference remains around 2 dB between the finest and the coarsest mesh. For the pressure side, the difference between the coarsest and the other meshes increases more significantly above $\omega\delta^*/U_e > 2$. This could be related to the discrepancies mentioned above for the velocity and specific dissipation profiles (Fig. 4.2(a) and 4.2(b)). The far-field noise prediction shown in Fig. 4.12(b) shows that the stronger pressure side variability has a significant effect on the predicted sound spectrum, unexpectedly providing a better agreement with experiments for the coarsest mesh. Apart from this - likely coincidental - effect, the mesh-related variability of the predicted spectra remains within 2 dB. The overall comparison with the measured sound spectrum is overall good, with substantial improvements at the lowest frequencies compared with the semi-empirical models.

4.3. EFFECT OF THE PROBE LOCATION ALONG THE AIRFOIL

In the previous section, the far-field noise are performed by the wall-pressure spectra which are obtained from the boundary layer profiles extracted at the $x/c = 0.99$. However, it is observed that the Rozenberg and Lee models are inapplicable at the location where the boundary layer is exposed to a FPG flow. The focus of this section is to investigate the effect of the pressure gradient on the wall-pressure spectrum and the far-field noise prediction along the airfoil chord by extracting the boundary layer profiles from different probe locations, $x/c = 0.9$ till 0.99, for the DU96-W-180 airfoil. Later, the wall-pressure spectra models will be computed for each probe location to investigate the sensitivity on the local quantities. The velocity profile in Fig. 4.13 shows that the APG has a significant effect on the suction side. Hence, the value of integral boundary layer parameters (δ, δ^* and θ) and the wake parameters (Π, β) increase and the other parameters: U_e and u_τ decrease as shown in Tab. 4.7. For the pressure side, the APG is present until $y/c \simeq 0.05$ which can be deduced from the pressure coefficient in Fig. 4.2(a). After that location, there is a favorable pressure gradient, $\beta < 0$ (see Tab. 4.7). The turbulent kinetic

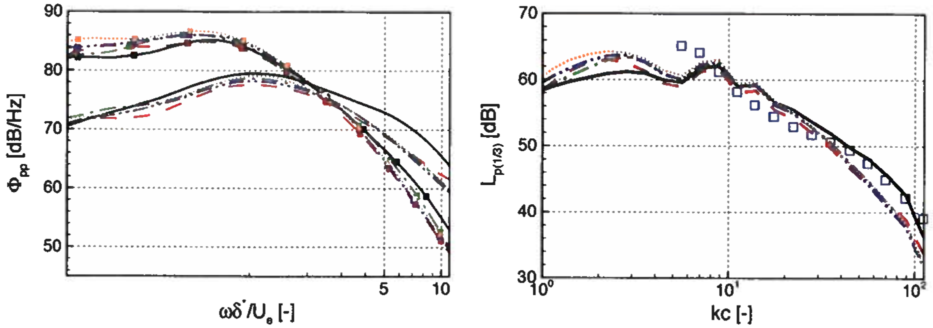

(a) Wall-pressure spectra prediction.

(b) Far-field noise prediction.

Figure 4.12: Wall-pressure spectra prediction by the Panton & Linebarger Panton and Linebarger [142] model and corresponding far-field noise prediction with different grid sizes for the DU96-W-180. Pressure side (plain): $y^+ \simeq 23$ (——), $y^+ \simeq 14$ (- - -), $y^+ \simeq 8$ (-·-·), $y^+ \simeq 2$ (-··-), $y^+ \simeq 0.2$ (·····); suction side (■): $y^+ \simeq 10$ (——), $y^+ \simeq 4$ (- - -), $y^+ \simeq 1.5$ (-·-·), $y^+ \simeq 0.3$ (-··-), $y^+ \simeq 0.04$ (·····); experiments [92]: □.

energy profile given in Fig. 4.13(b) shows that the maximum value increases and shifts up when the probe location is closer to the trailing-edge on the suction side. Contrary, the peak point decreases and above $y/c \simeq 0.0053$ shifts upwards for the pressure side. Fig. 4.13(c) demonstrates that the specific dissipation profile decreases from surface till $y/c \simeq 0.02$, and switches the behavior for the suction side. The same trend is observed for the pressure side except, this time, the switching point changed to $y/c \simeq 0.01$. Overall, it can be interpreted that the effect of probe location on the suction side appears stronger than on the pressure side. The graphical of the values given in Tab. 4.7 are reported in Appendix A.

In this section, the Goody model is not considered since it provides poor predictions with respect to the other models. The effect of the probe location on the wall-pressure spectra predicted by Rozenberg's model is shown in Fig. 4.14(a). The frequencies for the wall-pressure spectrum are non-dimensionalized by the global variables' values for the $x/c = 0.01$ on the section side. It has been observed that the lower frequencies $\omega\delta^*/U_e < 0.5$ are less sensitive to the probe location than the higher frequencies on the suction side and the amplitude decreases when the probe location gets closer to the trailing-edge which is due to the smaller values of Π and Δ_*. However, the deviation is less than 3 dB above the frequencies $\omega\delta^*/U_e > 5$ for the pressure side until the probe location $x/c = 0.97$ where the flow is exposed to FPG. After that point, the behavior of the response completely changes. The far-field noise prediction given in Fig. 4.14(b) shows that the low frequencies are under-estimated and the slope is not captured. In contrast with the NACA0012 airfoil results, the decay at the highest frequencies isn't observed. The wall-pressure spectrum on suction side predicted by Kamruzzaman model indicates that the amplitude of the spectrum increases along the airfoil chord starting from 8 dB till $\omega\delta^*/U_e = 1.4$ due to the parameter a (Fig. 4.15(a)). Above these frequencies, the decay of the overlap region becomes steeper which is regulated by the parameter, R_T' and reaches around 12 dB. The pressure side seems rather insensitive to the

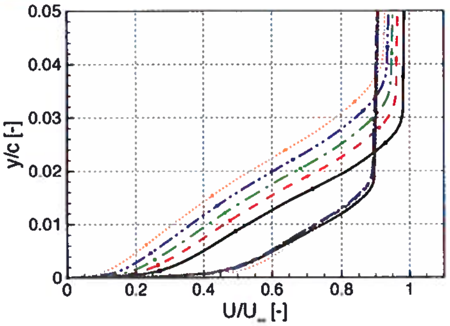

(a) Velocity profile.

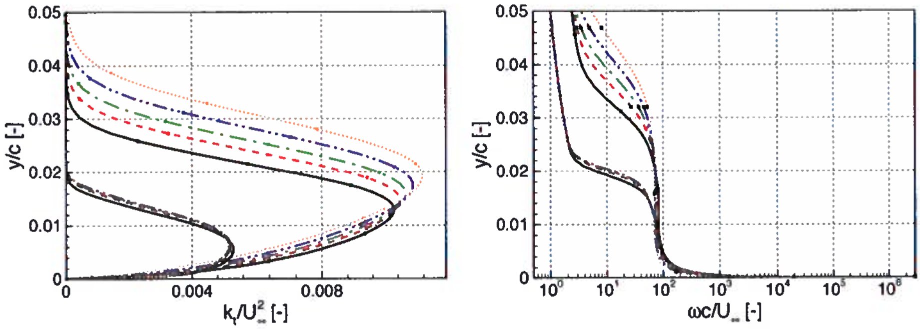

(b) Turbulent kinetic energy profile.

(c) Specific dissipation profile.

Figure 4.13: Non-dimensional boundary layer profiles for the DU96-W-180 along the airfoil chord; $x/c = 0.9$ (——), $x/c = 0.93$ (- - -), $x/c = 0.95$ (-·-·), $x/c = 0.97$ (-··-) and $x/c = 0.99$ (·····); (line-symbols: suction side, line: pressure side).

probe location except at $x/c = 0.99$ for which the maximum difference is around 2 dB. The far-field noise prediction exhibits a 4 dB increase in the amplitude starting from the low frequencies till $kc = 10$. The slope after this range is well captured. The same behavior is observed with the Lee model for the suction side as the Kamruzzaman model (Fig. 4.16(a)). The amplitude of the spectrum for the low frequencies is increased around 10 dB with the modification of the parameter a. For the pressure side, the model starts to deviate after $x/c = 0.97$ and becomes inapplicable. The far-field noise prediction reveals that the model is unable to capture the amplitude for the low frequencies. The decay has been observed for the frequencies between $10 < kc < 87$ whereas over-predicted around 4 dB. The highest frequency decay, $kc > 87$, is not captured by the model in the presence of FPG flow. The wall-pressure spectrum prediction by Panton & Linebarger's model shown in Fig. 4.17(a) shows that when the probe position on the suction side approaches the trailing-edge, the amplitude increases for the dimensionless frequencies below $\omega\delta^*/U_e < 0.8$ and decreases up to 8 dB for the frequencies above $\omega\delta^*/U_e > 0.8$. Closer to the trailing-edge, a deviation is observed starting from $\omega\delta^*/U_e > 4$ up to 3 dB for the higher frequencies on the pressure side. The far-field noise prediction given in

Table 4.7: Global variables with respect to probe location.

x/c	side	δ/c	U_e/U_∞	u_τ/U_∞	δ^*/c	θ/c	Π	β
0.1	SS	0.0296	0.976	0.0210	0.0098	0.0049	5.10	8.16
	PS	0.0179	0.894	0.0313	0.0040	0.0025	1.57	0.48
0.07	SS	0.0329	0.956	0.0183	0.0115	0.0054	6.34	11.22
	PS	0.0184	0.888	0.0311	0.0042	0.0026	1.53	0.48
0.05	SS	0.0357	0.944	0.0163	0.0130	0.0058	7.55	14.07
	PS	0.0188	0.888	0.0312	0.0042	0.0027	1.48	0.27
0.03	SS	0.0376	0.93	0.0141	0.0146	0.0062	9.12	18.48
	PS	0.0189	0.890	0.0318	0.0042	0.0027	1.35	-0.55
0.01	SS	0.0409	0.921	0.0118	0.0167	0.0065	11.54	21.11
	PS	0.0189	0.897	0.0335	0.0039	0.0026	1.07	-2.55

Fig. 4.17(b) exhibits that a deviation of 4 dB above $kc > 10$ can be obtained with different probe positions.

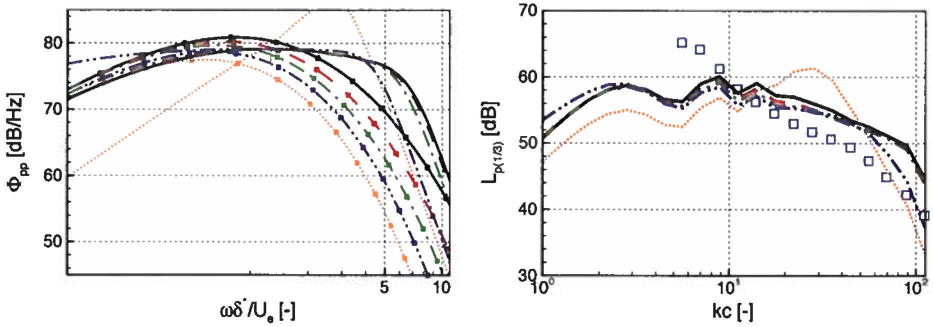

(a) Wall-pressure spectra prediction.

(b) Far-field noise prediction.

Figure 4.14: Wall-pressure spectrum predicted by the Rozenberg [159] model and corresponding the far-field noise prediction on the DU96-W-180 airfoil varying extraction position along the chord; x/c = 0.9 (——), x/c = 0.93 (- - -), x/c = 0.95 (-·-·), x/c = 0.97 (-···-) and x/c = 0.99 (·····); (line-symbols: suction side, line: pressure side).

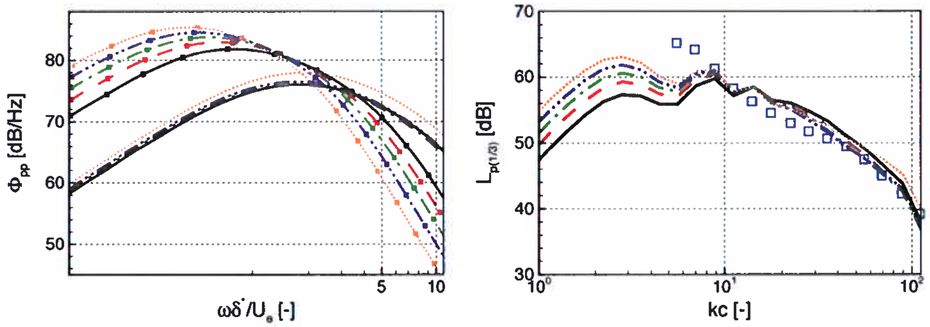

(a) Wall-pressure spectra prediction.

(b) Far-field noise prediction.

Figure 4.15: The wall-pressure spectrum predicted by the Kamruzzaman [110] model and corresponding the far-field noise prediction on the DU96-W-180 airfoil varying extraction position along the chord; $x/c = 0.9$ (——), $x/c = 0.93$ (- - -), $x/c = 0.95$ (-·-), $x/c = 0.97$ (-··-) and $x/c = 0.99$ (·····); (line-symbols: suction side, line: pressure side and experiments: □ [92]).

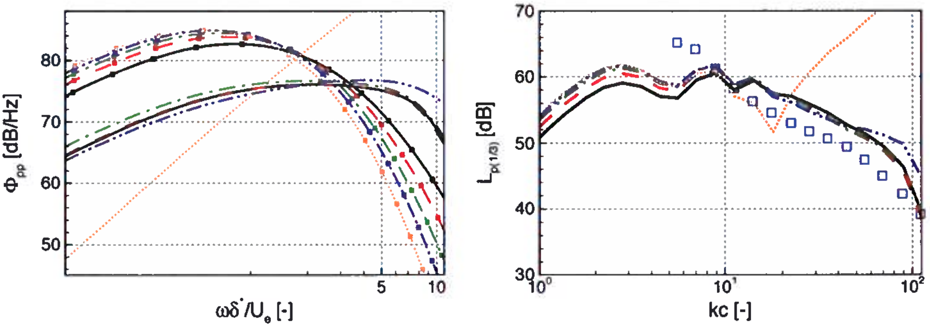

(a) Wall-pressure spectra prediction.

(b) Far-field noise prediction.

Figure 4.16: The wall-pressure spectrum predicted by the Lee [119] model and corresponding the far-field noise prediction on the DU96-W-180 airfoil varying extration position along the chord; $x/c = 0.9$ (——), $x/c = 0.93$ (- - -), $x/c = 0.95$ (-·-), $x/c = 0.97$ (-··-) and $x/c = 0.99$ (·····); (line-symbols: suction side, line: pressure side and experiments: □ [92]).

4.4. CONCLUSIONS

This study focuses on the effect of grid spacing on the wall-pressure spectra and far-field noise predicted for NACA0012 and DU96-W-180 airfoils using Amiet's linearized airfoil theory. Two categories of wall-pressure spectrum models have been investigated. Firstly, semi-empirical models have been considered, where the wall-pressure spectrum is rescaled with the mixed boundary layer variables, thus only requiring the boundary layer velocity profile (and for some models the pressure gradient) at the trailing edge. In this category, the models of Goody (assuming ZPG), and Rozenberg, Kamruzzaman, Catlett, Hu & Herr, Lee (accounting for APG effects) are compared. Secondly, an integral model

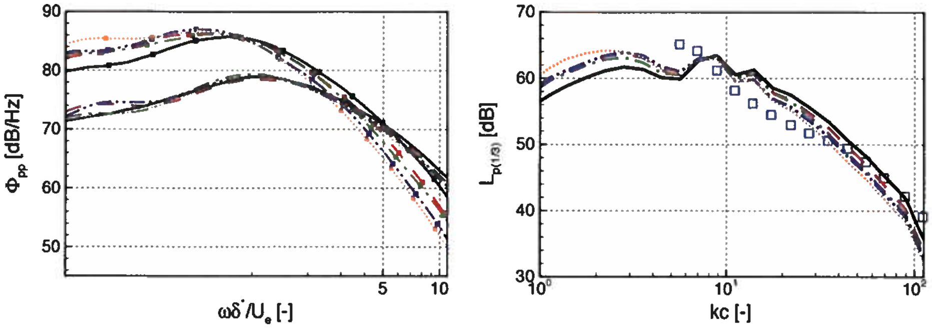

(a) Wall-pressure spectra prediction.

(b) Far-field noise prediction.

Figure 4.17: The wall-pressure spectrum predicted by the Panton & Linebarger [142] model and corresponding the far-field noise prediction on the DU96-W-180 airfoil varying extration position along the chord; $x/c = 0.9$ (——), $x/c = 0.93$ (- - -), $x/c = 0.95$ (-·-·), $x/c = 0.97$ (-···-) and $x/c = 0.99$ (·····); (line-symbols: suction side, line: pressure side and experiments: □ [92]).

proposed by Panton & Linebarger is investigated, in which the wall-pressure spectrum is obtained by integrating the Poisson equation. In addition to the mean velocity profile, this model also requires the turbulent kinetic energy and specific dissipation profiles, but is on the principle more generally applicable to flows with arbitrary pressure gradients.

The grid sensitivity analysis is performed for both airfoils with different grid resolutions characterized by the value of non-dimensional wall units, y^+, at the extraction location $x/c = 0.99$. For the NACA0012 airfoil, the coarsest grid resolution is $y^+ \simeq 10$ and for the DU96-W-180 airfoil, $y^+ = 10$ on the suction side and $y^+ = 23$ on the pressure side, and the finest grid resolution is below $y^+ < 1$ for both cases. It has been observed that the pressure coefficient appears insensitive to the mesh refinement for both airfoils. However, the boundary layer profiles showed different behaviors.

For the NACA0012 airfoil, the boundary layer velocity profile at $x/c = 0.99$ is overall insensitive to the mesh refinement, but the turbulent kinetic energy and specific dissipation profiles displayed a larger variability. A mesh independence is achieved by the Panton & Linebarger model for $y^+ < 5$. The wall-pressure spectrum predictions by the different models show that the Goody model performs poorly with respect to the experimental data, due to the presence of APG. The Rozenberg and Lee models accounting for such effects proved indeed much more accurate. The Kamruzzaman model under-predicts the low frequencies and over-predicts the higher frequencies. However, the Catlett and Hu & Herr models perform poorly since they are developed for APG flow on a flat-plate. The Panton & Linebarger model captures the slope but under-predicts the amplitude by around 3 dB. The same conclusion can be drawn for the far-field predictions.

For the DU96-W-180 airfoil, the velocity profile exhibit different trends with respect to the grid refinement, depending on the quantify of interest. The mesh resolution has a larger impact on the suction side than on the pressure side, excepted for the specific dissipation profile. In general, it has been observed that the low frequencies of the radiated spectrum are dominated by the suction side turbulent boundary layer, whereas the pressure side flow is responsible for the higher frequencies. The low-frequency part of the predicted acoustic spectrum proves accordingly to be more mesh-dependent than the high-frequency part.

In more quantitative terms, it can be concluded that for the considered airfoils and flow solver, a mesh resolution below $y^+ <23$ on the pressure side for the semi-empirical models and $y^+ <13$ for the integral model is necessary to ensure the converge the radiated noise spectrum predictions. Both Rozenberg and Lee models are not used to predict the wall-pressure spectrum on the pressure side due to the presence of FPG, in which case the Goody model is applied. Nevertheless, a better agreement with the experimental sound spectra is observed with the Lee model. The far-field noise predicted by the Kamruzzaman model over-predicts the levels by about 3 dB for frequencies above $kc > 10$. Finally, the far-field noise predicted by the Panton & Linebarger model is found to be within ± 3 dB of the experimental data, and provides the best agreement for the lowest frequencies. It shows however a slightly larger variability than the semi-empirical models.

The probe location analysis is performed with five different positions starting from $x/c = 0.9$ to $x/c = 0.99$ for the DU96-W-180 airfoil. It has been observed that the flow is exposed to an APG flow on the suction side along the airfoil whereas on the pressure side, the flow is exposed to an APG flow until $y/c = 0.95\%$ and a FPG flow after. Moreover, the wall-pressure spectrum prediction by the models showed that the suction side is more sensitive to the probe location than the pressure side as for the boundary layer profiles. In general, the far-field noise predictions by the semi-empirical models are found to be sensitive to the probe location below the frequency $kc < 10$.

5

APPLICATION TO DIFFUSER AUGMENTED WIND TURBINE (DAWT)

The CAD of the DonQi Urban Windmill shown in Fig. 5.1a is provided by the Delft University of Technology (see Ref. [9] for the detailed explanation of the geometry). The wind turbine has a radius of 0.75 m with a tip clearance of 0.015 m. The airfoil profile is a NACA2207 along the entire blade. The chord of the blade at the hub is 0.13 m with a twist angle of 40.5° and is 0.105 m with 0.3° twist at the tip. This variation is shown in Fig. 5.1b.

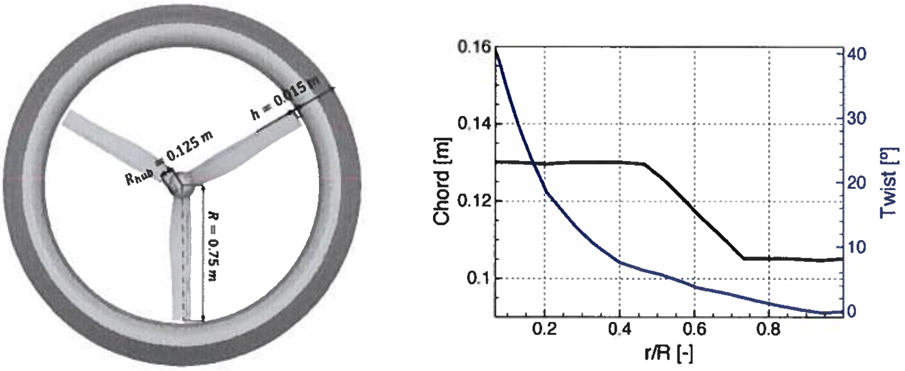

(a) (b)

Figure 5.1: (a)The geometry of the DonQi Urban Windmill; (b) The chord and twist distributions along the blade.

5.1. 3D NUMERICAL SIMULATION

In this section, a 3D simulation of the DonQi Urban Windmill is performed. The *Multiple Reference Frame* method explained as in Sec. 3 is used. The details of the computational setup are explained in the following parts.

5.1.1. COMPUTATIONAL SETUP

Steady three dimensional (3D) incompressible RANS simulations of the DonQi Urban Windmill were performed using the open source CFD solver OpenFOAM 4.0. The $k-\Omega$ SST turbulence model proposed by Menter [130] was used as described in Chapter 4, and assuming a turbulent flow along the blade, diffuser and hub. The inlet velocity and the turbulence intensity were chosen as 5 m/s and 5%, respectively, which corresponds to the operating condition for the turbine [9]. The inlet velocity is uniform and the wind turbine is symmetric around the rotational axis. Thus, only 120° of the full domain was modelled to reduce the computational effort as shown in Fig. 5.2. For the inlet and outlet, the same boundary conditions were applied as in Chapter 4 and they were placed at 8R and 7R, respectively [169] (R is the rotor radius) in front and behind the hub, respectively. A periodic boundary condition was used on the adjacent faces. The far-field boundary condition was assumed to be the same as the inlet and was placed at 8R to reduce interaction with the blade region [75]. A closer view of the MRF zone is shown in Fig. 5.2b. The rotational speed was chosen as $\Omega_{rot} = 39.84$ rad/s which is found to be an ideal operating condition with a tip speed ratio of 6 as suggested by van Dorst [192]. The blade and the hub intersection with the MRF zone were considered rotating, while, the diffuser intersection with the MRF zone was considered stationary. Furthermore, a contra-rotating velocity boundary condition was exposed to the non-rotating part of the hub, the others were set to no-slip condition. The pressure gradient was set to zero and the blended wall functions were used for the kinetic energy k, the turbulent viscosity ν_t and the specific dissipation Ω for all the solid surfaces. The boundary conditions with the initial values are summarized in Table 5.1.

5.1.2. MESH SENSITIVITY

The mesh was created using the ANSYS MESHING 19.0 tool by using the multizone utilitiy. The domain is subdivided into several blocks, where the outer blocks are composed of a hexadral mesh while a tetrahedral mesh is used for the inner blocks. A detail sketch of the mesh is shown in Fig. 5.3. Three different meshes were created by changing only the first cell thickness, while keeping the surface mesh identical. Thus, the number of the cells for each mesh configurations is sensitive to the first layer cell thickness. It can be deduced from Table 5.2 that the y^+ value for the finest mesh is in the inner layer whereas the medium and coarse ones are extended to the buffer layer.

To investigate the effect of mesh resolution on the blade, three strip positions are chosen: close to the hub ($x/R = 0.19$), at midspan ($x/R = 0.55$) and close to the tip ($x/R = 0.92$) which are demonstrated in Fig. 5.4. The pressure coefficient is calculated as:

$$C_p = \frac{p - p_0}{\frac{1}{2}\rho_0 U_{Rel}^2} \tag{5.1}$$

where p_0 and ρ_0 are the pressure and density at the atmospheric conditions. The relative

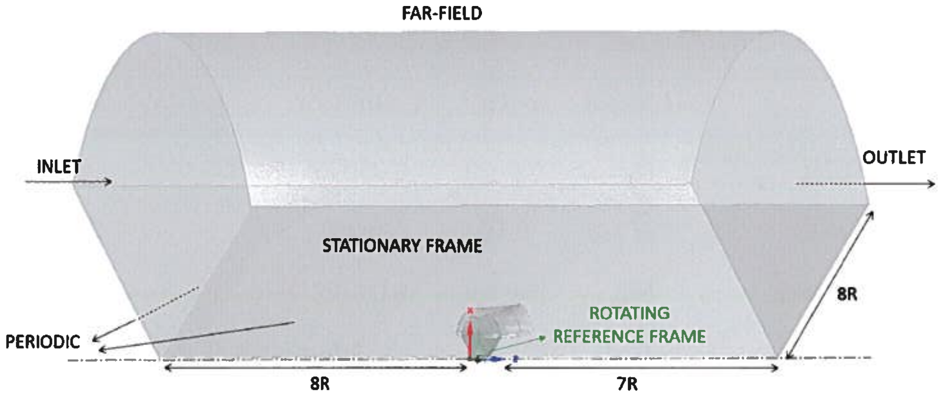

(a) Computational domain.

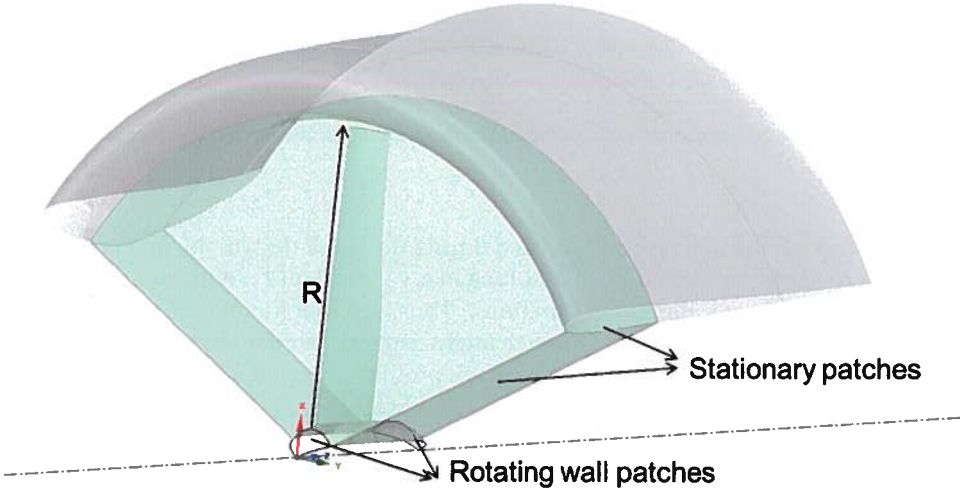

(b) MRF region.

Figure 5.2: Computational domain.

velocity is defined as: $U_{Rel} = \sqrt{U_{\infty}^2 + (\Omega_{rot} \cdot r_{strip})^2}$ depending on the strip location. The pressure coefficient as a function of mesh resolution is shown in Fig. 5.5 at the three strip locations. It is observed that the pressure coefficient remains unchanged for the three mesh resolutions along the blade sections.

The dimensionless velocity, turbulent kinetic energy and specific dissipation boundary layer profiles extracted at $x/c = 0.99$ from the leading edge with different mesh resolutions are given in Fig. 5.6, 5.7 and 5.8 at the three strip locations, respectively. The axial velocity profile shows a good match at the outer layer of the boundary layer, however, small discrepancies are observed for the inner and log-layer. It should be noted

Table 5.1: Boundary conditions

	U $[m/s]$	p [Pa]	k_t $[m^2/s^2]$	ν_t $[m^2/s]$	Ω [1/s]
Inlet	U_∞	$\nabla P = 0$	0.09375	-	111.8
Outlet	$\nabla \vec{U} = 0$	P =0	$\nabla k = 0$	-	$\nabla \Omega = 0$
Far-field	U_∞	$\nabla P = 0$	0.09375	-	111.8
Blade	$\vec{U} = 0$	$\nabla P = 0$	Adaptive wall-function		
Diffuser	$\vec{U} = 0$	$\nabla P = 0$	Adaptive wall-function		
Hub non-rotating	Ω_{rot}	$\nabla P = 0$	Adaptive wall-function		
Hub rotating	$\vec{U} = 0$	$\nabla P = 0$	Adaptive wall-function		
Side patches	cylicAMI				

that even though the first layer cell is fixed during the mesh design, the first cell height decreases towards the trailing-edge, resulting in a y^+ less than 1 along the trailing-edge region for the different mesh configurations. Thus, the wall function is not employed since the boundary layer is resolved which might explain the different behavior for each mesh resolution. The turbulent kinetic energy profiles extracted at the same positions show high sensitivity to the mesh resolution. It could be observed that the difference between the mesh resolutions decreases from the hub to tip. The reason behind this may be due to the occurrence of secondary flows at the hub. The turbulence model might be more sensitive to the different mesh resolution in such a flow. Furthermore, the peak point decreases with a finer mesh which is contrary to the outcome analysed in Sec. 4.2. Contrary to the other boundary layer profiles, the specific dissipation profiles exhibit in-

Table 5.2: Wall normal spacing for the blade

$\Delta y/c \times 10^3$	Number of cells	Min. y^+	Max. y^+	Average y^+
0.08	49 618 393	0.07	8	2.5
0.06	52 267 244	0.063	7	2
0.05	53 762 184	0.06	6	1.6

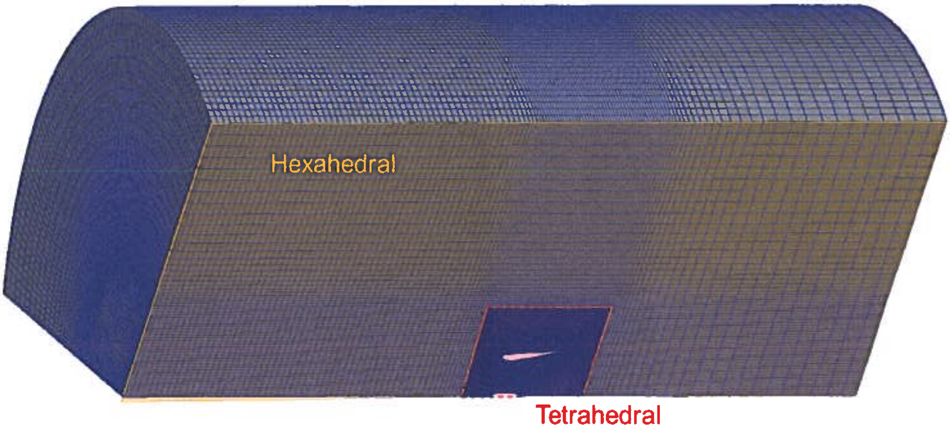

Figure 5.3: The tetrahedral mesh within the hexahedral mesh.

sensitivity to the mesh resolution. The wall-normal and spanwise velocity profiles are given in Appendix B.1.

5.2. 2D ISORADIAL APPROACH

The main focus of this section is to investigate the applicability of the 2D isoradial approach which would reduce 3D computational effort in terms of both meshing and simulation cost. For this end, the isoradial methodology introduced in Sec. 3.5.1 is applied. As a first step, the effect of the nacelle and the diffuser on the flow acceleration is neglected and it is assumed that each isoradial blade section encounters the same free-stream velocity, which is applied in the previous section for three-dimensional simulations. The 2D computational setup based on this approach is explained, and followed by the analysis on the number of strips required for a converged acoustic results by excluding the scattering due to the nacelle and diffuser. Later, in order to represent the effect of the diffuser and the nacelle on the inflow conditions due to the acceleration, a two-dimensional axisymmetric simulation is performed to obtain the inflow conditions for two-dimensional approach. This approach is indicated in Fig. 5.9. The flow acceleration along the diffuser is investigated.

5.2.1. COMPUTATIONAL SETUP

The solver and turbulence model described in Chapter 4 were used, as well as the same boundary conditions except for the top and bottom part of the domain. In this case, cyclic boundary conditions (cyclicAMI) were applied to take into account the periodicity. The inlet and outlet were placed 3c upstream and downstream of the airfoil. However, the distance between the top and bottom parts were modified depending on the radial position of the isoradial blade cut to satisfy the periodicity. For the simplification of the geometry, it is assumed that the axial velocity is unchanged along the axial direction. Thus, all the initial conditions given in Table 5.1 were kept the same. In addition,

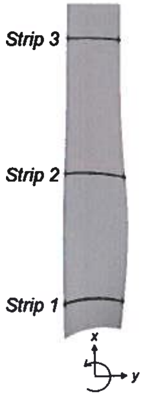

Figure 5.4: Three strip positions.

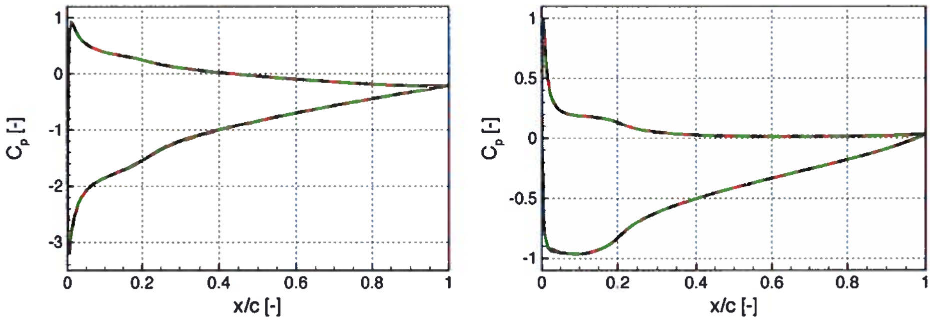

(a) Strip 1.

(b) Strip 2.

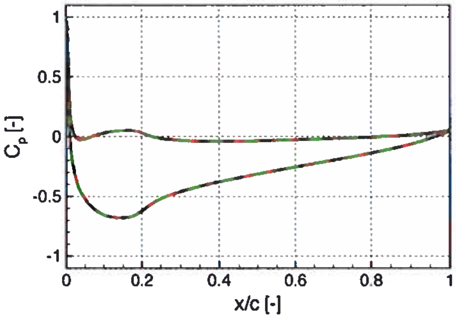

(c) Strip 3.

Figure 5.5: Pressure coefficient along the airfoil at each strip location with different mesh resolutions; $y^+_{ave} \simeq 2.5$ (——), $y^+_{ave} \simeq 2$ (- - -), $y^+_{ave} \simeq 1.6$ (-·-).

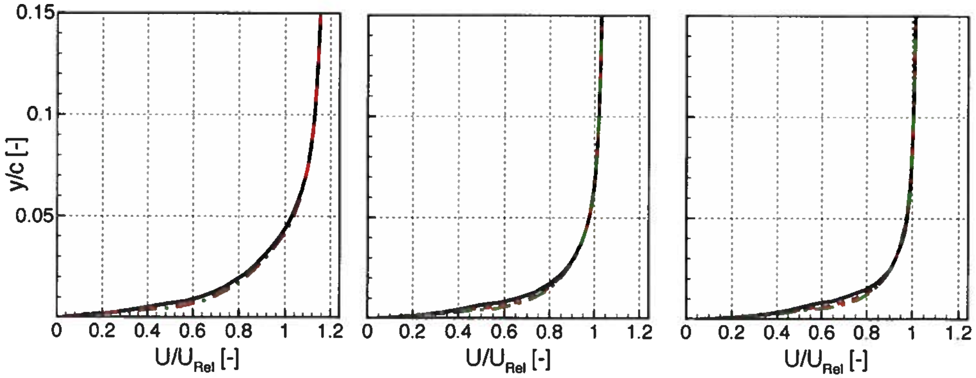

(a) Strip 1. (b) Strip 2. (c) Strip 3.

Figure 5.6: Axial velocity profiles at x/c =0.99 from the leading edge at each strip location with different mesh resolutions; $y^+_{ave} \simeq 2.5$ (——), $y^+_{ave} \simeq 2$ (- - -), $y^+_{ave} \simeq 1.6$ (-·-·).

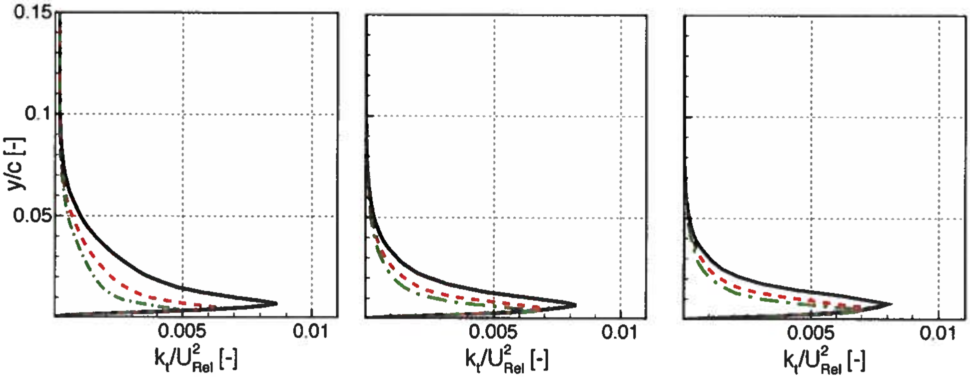

(a) Strip 1. (b) Strip 2. (c) Strip 3.

Figure 5.7: Turbulent kinetic energy profiles at x/c =0.99 from the leading edge at each strip location; $y^+_{ave} \simeq 2.5$ (——), $y^+_{ave} \simeq 2$ (- - -), $y^+_{ave} \simeq 1.6$ (-·-·).

a tangential velocity was introduced due to the rotational speed of the blade which depends on the strip position, $V = \Omega_{rot} \cdot r_{strip}$. A sketch shown in Fig. 5.10 illustrates the aforementioned conditions.

5.2.2. CONVERGENCE DUE TO THE NUMBER OF STRIPS

To obtain a converged solution for the far-field spectrum, the blade is divided into 5, 10 and 20 as shown in Fig. 5.11. The boundary layer profiles normal to the airfoil surface close to the trailing-edge are obtained for each strip from the 2D RANS simulations. The

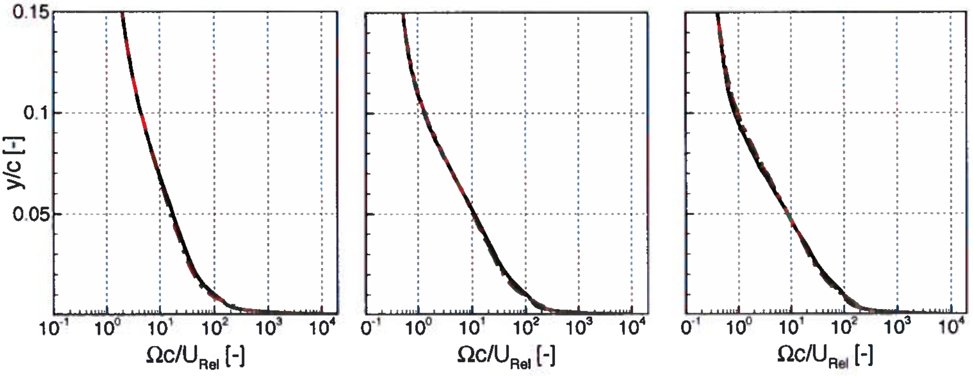

(a) Strip 1. (b) Strip 2. (c) Strip 3.

Figure 5.8: Specific dissipation profiles at x/c =0.99 from the leading edge at each strip location; $y^+_{ave} \simeq 2.5$ (——), $y^+_{ave} \simeq 2$ (- - -), $y^+_{ave} \simeq 1.6$ (-·-·).

corresponding wall-pressure spectrum is computed by the Panton and Linebarger [142] model. The other models introduced in Sec. 3.4 are not considered as this model is found to account for alterations of the boundary layer profiles with a better accuracy than the others. It should be noted that for the spanwise correlation length and the convective velocity are assumed to be the same for all the strips along the blade as described in Sec. 3.1. To obtain uncorrelated contributions from each strips, the spanwise correlation length should be smaller than the strip span, $l_y < L$. Considering the maximum strip number ($L = 0.03$ m) with the maximum velocity at the tip of the blade ($U = 30$ m/s), the minimum frequency from the Eq. 3.2 for uncorrelated strips is found to be $f = 143$ Hz.

The far-field noise prediction at 1 m and 10 m (x, y, z=0, 0, 1-10) downstream of the blade is given in Fig. 5.12 for 5, 10 and 20 strips. It has been observed that beyond the compact regime (kc >1), the predictions from different strips give similar results. However at the high frequencies, $kc > 25$, the predictions from the 5 strips configuration at a 1 m observer location deviates by 2 dB from the other strip configurations, as the observer position is not located at the geometrical far-field $z/R \approx 1$. According to Amiet's formulation, the observer has to be located at the acoustical and geometrical far-field position. Thus, considering the only observer position at 10 m, it is concluded that 5 strips are enough to have a converged solution. The deviation for 20 strips that are observed below $kc < 1$ are due to insufficient sampling issues related to the Monte-Carlo integration as mentioned in Sec. 4.2.3.

5.2.3. IMPROVING THE INFLOW CONDITIONS

In Sec. 5.2.1, it was mentioned that the free-stream velocity was imposed as an inlet velocity for each strip position assuming that the diffuser and nacelle do not change the axial velocity. However, adding a diffuser and nacelle create a circulation around them which accelerates the flow. To investigate the evolution of the flow fluid along the dif-

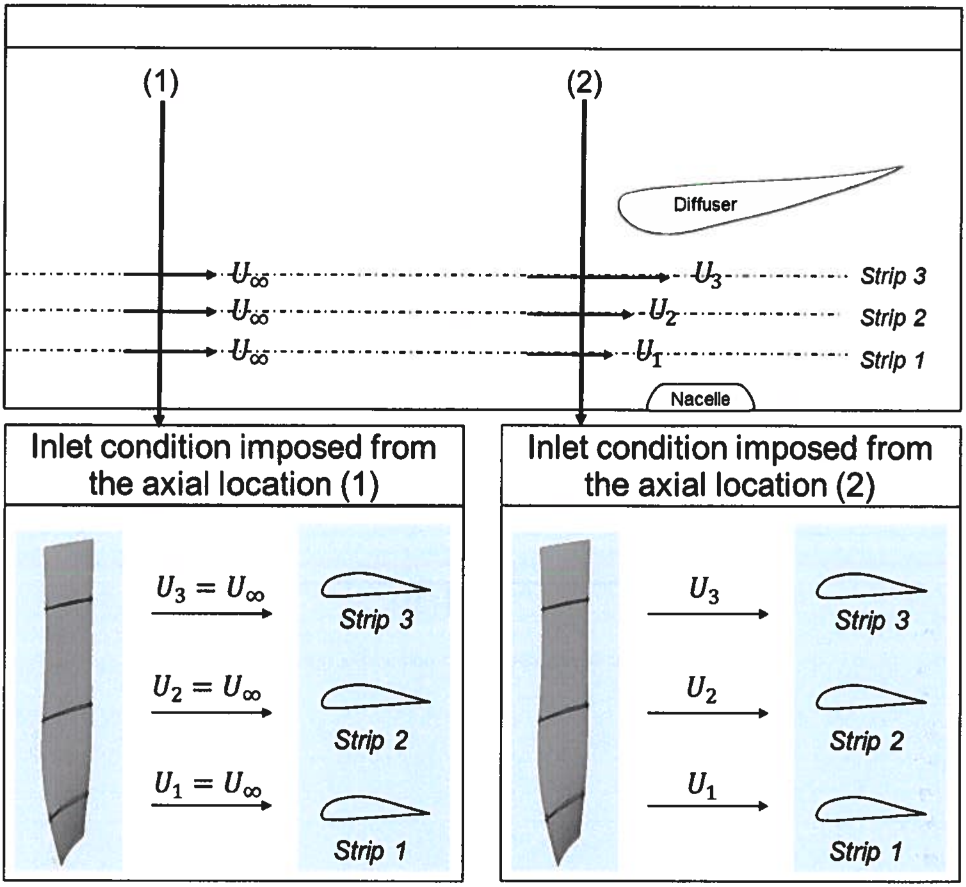

Figure 5.9: The 2D isoradial approach with the acceleration correction from a 2D axisymmetric simulation.

fuser, an axisymmetric 2D simulation was performed by neglecting the blade as shown in Fig. 5.13.

The domain size was kept the same as the 3D simulation except for the cyclic angle. In this case, the cyclic angle was 5° with a thickness of one cell in order to use the wedge utility of OpenFoam 4.0. The same initial and boundary conditions were applied for other boundaries. A structured mesh was created with ANSYS ICEM. The wall-normal resolution is determined to be less than $y^+ < 5$ for both diffuser and nacelle.

The same strip locations as shown in Fig. 5.4 were used to investigate the flow acceleration along the diffuser. The dimensionless mean velocity profiles in the polar coordinate system along the diffuser are given in Fig. 5.14 where U_z is the axial velocity, U_r is the radial velocity, U_θ tangential velocity, z corresponds to the axis of symmetry and c is the mid-chord of the blade. The origin, $z/c = 0$, is located on the tip of the nacelle front. The diffuser, blade, nacelle and probe locations are described in Fig. 5.14(a). It has been observed that the flow acceleration starts around $z/c \simeq -1$ and has its maximum

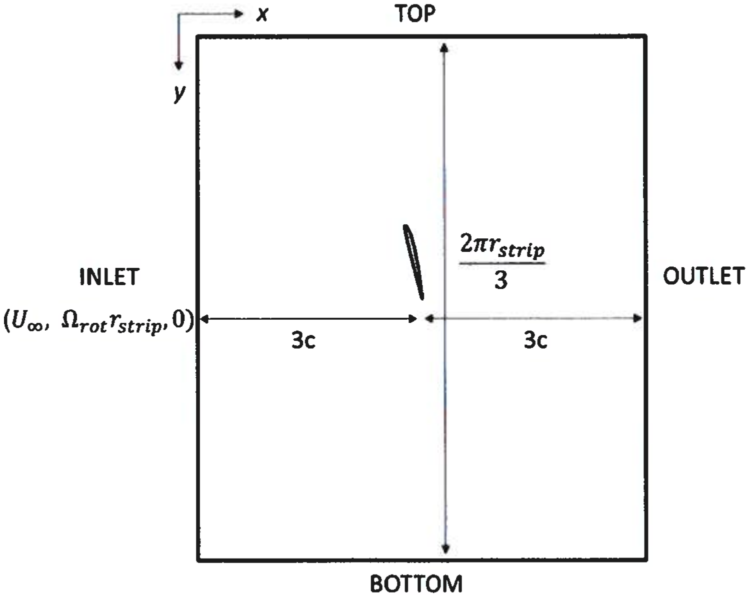

Figure 5.10: Computational setup for 2D approach.

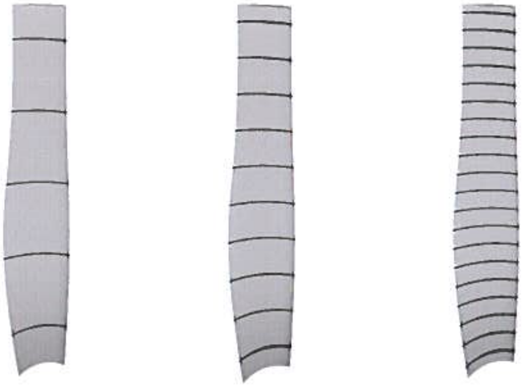

(a) 5 strips. (b) 10 strips. (c) 20 strips.

Figure 5.11: Isoradial blade cuts of the DonQi Urban Windmill.

at the location of minimum area. Surprisingly, the first and second strips' axial accelerations are almost identical. One might expect to observe less influence on the second strip due to the circulation around the diffuser and the nacelle if the distance between them would be larger. Furthermore, the diffuser has a high curvature on the suction side which leads to a greater acceleration and thus, resulting in a higher axial velocity at

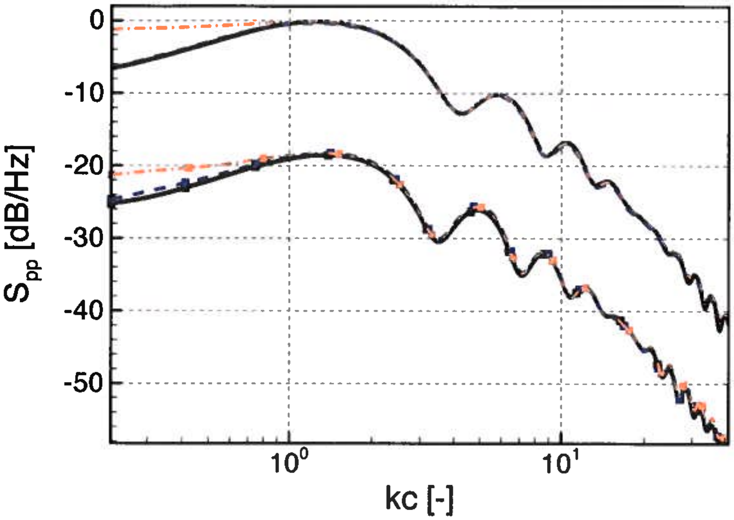

Figure 5.12: Far-field noise prediction at two observer locations (line: 1 m, line-symbols: 10 m) with 5 strips (——), 10 strips (- - -) and 20 strips (- · · -).

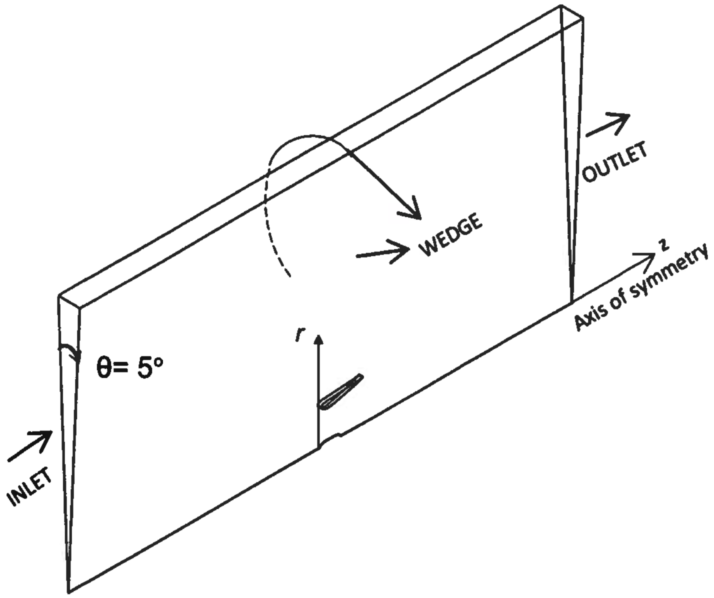

Figure 5.13: Computational setup for 2D axisymmetric simulation.

the midspan. The radial velocity profile shows similar results at the midspan, while the tip strip locations have a negative radial velocity component at the inlet of the diffuser which signify that both locations are mainly driven by the flow on the suction side of the diffuser. Furthermore, the absolute value of the radial component at the midspan is greater than the strip location near the nacelle which means that the acceleration due to the diffuser is dominant. After the minimum area location, the flow starts to decelerate for all the strip locations. Further downstream, at $z/c = 8$, it is observed that the radial component is less pronounced for the nacelle strip location, however, the midspan and tip strip locations are still driven by the flow around the diffuser. Finally, the tangential velocity along each strip location is found to be zero as the rotation is neglected in this configuration.

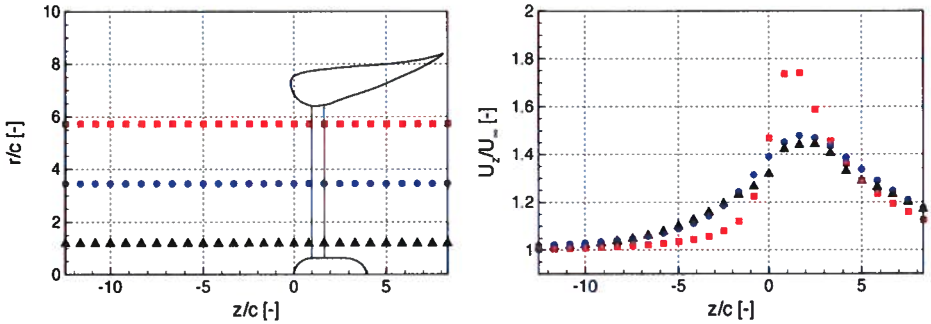

(a) The location of the strip and probes.

(b) Mean axial velocity.

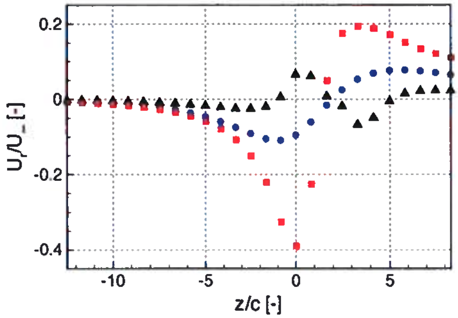

(c) Mean radial velocity.

Figure 5.14: The probe locations and mean velocity profiles along the diffuser with respect to the different strip locations; *Strip 1* (▲), *Strip 2* (●) and *Strip 3* (■).

5.3. COMPARISON OF THE 3D AND 2D COMPUTATIONS

In this section, the comparison of the 3D and 2D simulations will be assessed in terms of the incoming velocity profile upstream of the blade, the pressure coefficient and the boundary layer profiles along each strip location. Later, the wall-pressure spectrum will be obtained by using the models explained in Sec. 3 and the corresponding far-field noise prediction by Amiet's theory.

As described in the previous sections, as a first approximation for 2D computations, the diffuser and nacelle are neglected and the free-stream velocity is assumed to be uniform along the blade. However, the mean axial flow accelerates in the presence of both diffuser and nacelle. To consider this axial velocity acceleration on the 2D computational domain, three different locations are selected from the 2D axisymmetric simulations and imposed as U_∞ as shown in Fig. 5.10 with the same domain size. The first location is chosen such that the effect of the axial velocity acceleration is less than $U_z/U_\infty < 1.15$, the second location is selected before the front tip of the diffuser and the last location is chosen so that the maximum velocity could be obtained before the blade (see Fig. 5.13 at $z/c = -5.0$, $z/c = -0.5$ and $z/c = 0.677$, respectively). The three extraction locations and corresponding free-stream velocity values, as well as the base configuration are summarized in Table 5.3 with the same strip locations analysed in the previous sections. It will be these three velocities at $z/c = [-5.0, -0.5, 0.677]$ that will be imposed in the following section. It should be noted that the far-field noise predictions, the 5 strip configuration shown in Fig. 5.11(a) is used. The strip positions are numbered as *Strip 1* near the hub till *Strip 5* near the tip.

Table 5.3: The extraction locations and corresponding inlet velocity boundary conditions

z/c [-]	$U_{z/c}$ [m/s]			$U_{z/c}/U_\infty$ [-]		
	Strip 1	*Strip 3*	*Strip 5*	*Strip 1*	*Strip 3*	*Strip 5*
$-\infty$	5	5	5	1	1	1
-5.0	5.5	5.4	5.2	1.1	1.08	1.04
-0.5	6.4	6.7	6.2	1.28	1.34	1.24
0.667	7	7.2	8.5	1.4	1.44	1.7

5.3.1. INLET VELOCITY PROFILES

The inlet velocity profiles obtained from the 2D simulations with different inlet velocity boundary conditions (specified in Table 5.3), and the 3D simulation are compared in terms of the axial and tangential velocity in Fig. 5.15 and Fig. 5.16, respectively. The inlet velocity profiles are extracted at $z/c = 0.667$ and plotted as a function of the azimuthal angle, θ, which is 1/3 of the domain. The comparison is performed for the same strip locations investigated in the previous sections (see Fig. 5.4) with respect to different inlet velocity profiles obtained from the 2D and 3D simulations. However, the radial inlet velocity shown in Fig. 5.17 is compared only with respect to the different strip locations since the radial component of the velocity is neglected in 2D simulation. In all the figures, the trailing-edge location is positioned at $\theta = 0$ rad.

As a general remark, assuming the free-stream velocity as an inlet boundary condition, the mean axial velocity profile obtained by the 2D simulation under-predicts the inlet profile from 3D simulation. However, imposing the maximum velocity to the 2D simulation clearly over-predicts the inlet axial velocity profile when compared to the 3D simulation. Hence, an inlet velocity between the two extreme positions might able to reconstruct the same inlet profile from 2D simulations. Consequently, the positions at $z/c = -5.0$ and $z/c = -0.5$ are chosen to this end. Even though the velocity obtained at $z/c = -5.0$ is 1.1 times higher than the free-stream velocity, $U/U_\infty = 1.1$, the inlet axial profile for *Strip 1* is over-predicted and for *Strip 5* is under-predicted whereas a good match is observed for *Strip 3* in comparison to the 3D results. Finally, for *Strip 5*, the inlet velocity profile obtained from the 2D simulation by imposing the axial velocity at $U_{z/c} = -0.5$ has a good match. The tangential mean velocity profiles non-dimensionalized with the rotational speed shows that the profiles obtained from the 2D simulations perform poorly with respect to the 3D simulation. In all strip positions, the peak point of the 2D profiles is shifted to the left in comparison with the 3D result. The inlet radial velocity component is investigated only for 3D simulations with respect to the different strip positions as shown in Fig. 5.17 as the 2D simulation does not take into account the spanwise evaluation. When the inlet radial velocity profiles are compared with the 2D axisymmetric simulations shown in Fig. 5.14c at $z/c = 0.667$, it is observed that the mean of the velocity is lower. Furthermore, the midspan location is less affected by the circulation due to the diffuser as the mean radial velocity is around $U_r/U_\infty = 0.025$. It could be concluded that the presence of the blade and the rotation reduce the radial velocity component. However, it is difficult with the current studies to interpret the magnitude of impact on the results.

5.3.2. PRESSURE DISTRIBUTION AND BOUNDARY LAYER PROFILES

Another way to verify the inlet boundary conditions is to observe the pressure distribution along the airfoil. Thus, the same analysis is performed by comparing 3D simulation to 2D simulations with different inlet velocity boundary condition values at three different strip locations given in Fig. 5.18. In 2D simulations, the axial velocity is increased while keeping the rotational speed the same. Therefore, the angle of attack gets steeper when the axial velocity increases which results in a higher lift. This behavior is observed for all the strip locations. In addition, for *Strip 1*, a decrease in the pressure distribution is observed due to the separation near the trailing edge which is caused by a higher angle of attack. When reproduction of the pressure distribution is concerned, it is observed that for *Strip 1*, whatever the inlet velocity is, the C_p distribution is shifted downwards except for the stall case. This behavior is explained by several authors [18, 36, 64, 126] due to the Coriolis and centrifugal effects in 3D simulations in contrast with the 2D simulation of a conventional horizontal wind turbine at the same operating conditions. They have observed that the separated flow near the hub region is moved towards the midspan of the blade due to the centrifugal forces which result in a reduced wake size, and thus, a thin boundary layer. When the boundary layer reduces, the velocity on the suction side increases which reduces the pressure along the blade. Furthermore, the Coriolis force acts in the chorwise direction and delays the separation point to towards the trailing-edge. In

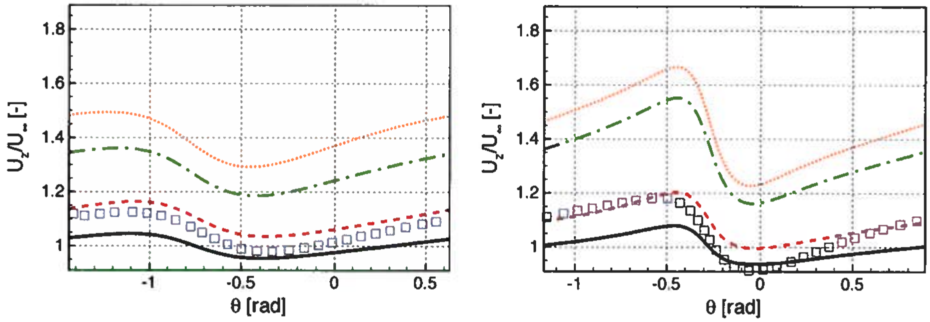

(a) Strip 1.

(b) Strip 3.

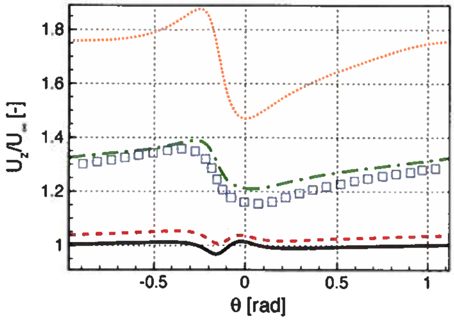

(c) Strip 5.

Figure 5.15: Axial mean velocity profile extracted at $z/c = 0.667$ with respect to each strip location and with different imposed velocities given in Table 5.3; $U_{z/c=-\infty}$ (——), $U_{z/c=-5.0}$ (- - -), $U_{z/c=-0.5}$ (-·-), $U_{z/c=0.667}$ (·····) and 3D simulation (□).

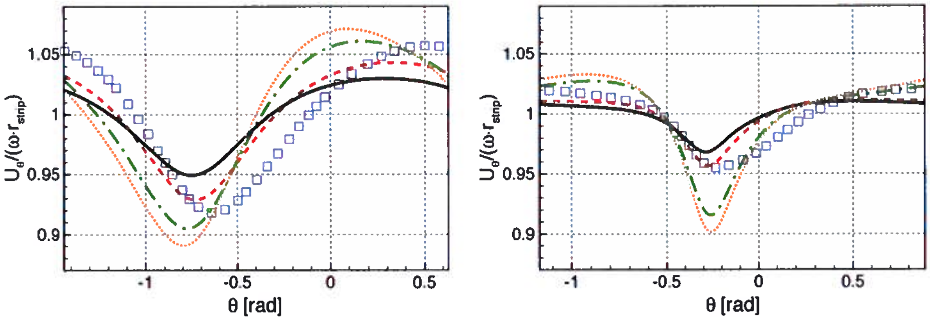

(a) Strip 1.

(b) Strip 3.

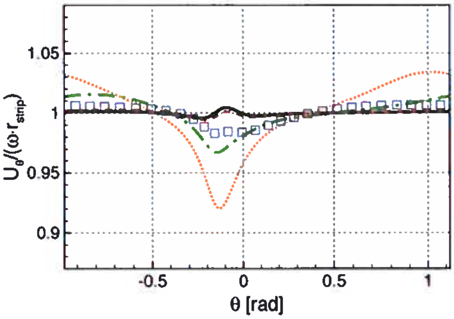

(c) Strip 5.

Figure 5.16: Tangential mean velocity profile extracted at $z/c = 0.667$ with respect to each strip location and with different imposed velocities given in Table 5.3; $U_{z/c} = -\infty$ (——), $U_{z/c=-5.0}$ (- - -), $U_{z/c=-0.5}$ (-·-), $U_{z/c=0.667}$ (·····) and 3D simulation (□).

addition, it is found that these effects become less pronounced towards the outer portion of the blade. This statement can be observed for *Strip 3* and *Strip 5* where a better match is obtained for the pressure distribution. Even though, the inlet velocity profile obtained by $U_{z/c=-5.0}$ shows a better agreement with 3D simulation, it is seen that the shape of the C_p distribution is different for that velocity. Furthermore, at this strip location, it was already verified that the radial velocity component is weak which should have reproduced a better match. Again, it is observed that changing only the axial velocity is unable to reproduce the pressure coefficient. Contrary to the other strip locations, *Strip 3* is able to reconstruct the pressure distribution from the 2D simulation by imposing the velocity at $U_{z/c=-0.5}$.

The mean axial velocity boundary layer profiles extracted at $x/c = 0.99$ from the leading edge of each blade section are given in Fig. 5.19. As a general observation, the velocity profiles obtained from the 2D simulations are exposed to a higher pressure gradient compared to the 3D case. The reason behind this, as mentioned before,might be due to the Coriolis forces which act in the chordwise direction and have a favorable pressure ef-

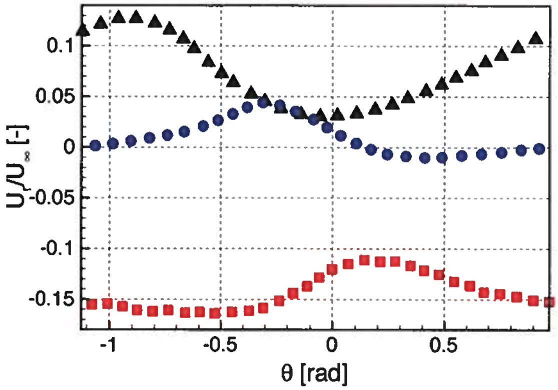

Figure 5.17: Radial mean velocity profile at z/c =0.667 with respect to each strip location; *Strip 1* (▲), *Strip 3* (●) and *Strip 5* (■).

fect. For *Strip 1*, the velocity profiles obtained from $U_{z/c=-0.5}$ and $U_{z/c=0.667}$ demonstrate separation as also seen from the C_p distribution since this region has a higher pitch angle than the other strip locations. For *Strip 3* & *Strip 5*, a good match is observed at the outer part of the boundary layer in comparison with the 3D simulation. In terms of the inlet velocity profile and pressure distribution, the results obtained at $U_{z/c=-0.5}$ have a better agreement for *Strip 5* in comparison with the 3D simulation, however, this does not hold true for the boundary layer profile. The global boundary layer variables are given in Table 5.4 for $U_{z/c=-\infty}$, $U_{z/c=-5.0}$, $U_{z/c=-0.5}$ and 3D simulation. Since the boundary layer profile obtained from $U_{z/c=0.667}$ does not match with the 3D simulation, the values for this case are given Appendix B.3. From Table 5.4, it is observed that in general the boundary layer thickness, δ and wake parameters, Π & β which are obtained from 3D simulations are higher than the 2D simulations while the integral boundary layer variables such as the displacement and momentum thickness values as well as the external and friction velocity seem close to each other. However, most of the wall-pressure models are highly dependent on the wake parameters which indicates that 3D wall-pressure spectrum predictions might deviate from the 2D predictions. The boundary layer variables obtained from $U_{z/c=-0.5}$ show that there is a separation for the strip location near the hub which can also be depicted from the boundary layer velocity profiles.

Additionally, the kinetic energy profiles are over-predicted by the 2D simulations (see Appendix B.2). The reason might be due to fact the secondary flow effects are not present in 2D simulation. Thus, the wall-pressure spectrum predicted by the Panton & Linebarger model will deviate significantly from the 3D predictions especially for the low frequencies for the suction side.

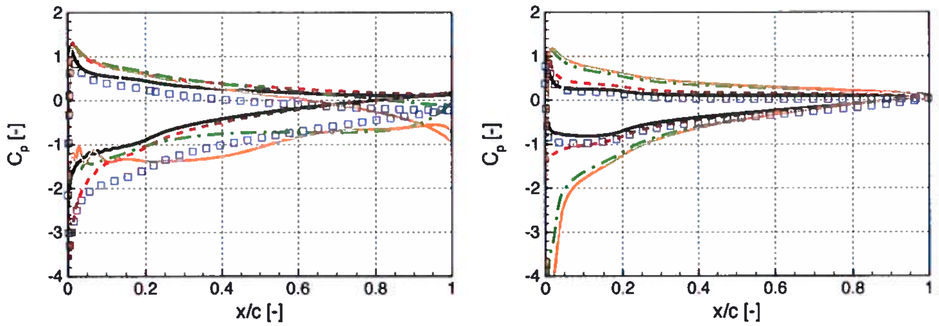

(a) Strip 1.

(b) Strip 3.

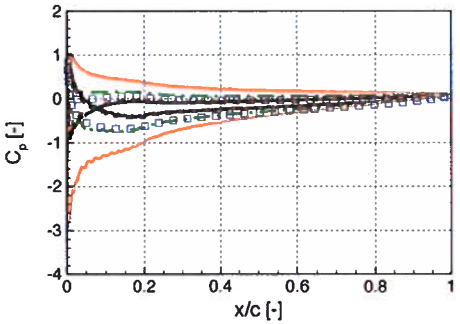

(c) Strip 5.

Figure 5.18: Pressure coefficient along each strip location; $U_{z/c=-\infty}$ (—), $U_{z/c=-5.0}$ (- - -), $U_{z/c=-0.5}$ (-·-), $U_{z/c=0.667}$ (·····) and 3D simulation (□).

5.3.3. PREDICTION OF THE WALL-PRESSURE SPECTRA AND FAR-FIELD TRAILING EDGE NOISE

The wall-pressure spectrum prediction is performed by the Kamruzzaman, Lee, and Panton & Linebarger models for the same three strip positions that were investigated in the previous section: a strip close to the hub *Strip 1*, a strip in the middle of the blade *Strip 3* and a strip near the tip region *Strip 5*. The wall-pressure spectrum is calculated from $U_{z/c=-\infty}$ and $U_{z/c=-5.0}$ for the *Strip 1* and *Strip 3* locations, while for *Strip 5*, $U_{z/c=0.5}$ is also added since it provides a better match for C_p and U_e (shown in Fig. 5.18 and 5.19).

The dimensionless frequency for the wall-pressure spectrum is expressed by $\omega\delta^*/U_e$ where the global boundary layer variables on the suction side are obtained from 3D simulations. Figure 5.20 shows the prediction for *Strip 1* on suction side (a) and the pressure side (b). When the 3D simulation is considered on the suction side, a decay seems to occur for the prediction obtained both from the Kamruzzaman and Lee model while, the Panton & Linebarger model under-predicts for the frequencies below $\omega\delta^*/U_e < 10$. For 2D simulations, it is observed that the Kamruzzaman and Panton & Linebarger model

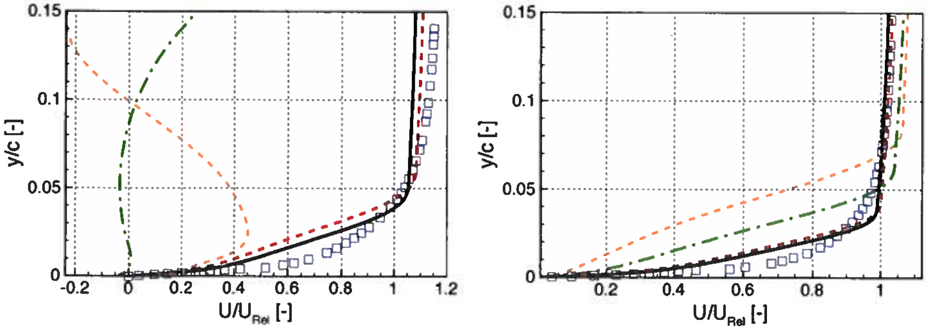

(a) Strip 1.

(b) Strip 3.

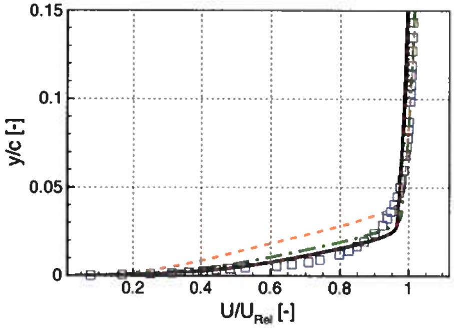

(c) Strip 5.

Figure 5.19: Mean axial boundary layer profile extracted at x/c =0.99 with respect to each strip location; $U_{z/c=-\infty}$ (——), $U_{z/c=-5.0}$ (- - -), $U_{z/c=-0.5}$ (-·-), $U_{z/c=0.667}$ (·····) and 3D simulation (□).

seem insensitive to the velocity increase while a significant increase is observed for the Lee model above $\omega\delta^*/U_e > 7$. On the pressure side, the predictions obtained from 3D simulation exhibits a similar decay, however, with different amplitudes. Likewise, the Panton & Linebarger model under-predicted the wall-pressure spectrum with respect to the other models. When the 2D simulations are compared, it is observed that increasing velocity shifts the amplitude for the frequencies above around $\omega\delta^*/U_e \approx 2$. Overall, the wall-pressure spectrum obtained by the Kamruzzaman model gives closer results with 2D and 3D simulations especially for $U_{z/c=-5.0}$.

The wall-pressure spectrum prediction for *Strip 3* is given in Fig. 5.21 for the suction side (a) and pressure side (b). The predictions obtained the Kamruzzaman and Lee models exhibit a similar decay for the high frequencies above $\omega\delta^*/U_e < 7$ for the 3D simulation on the suction side. Similarly, the Panton & Linebarger model under-predicts the amplitude for the low frequencies. The predictions obtained from the 2D simulations are insensitive to the velocity increase even though this increase was significant for the inlet profiles and pressure coefficient as mentioned previously. The predictions obtained from each model are unable to exhibit a similar curve with the 2D and 3D simulations.

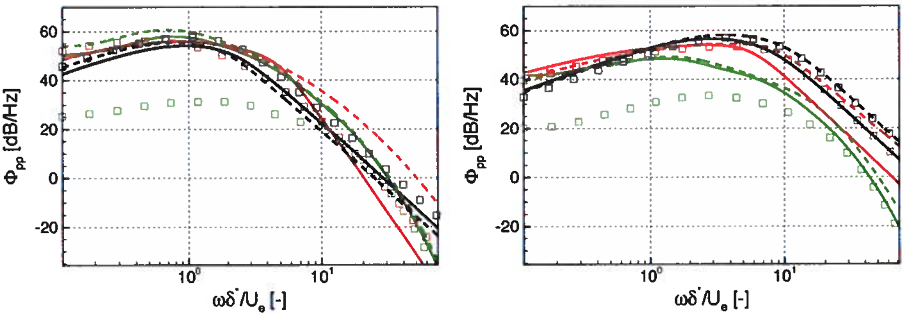

(a) Suction side.

(b) Pressure side.

Figure 5.20: The wall-pressure spectrum predicted by the Kamruzzaman model (black), the Lee model (red) and the Panton & Linebarger model (green) from $U_{z/c=-\infty}$ (solid line), $U_{z/c=-5.0}$ (dashed line) and 3D simulation (rectangle) at *Strip 1*.

On the contrary, the pressure side predictions for the 3D simulations shows a similar slope, however, under-prediction occurs for the Panton & Linebarger model. The wall-pressure prediction obtained from 3D simulations of the Kamruzzaman and Lee models show a better match with their predictions except for the Lee model which yields inconsistent results for higher frequencies. Overall, the Kamruzzaman model gives the most consistent prediction.

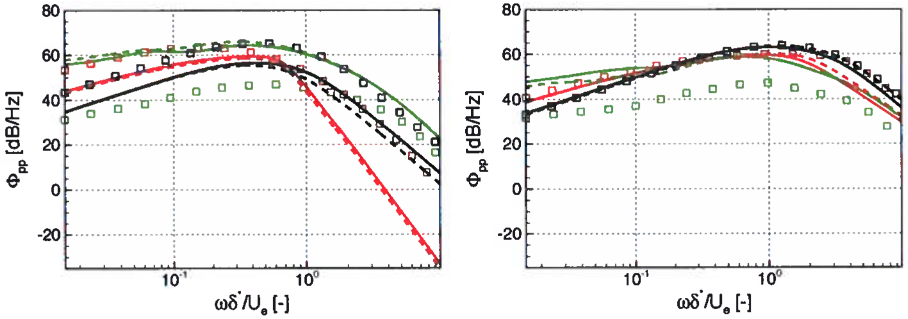

(a) Suction side.

(b) Pressure side.

Figure 5.21: The wall-pressure spectrum predicted by the Kamruzzaman model (black), the Lee model (red), and the Panton & Linebarger model (green) from $U_{z/c=-\infty}$ (solid line), $U_{z/c=-5.0}$ (dashed line) and 3D simulation (rectangle) at *Strip 3*.

The same predictions are performed for *Strip 5*, in addition, the wall-pressure spectrum obtained from $U_{z/c=-0.5}$ is also analyzed. The wall-pressure spectrum obtained from the 3D simulation with different models do not provide the same behavior for the suction side. The wall-pressure spectrum obtained from the 2D simulations show that when the velocity increases the amplitude decreases for the higher frequencies for all the models. For the pressure side, the Lee and Panton & Linebarger model exhibit a similar slope behavior with different amplitudes. Moreover, the frequencies above $\omega\delta^*/U_e > 1$ perform the a similar decay for all the models. In general, it is observed that increasing the velocity, decreases the amplitude for the low frequencies while increasing the amplitude for the higher frequencies except for the Panton & Linebarger model which seems insensitive to the velocity augmentation. Similar to the other *Strips*, the Kamruzzaman model prediction gives similar results for 2D and 3D simulations. As a general remark, similar to Chapter 4, the pressure side contributes more to the higher frequencies whereas the low frequencies are dominated by the suction side. When the different strip positions are compared, although the *Strip 5* is exposed to a higher tangential velocity, the magnitude of the spectrum seems to be closer with respect to the other strip locations. Furthermore, the low frequency range has almost the same amplitude for all the strip locations, which means that they will contribute significantly to the far-field noise spectrum. While for the high frequency range, the contribution from the last three strips is enough to have the same amplitude. This is demonstrated in Fig. 5.23.

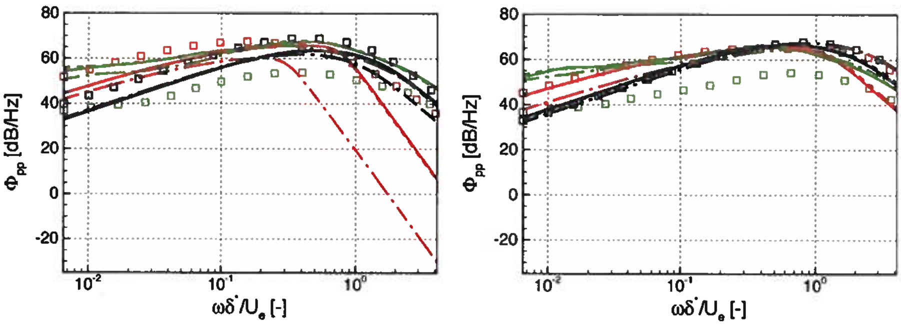

(a) Suction side.

(b) Pressure side.

Figure 5.22: The wall-pressure spectrum predicted by the Kamruzzaman model (black), the Lee model (red), and the Panton & Linebarger model (green) from $U_{z/c=-\infty}$ (solid line), $U_{z/c=-5.0}$ (dashed line), $U_{z/c=-0.5}$ (dashed dotted line) and 3D simulation (rectangle) at *Strip 5*.

One-third octave band far-field noise spectrum predicted at two locations are given in Fig. 5.24; downstream of the wind turbine (a) and upstream of the wind turbine (b). As mentioned previously, the far-field noise prediction is performed by assuming free-field propagation. In Fig. 5.24, the 2D simulations are obtained by using three different free-stream velocities; $U_{z/c=-\infty}$, $U_{z/c=-5.0}$ and $U_{z/c=-0.5}$. These are compared with the 3D simulation. As mentioned before, due to flow separation observed in the 2D case of $U_{z/c=-0.5}$, only the last three strips are considered for the prediction to determine if the high frequency range is closer to the 3D simulations as interpreted from the global boundary layer variables. The spectrum predictions obtained by the Kamruzzaman and Lee models show a difference of around 6 dB for the low frequencies which decreases for the middle frequencies and increases up to 2 dB for the higher frequencies, whereas the Panton & Linebarger model under-predicts compared to the other models. This is

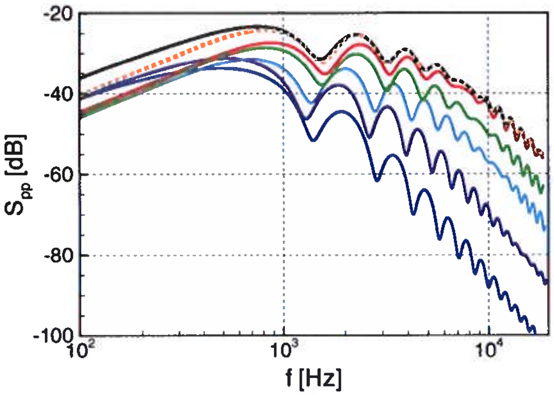

Figure 5.23: The far-field noise spectrum at $z = 10$ m contribution from different strip locations; *Strip 1* (—), *Strip 2* (—), *Strip 3* (—), *Strip 4* (—), *Strip 5* (—), contributions from all the strips (- - -), and contribution from the last three strips (*Strip 3*, *Strip 4* & *Strip 5*) (·····).

due to the fact that the kinetic energy profiles obtained from the 3D simulations are considerably lower. A better prediction is observed when the inlet velocity of $U_{z/c=-0.5}$ is used, however, a decrease in the low frequency is inevitable since the other strips locations which contribute mainly to the low frequency are neglected. For the far-field noise prediction upstream of the wind turbine, in general, the models perform well compared with the 3D predictions, except for $kc > 10$ for the Lee model where a decay is observed. However, when the inlet velocity of $U_{z/c=-0.5}$ is used, an increase for that frequency range is observed for the Kamruzzaman and the Lee models.

5.4. CONCLUSIONS

In this Chapter, a 3D RANS simulation is performed for the DonQi Urban Windmill to investigate the flow as well as the acoustic properties by performing the same analysis in the previous chapter. The rotational zone is simulated by a MRF methodology where the blade is assumed to be frozen and the flow passes through it, the Navier-Stokes equations are solved by considering the Coriolis and centrifugal effects. The mesh sensitivity is performed to demonstrate that the results are independent of the mesh resolution. This analysis holds true for the global parameters, however, as seen in Chapter 4, the boundary layer profiles are found to be sensitive to the mesh resolution.

As an alternative methodology, a 2D approach similar to the BEM methodology is suggested. In this methodology, the blade is considered alone by neglecting the effect of the nacelle and the diffuser. Assuming that the radial velocity component is negligible, the blade can be divided into isoradial strips. 2D incompressible steady RANS computations were performed for each strip location by unwrapping them. As a first step, the free-stream velocity is considered to be the same as in the 3D simulation, thus only the rotational component is added as $\omega_{rot} \cdot r_{strip}$, which depends on the radius of the each strip location and takes into account the rotational velocity. Later, a convergence study

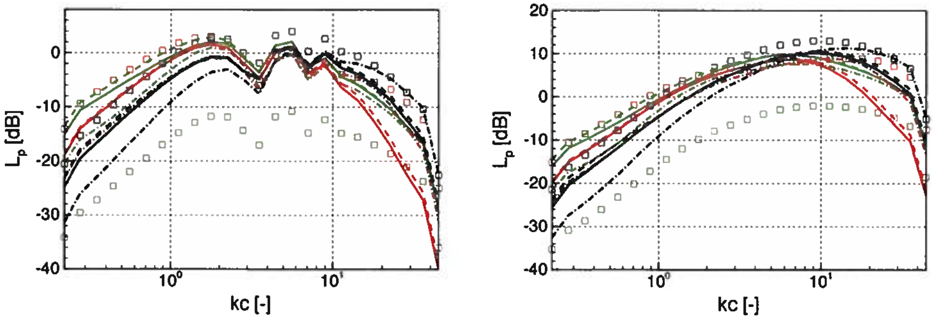

(a) L_p at z = 10 m downstream of the wind turbine.

(b) L_p at z = -10 m upstream of the wind turbine.

Figure 5.24: The 1/3 octave band far-field noise spectrum at two observer locations predicted by different wall-pressure spectra predicted by the Kamruzzaman model (black), the Lee model (red), and the Panton & Linebarger model (green) from $U_{z/c=-\infty}$ (solid line), $U_{z/c=-5.0}$ (dashed line), $U_{z/c=-0.5}$ (dashed-dotted line) and 3D simulation (rectangle).

based on the number of strips is carried out by diving the blade into 5, 10, and 20 strips. It is concluded that the 5 strips configuration is sufficient for Amiet's theory if the observer is located in the acoustical and geometrical far-field. As a second step, to take into account of the flow acceleration due to the nacelle and the diffuser, an axisymmetric RANS simulation is performed without the presence of the blade. Three additional axial positions rather than the free-stream ($z/c = -\infty$) are considered which are further upstream ($z/c = -5.0$), before the diffuser ($z/c = -0.5$) and before the blade ($z/c = 0.667$). The axial free-stream velocity values corresponding to these axial positions are imposed to 2D RANS simulations at each strip location.

The comparison between the 3D and 2D simulations are performed in terms of inlet velocity profiles upstream of the blade sections, pressure coefficient along the blade, and the boundary-layer profiles extracted at x/c = 0.99 normal to the blade surface at three strip locations. It has been observed that for the axial velocity a good comparison is achieved whereas for the azimuthal velocity, the peak point seems to be shifted which may indicate that the position of the blades are not identical. The radial mean velocity component from the 3D simulation shows that the order of magnitude with respect to the mean axial velocity is 10, which might have a weaker effect on the spanwise direction. The pressure distributions could not be reproduced by the 2D simulations even with different mean axial velocities at the hub region, which might be due to the centrifugal and Coriolis forces acting dominantly at that area resulting a difference between the 3D and 2D nature of the flow. For the middle part, a better match is observed with respect to the hub region, however, again the magnitude of the C_p distribution seems shifted down and increasing the velocity wouldn't help to imitate it. On the contrary, a better match is observed for the tip region for the inlet velocity of $z/c = -0.5$. Likewise, the C_p distribution was found to be shifted down in terms of magnitude which might create different flow field than the 2D simulations. Finally, the boundary-layer profiles extracted at $x/c = 0.99$

normal to the blade surface are investigated. In general, the boundary-layer profiles obtained form 2D simulation do not match with the 3D simulation. The last two velocities ($z/c = -0.5$ and $z/c = 0.667$) imposed to the 2D simulations demonstrate a separated flow for the hub region. Moreover, they could not reproduce similar results compared to the 3D simulation for the other strip locations, even though *Strip 5* gives better results in terms of the C_p distribution. When the global boundary layer variables are considered, it is found that the boundary-layer thickness and the wake parameters have a higher value than the 2D simulations whereas the integral variables are found to be of the same order.

The wall-pressure spectrum is predicted by three models; the Kamruzzaman, Lee, and Panton & Linebarger models for 2D and 3D simulations and the results are shown only for three strip locations investigated before. All of the 3D predictions at different strip locations performed by the Panton & Linebarger model show under-predicted results compared to the other models. For 2D simulations, increasing the velocity from $U_{z/c=-\infty}$ to $U_{z/c=-5.0}$ does not change the predictions significantly, as it does for the inlet velocity profiles. However, further increasing the velocity, the results perform better on the pressure side than the suction side. Overall, the Kamruzzaman model performs the best amongst the model compared to their prediction in 3D. The far-field noise predictions are performed at 10 m upstream and downstream of the blade. The 3D prediction of Panton & Linebarger model deviates significantly from the other predictions as it is also observed for the wall-pressure spectrum. The reason for it, may be due to the under-prediction of the turbulent kinetic energy. The 3D prediction of the other two models show a deviation of 6 dB maximum for the two locations. The 2D predictions from the Lee and Panton & Linebarger models exhibit a good match with the 3D simulations for the low frequency part while Kamruzzaman and Panton & Linebarger model perform better for the high frequency part. Moreover, the results obtained by the 2D simulation by imposing the velocity at $z/c = -5.0$ significantly improves the high frequency part for the Kamruzzaman and Lee models, whereas it seems negligible for the Panton & Linebarger model.

In terms of computational effort, the 3D simulations are performed on a node of a cluster built with AMD Opteron(tm) Processor, the computation took 1767 CPU-hour for the finest mesh while the 2D axisymmetric and 2D strip simulation for one strip location are performed on a work station with Intel(R) Xeon(R) CPU E5-2650 and the computation took 6.5 and 2.7 CPU-hour, respectively. In total, 2D approach for 5 strip locations with correction for the flow acceleration inside the nacelle uses 20 CPU-hour ($6.5+2.7\times5$) which is nearly two orders of magnitude times faster than 3D simulations.

In future work, the rotational velocity component for the 2D simulation can be varied to investigate flow field to reproduce the 3D simulations. Furthermore, the initial conditions could be obtained by a BEM method with the corrections for the 3D flow effects, and used to perform the 2D analysis.

Table 5.4: Global variables at $x/c = 0.99$ for different strip locations

Simulation	Side	Strip number	δ/c	U_e/U_{Rel}	u_τ/U_{Rel}^2	δ^*/c	θ/c	Π	β
3D	Suction	*Strip 1*	0.119	1.143	0.004	0.017	0.010	3.353	6.257
		Strip 2	0.113	1.046	0.002	0.014	0.009	4.394	9.190
		Strip 3	0.095	1.017	0.002	0.011	0.007	3.700	7.205
		Strip 4	0.081	1.005	0.001	0.009	0.006	3.109	5.611
		Strip 5	0.078	0.998	0.001	0.009	0.005	2.801	4.817
	Pressure	*Strip 1*	0.038	1.092	0.008	0.004	0.002	0.440	-0.049
		Strip 2	0.037	0.999	0.004	0.004	0.002	0.459	-0.024
		Strip 3	0.040	0.984	0.003	0.004	0.002	0.432	0.005
		Strip 4	0.047	0.979	0.002	0.004	0.003	0.614	0.203
		Strip 5	0.046	0.978	0.002	0.004	0.003	0.746	0.411
$U_{z/c=-\infty}$	Suction	*Strip 1*	0.045	1.040	0.004	0.015	0.007	2.0522	3.0116
		Strip 2	0.038	1.000	0.002	0.013	0.006	3.0698	5.5076
		Strip 3	0.033	0.977	0.001	0.010	0.005	1.4416	1.6928
		Strip 4	0.028	0.959	0.001	0.008	0.004	1.0763	0.9852
		Strip 5	0.026	0.953	0.001	0.007	0.004	1.0192	0.881
	Pressure	*Strip 1*	0.020	1.043	0.007	0.005	0.003	0.4695	-0.0087
		Strip 2	0.018	0.990	0.004	0.004	0.002	0.4983	0.032
		Strip 3	0.019	0.966	0.003	0.004	0.003	0.0956	-0.4412
		Strip 4	0.024	0.957	0.002	0.006	0.003	0.3586	-0.1569
		Strip 5	0.025	0.954	0.001	0.006	0.003	0.4198	-0.0768
$U_{z/c=-5.0}$	Suction	*Strip 1*	0.053	1.117	0.004	0.019	0.008	2.9334	5.1543
		Strip 2	0.046	1.037	0.002	0.018	0.007	4.6689	10.0076
		Strip 3	0.037	0.995	0.001	0.012	0.006	1.6125	2.0461
		Strip 4	0.028	0.967	0.001	0.009	0.004	1.1291	1.0831
		Strip 5	0.026	0.956	0.001	0.007	0.004	1.0466	0.9308
	Pressure	*Strip 1*	0.018	1.117	0.008	0.005	0.002	0.322	-0.2026
		Strip 2	0.016	1.025	0.004	0.004	0.002	0.3451	-0.1741
		Strip 3	0.018	0.983	0.003	0.004	0.002	0.116	-0.4238
		Strip 4	0.022	0.963	0.002	0.005	0.003	0.3453	-0.1738
		Strip 5	0.024	0.956	0.001	0.006	0.003	0.4182	-0.0789
$U_{z/c=-0.5}$	Suction	*Strip 1*	-	-	-	-	-	-	-
		Strip 2	0.150	0.831	-	0.108	0.013	-	-9.3629
		Strip 3	0.056	1.061	0.001	0.023	0.009	0.3904	-0.1158
		Strip 4	0.037	1.003	0.001	0.012	0.006	1.3222	1.454
		Strip 5	0.030	0.982	0.001	0.009	0.005	1.2606	1.3337
	Pressure	*Strip 1*	0.013	1.367	0.013	0.002	0.001	0.4011	-0.1017
		Strip 2	0.013	1.201	0.006	0.002	0.001	-	-0.6452
		Strip 3	0.015	1.040	0.003	0.003	0.002	0.1065	-0.4321
		Strip 4	0.017	0.990	0.002	0.004	0.002	0.2526	-0.285
		Strip 5	0.019	0.970	0.002	0.004	0.003	0.3532	-0.1638

II

EXPERIMENTAL WORK

6

A REMOTE MICROPHONE TECHNIQUE FOR AEROACOUSTIC MEASUREMENTS IN LARGE WIND TUNNELS

The present study was devoted to the development and application of a remote microphone technique for aeroacoustic measurements in large aerodynamic wind tunnels. In this technique, the microphone and its connecting line to the sensing port are fitted within an aerodynamically streamlined fairing. A model-based calibration method was applied to account for the phase lag and dissipation within the microphone connecting line. The proposed system allows acoustic measurements when the wind tunnel surface cannot be altered, since the fairing can simply be glued on the wall. The fairing is streamlined to minimize flow disturbances as well as the risk of separation which would otherwise contaminate the wind tunnel flow quality and acoustic measurements. It was furthermore hoped that the acceleration of the flow over the fairing surface might reduce the turbulence fluctuations and thereby increase the signal-to-noise ratio of the acoustic measurements. Those aerodynamic effects were investigated with a set of hot-wire measurements performed in the subsonic L2B small wind tunnel of the von Karman Institute (VKI). The mean velocity and the turbulence intensity profile were analyzed in the presence of different inflow turbulence characteristics at 5, 10, and 15 m/s free-stream velocity. The effect of incident turbulence on the acoustic measurement was investigated by applying the calibration procedure and comparing the measurements with a wall-mounted reference microphone signal in similar flow conditions. As an application, this technique is used to measure the noise emitted from the contra-rotating fans of the large L1 subsonic wind tunnel of the von Karman Institute, where the microphone fairing is placed inside the diffuser and thus subjected to a thick turbulent boundary layer.

6.1. INTRODUCTION

The reduction of flow-generated noise has become one of the demanding design criteria for numerous engineering applications. Consequently, a growth of interest has emerged in the field of experimental aeroacoustics, in order to better understand aerodynamic sound production mechanisms and to validate noise prediction methods.

Large aerodynamic wind tunnels have been and are currently being refurbished to permit measuring the noise emissions of wing components, landing gears, wind turbine blade sections, etc., at realistic Reynolds numbers Moreau et al. [132]. In this context the von Karman Institute for Fluid Dynamics (VKI) is investigating the possibility of using its largest subsonic wind tunnel L1 as a mean to study contra-rotating rotor (CRR) noise. In this instance, the CRR under consideration is the twin-rotor fan that provides the flow to the wind tunnel. In order to measure the tonal and broadband noise resulting from the viscous wake interactions, an array of wall-mounted microphones has been designed, to be located in the divergent section of the wind tunnel (Fig. 6.1).

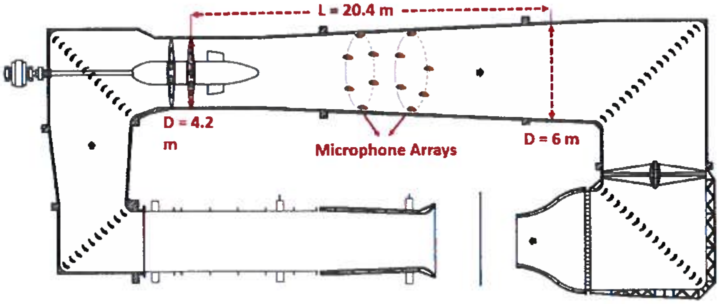

Figure 6.1: The L1 wind tunnel.

The following guidelines drove the design:

1. The number and spatial distribution of microphones should permit extracting the acoustic field in terms of its duct modal components, up to the second azimuthal mode.
2. The placement of the microphones should not require drilling into the thick (about 0.3 m) concrete walls of the divergent section. As a result, the microphones should be encapsulated within fairings, to be glued on the inner wall of the divergent section.
3. The microphones fairings should not introduce additional turbulence, for the sake of flow quality in the test section firstly, and secondly to avoid extraneous noise generation by the guide vanes at the downstream end of the divergent section.
4. If possible, the fairings should enhance the signal-to-noise ratio between the incident acoustic field and the hydrodynamic pressure fluctuations induced by the turbulent boundary layer (TBL) at the microphone locations.

While the first aspect above won't be treated in this paper – it is discussed in length in the literature, e.g. by Sack et al. [160], the other objectives and proposed solutions are detailed in what follows.

The structure of the chapter is the following: Section 6.2 describes the technical solution adopted to meet the above objectives, which implies a modelling of the acoustic response of the system (Section 6.3) and evaluating the influence of TBL pressure fluctuations on the measurement accuracy (Section 6.4). Conclusions are drawn in Section 6.5.

6.2. MICROPHONE FAIRING

In order to minimize flow separation, which would otherwise alter the wind tunnel flow quality and contaminate the microphone signal, the fairing encapsulating the microphone was designed using a streamlined profile, shown in Fig. 6.2(a). It is a combination of two arcs in which the trailing edge radius, 0.2 m, is twice the leading edge radius. The fairing has 0.224 m length, maximum height of 0.047 m and maximum width of 0.12 m. This shape is not the result of an aerodynamic optimization, but follows empirical guidelines to mitigate the risk of flow separation with a size compatible with the curvature of the wind tunnel wall. The microphone is lying horizontal to minimize blockage, and its holding part was designed in a modular way, such that it can be disassembled from the fairing and fitted on a calibrator shown in Fig. 6.2(b). The aim here is to permit a calibration as close to *in-situ* conditions as possible, accounting for the acoustic response of the channel and cavity that lead from the pressure port to the microphone membrane. The dimensioning of the line-cavity system was performed by means of a linear response model detailed in Section 6.3, together with its experimental validation.

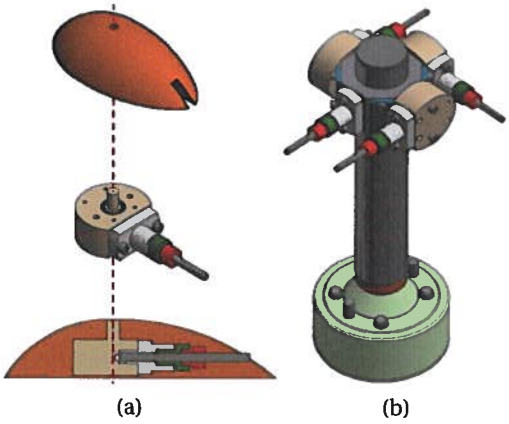

(a) (b)

Figure 6.2: CAD drawing of (a) the fairing, the holding part with the microphone and the assembly, (b) the calibrator with the holding parts and a reference microphone.

Another purpose of the design, justifying the position of the pressure tap on the fairing top, is to take advantage of the local acceleration that occurs from the leading edge of the fairing. This is an attempt to reduce the turbulent fluctuations and improve the relative importance of the acoustic signal. Section 6.4 details the hot wire measurements that were conducted over the fairing in order to quantify the effect of the acceleration on the turbulence intensity, and to correlate this effect to the quality of the acoustic measurements.

6.3. LINE-CAVITY RESPONSE MODEL

The microphone is connected to the pressure port via an L-shaped line and cone shaped cavity system as shown in Fig. 6.3(a). The length and diameter of the line, as well as the cavity volume, have an important effect on the amplitude and phase lag of the pressure fluctuations sensed by the microphone membrane. Since the frequency response of the line-cavity system can exhibit strong resonances that are detrimental to the measurement accuracy, several methods can be employed to damp out the resonance. A possibility is to use a small diameter flexible tube. However, this can introduce a signal distortion. Another method is to insert dampers to suppress the resonance in the system as described in Surry and Stathopoulos [179]. Eventually, the most promising solution was found to consist in correcting the signal based on the measured transfer function of the system. A correction of the amplitude is sufficient when single sensor measurements are to be processed, but in our case a phase calibration is also needed since the duct modal eduction makes use of the phase between different microphones. An example of a digital correction technique using the inverse transfer function was introduced by Irwin et al. [105]. This strategy will be followed in this paper, using the measured transfer function [14, 147].

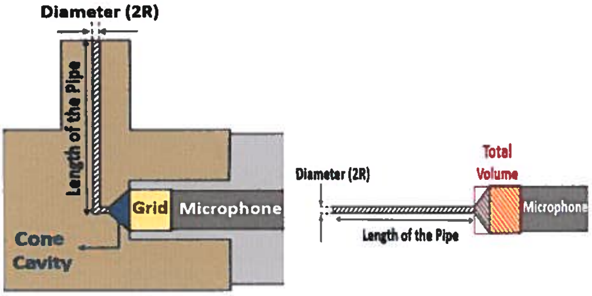

(a) (b)

Figure 6.3: (a) Microphone holding part, inserted in the fairing as shown in Fig. 6.2(a); (b) its simplification as a line-cavity system.

The analytical models that simulate the dynamic response of the tube are investigated by Bergh and Tijdeman [21] and citetstinson amongst others [10, 84, 196]. These models account for compressibility effects, viscous dissipation, heat loss, and elastic expansion [100]. In this paper, the remote microphone technique will be compared with the Bergh and Tijdeman [21] model. The model is expressed as a linear time-invariant system subjected to small amplitude perturbations.

The transfer function between the pressure at the port opening and the pressure sensed by the pressure sensor is given by Bergh and Tijdeman [21]:

$$\frac{\hat{p}_1}{\hat{p}_0} = \left[cosh(\phi L) + \frac{V_v}{V_t}\left(\sigma + \frac{1}{k}\right) n\phi L sinh(\phi L)\right]^{-1} \tag{6.1}$$

where $\phi = \frac{v}{a_0}\sqrt{\frac{J_0<\alpha>}{J_2<\alpha>}}\sqrt{\frac{\gamma}{n}}$ with $\alpha = i^{3/2}R\sqrt{\frac{\rho_s v}{\mu}}$ is the shear wave number where the viscosity is taken into account, i is the imaginary unit, R is the tube radius, ρ_s is the mean density, v is the frequency, μ is the absolute fluid viscosity, $n = \left[1 + \frac{(\gamma-1)}{\gamma}\sqrt{\frac{J_2<\alpha\sqrt{Pr}>}{J_0<\alpha\sqrt{Pr}>}}\right]^{-1}$ is a polytropic constant, $Pr = \frac{\mu C_p}{\lambda}$ is the Prandtl number, $\gamma = C_p/C_v$ is the specific heat ratio, J_m is the Bessel function of first kind of order m, a_0 is the mean velocity of the sound, L is the length of the pipe, V_v and V_t are the pressure transducer and tube volume, σ is the dimensionless increase in transducer volume due to diaphragm deflection, and k is the polytropic constant for the volumes [21]. This model was implemented in a VKI in-house MATLAB code named PreMeSys [33].

The three geometrical parameters which affect the frequency response function are the line radius, length, and the cavity volume. Their influence has been quantitatively validated using the results of Bergh and Tijdeman [21]. Since the amplitude and frequency of the resonance are most sensitive to the line radius and the line length, these variables represent the most effective design parameters. In contrast, changing the cavity volume within the limits of practicality does not affect significantly the resonance frequency. A high resonance frequency of the system would be achieved with small line length and cavity volume, and a large line radius. However, a large diameter increases the probing area, leading to a degradation of the spatial resolution and allowing turbulence to contaminate the microphone measurements.

Their influence is investigated in Fig. 6.4. The results permit validating the PreMeSys code. They also indicate that

- increasing the line radius has the effect of increasing the resonance frequency, as well as its amplitude as a result of lower viscous losses;
- increasing the line length increases the propagation time and adds viscous losses, such that both resonance amplitude and frequency decrease;
- increasing the volume adds a buffer for the acoustic propagation in the system, leading as well to a reduction of the resonance amplitude and frequency.

6.3.1. DESIGN OF THE FAIRINGS

The pipe length and radius, as well as the cavity volume, were designed to avoid a potential flow and acoustic coupling as observed by Tonon et al. [188]. In such a feedback mechanism, the vortex shedding at the port aperture couples with the acoustic response of the branch at the closed end. The vortex shedding at the port aperture was characterized by a Strouhal number $St = 2fR/U_0$ observed around 0.4, where U_0 is the velocity above the aperture. A small pipe radius R is desirable for the sake of spatial resolution,

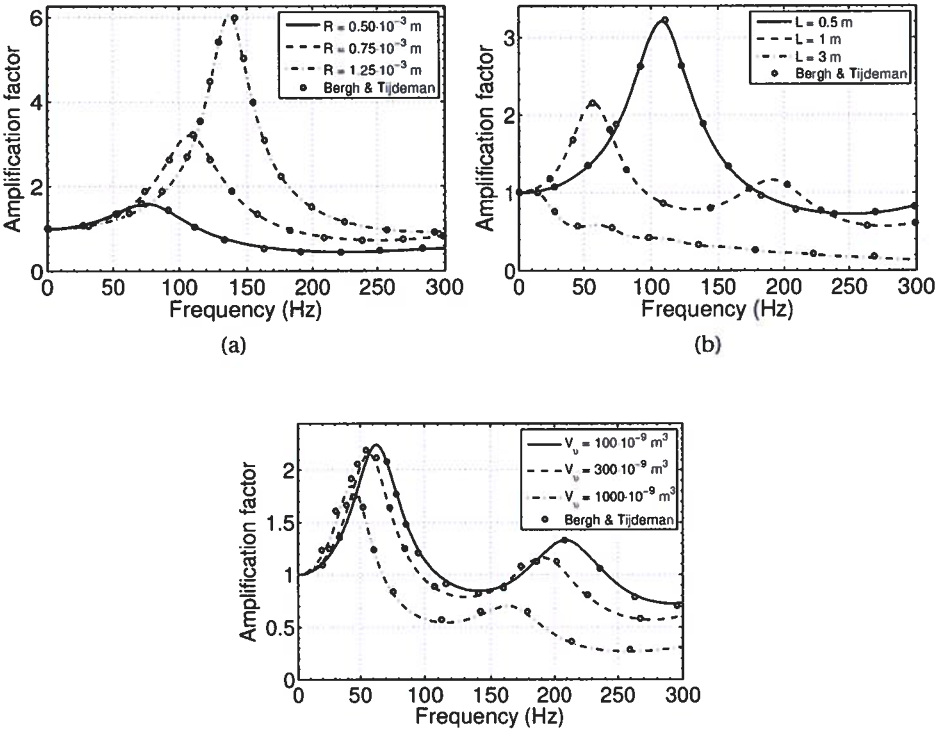

(a)

(b)

(c)

Figure 6.4: Validation of PreMeSys by comparison with results of Bergh and Tijdeman [21] and effect of geometrical parameters. (a) effect of pipe radius ($L = 0.5\,\mathrm{m}$, $V_v = 300 \cdot 10^{-9}\,\mathrm{m}^3$); (b) effect of pipe length ($R = 0.75 \cdot 10^{-3}\,\mathrm{m}$, $V_v = 300 \cdot 10^{-9}\,\mathrm{m}^3$); (c) effect of cavity volume ($L = 1\,\mathrm{m}$, $R = 0.75 \cdot 10^{-3}\,\mathrm{m}$). $\sigma = 0$ and $k = 1.4$.

with the smallest radius that can be drilled with precision being $0.5\cdot10^{-3}$ m. Three pipe-cavity systems with a radius size of $0.5\cdot10^{-3}$, $1.0\cdot10^{-3}$, and $1.5\cdot10^{-3}$ m were calculated with PreMeSys to obtain the acoustic resonance frequency. The equivalent line-cavity model is illustrated in Fig. 6.3(b), where the total volume of the equivalent cavity includes the volume between the protection grid and the membrane. The geometrical parameters were calculated from the CAD model as indicated in Table 6.1. The results obtained with PreMeSys are shown in Fig. 6.5.

$Radius\cdot10^{-3}$ (m)	$Length\cdot10^{-3}$ (m)	$Volume\cdot10^{-9}$ (m^3)
0.5	30.4	304
1.0	30.9	304
1.5	31.4	299

Table 6.1: Parameters for the pipe-cavity systems of Fig. 6.3.

For the targeted application presented in Section 6.4.3, the grazing flow velocity U_0 is of the order of 10 m/s. The frequencies corresponding to $St = 0.4$ are $f_{St} = 4$ kHz, 2 kHz and 1.3 kHz for radii of $0.5\cdot10^{-3}$ m, $1.0\cdot10^{-3}$ m, and $1.5\cdot10^{-3}$ m, respectively. From Fig. 6.5, it can be observed that the acoustic resonance frequencies of the pipe-cavity systems for $R = 0.5\cdot10^{-3}$ m and $1.0\cdot10^{-3}$ m are well below those values, which should thus not lead to spurious flow-acoustic resonances. A pipe radius of 1 mm was finally selected as it provides a nearly constant gain for the frequency range of interest for the application described in Section 6.4.3, which is [0, 500] Hz.

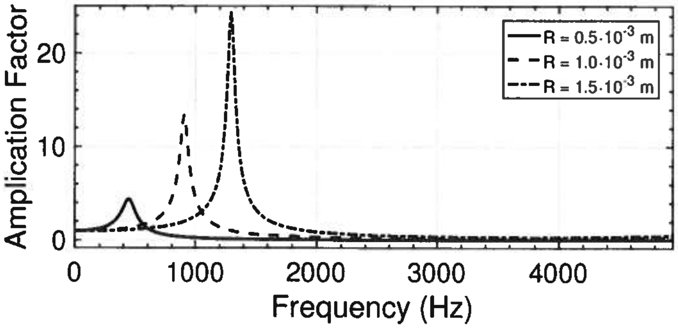

Figure 6.5: Investigation of the parameters in Table 6.1 with PreMeSys.

6.3.2. CALIBRATION PROCEDURE

The static calibration was performed by using the B&K Sound Calibrator Type 4231. The calibrator emits a continuous signal at 1 kHz with a sound pressure level of 94 dB. The dynamic calibration was performed with the calibrator shown in Fig. 6.2(b). A loudspeaker was placed on one side of the calibration tube and, on the other side, the microphones were distributed equally at the same axial position.

The data acquisition was performed by National Instrument cDAQ-9178 with two modules: NI 9215 for the microphones and NI 9263 for the loudspeaker. *B&K* 4938A-

011-1/4-inch pressure-field microphones with Type 2670 preamplifier were connected to the *B&K* Nexus conditioning amplifier Type 2960-A. The microphones were exposed to a chirp signal, where the frequency range starts from the lowest frequency emitted from the loudspeaker ($f_{min} \approx 100$ Hz) up to the cut-off frequency of the pipe ($f_{max} \approx 5$ kHz). The sampling rate was chosen as 51.2 kHz with 2^{20} samples. A reference microphone was flush-mounted to determine the response of the pipe-cavity system for the three different configurations. The measured transfer function is defined as [30, 96]:

$$H(f) = \frac{S_{21}(f)}{S_{11}(f)} \tag{6.2}$$

where 1 denotes the reference microphone and 2 is the pipe-cavity system, S_{21} is the cross power spectral density of the reference microphone and the pipe-cavity system and S_{11} is the power spectral density of the reference microphone. The transfer function is calculated by *tfestimate* MATLAB code, which uses Welch's averaged, modified periodogram method. The signals are divided by 2^{16} segments with 50% overlap by applying Hanning window. Afterward, the periodogram of each segment is calculated and the spectral densities are averaged.

The pipe-cavity system was machined out of a block of Teflon. Three designs with three different pipe radii have been tested using the calibrator to obtain the transfer function. The results are shown in Fig. 6.6 for the largest of the three radii, $R = 1.5 \times 10^{-3}$ m, and for 8 different realizations of the same design. The results indicate that both for the magnitude and phase, significant discrepancies are observed between the measured transfer function and the theoretical model, and even between different realizations, in spite of similar manufacturing qualities. In terms of amplitude, the measured values are significantly below the prediction, which we conjecture can be due to the mechanical compliance and roughness of the material. This was also observed by Hurst and Van De Weert [100], who also used Teflon.

6.4. AERODYNAMIC EFFECTS OF THE FAIRING ON THE ACOUSTIC MEASUREMENTS

Hot-wire measurements and acoustic measurements have been performed with and without the fairing in the L2B wind tunnel of VKI to assess the effect that the fairing has on the grazing flow at the sensing port. L2B is an open circuit wind tunnel of suction type with a 4.4 kW variable-speed DC motor providing a maximum velocity of 35 m/s. The rectangular test section, shown in Fig. 6.7, is $H = 0.35$ m high, 0.35 m wide, and 2 m long. The fairing, with maximum height at the sensing port equal to $0.13H$, was placed at a distance $3.86H$ downstream of the inlet. The boundary layer measurements were obtained at a single axial position above the sensing port of the pipe-cavity system. A reference microphone was placed at the same axial and spanwise location, but flush-mounted on the opposite wall. A Prandtl tube was used to measure the free-stream velocity at channel mid-height. The hot-wire and acoustic measurements were performed with a sampling frequency of 51.2 kHz with 2^{20} samples.

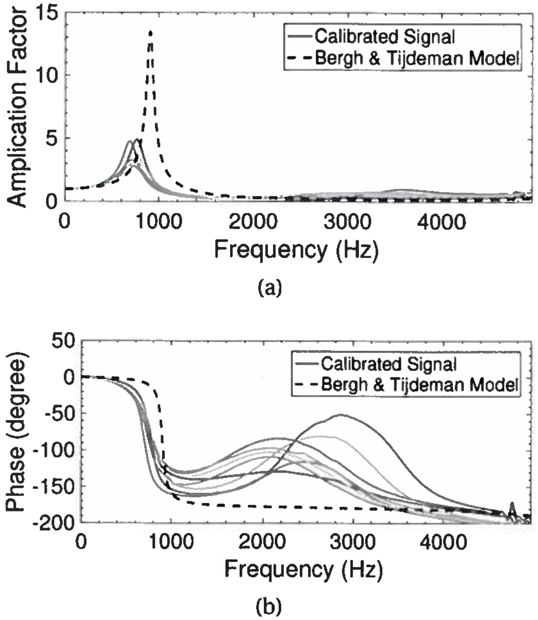

(a)

(b)

Figure 6.6: Comparison of the experimental calibration with the PreMeSys prediction. (a) amplitude of the dynamic response; (b) phase of the dynamic response.

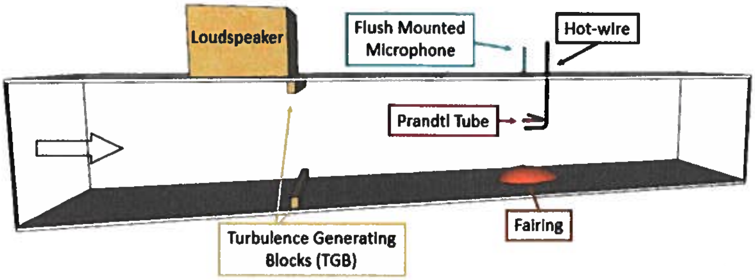

Figure 6.7: L2B wind tunnel setup.

6.4.1. AERODYNAMICS

The mean velocity profile and the turbulence intensity are shown in Fig. 6.8, for three different velocities: 5, 10, and 15 m/s. Here, y is the distance from the surface of the wind tunnel lower wall, or from the surface of the fairing when the latter is in place. U_{ref} is the reference velocity measured at channel mid-height, used for the calculation of the turbulence intensity $T.I. = \sqrt{\overline{u'^2}}/U_{\mathrm{ref}}$. In the presence of the fairing and for a canonical flat plate incoming turbulent boundary layer, Fig. 6.8 (up) shows that the velocity accelerates and causes a reduction of the turbulence intensity over most of the boundary layer height, except close to the surface where the turbulence intensity remains mostly unaffected.

A second measurement campaign was conducted, to evaluate the effect of the fairing subjected this time to a highly turbulent boundary layer, produced by turbulence-generating blocks (TGBs). Rectangular cross-section blocks extending over the full channel span perpendicularly to the mean flow, with streamwise dimension 0.057 H and height 0.086 H, were placed at 2.14 H upstream of the fairing leading edge (see Fig. 6.7), on the bottom and upper walls of the wind tunnel. A longitudinal separation between the TGB and the microphones around 25 block heights ensures that the microphones are well beyond the reattachment of the block-induced separation bubble, even if the redeveloping turbulent boundary layer has probably not reached equilibrium yet when reaching the microphones. This is not considered an issue, the purpose of this study being mostly to obtain a thicker and more turbulent boundary layer at the location of the sensing port.

The same reference velocity as before, $U_{\mathrm{ref}} = 5, 10$ and $15\,\mathrm{m/s}$, was maintained at channel mid-height. The mean velocity and turbulence intensity profiles, obtained with the TGBs in place, are shown in Fig. 6.8 (bottom). The boundary layer thickness appears to be substantially larger than in the clean case, as desired. In this high turbulence case, while the acceleration of the mean flow induced by the fairing is still significant, the benefits in terms of turbulence reduction are mitigated: reduction is only observed for $y/H > 0.06$ while a substantial increase of the turbulence is found closer to the sensing port, with turbulence levels in excess of 20% to be compared with the 13-14% that was measured in absence of fairing. This is anticipated to be detrimental for the acoustic measurement accuracy.

6.4.2. ACOUSTIC MEASUREMENTS

Two measurement campaigns were conducted. In the first one, a lousdpeaker is used, and fed with a low-frequency signal in order to generate a plane wave at the axial location of the L2B duct where two microphones are located (see Fig. 6.7). In the second one, no loudspeaker is used and the background noise of the L2B wind tunnel is measured.

First acoustic measurement campaign: using a loudspeaker source

The acoustic pressure spectra below are expressed as Sound Pressure Levels (SPL) using the conventional reference pressure of 20 μPa. The power spectra were computed by *pwelch* MATLAB code and the required parameters were chosen to be the same as in the calibration procedure. For the first acoustic measurement campaign, a chirp signal spanning from 10 Hz to 500 Hz was used, the first transversal cut-off frequency of the duct corresponding to $kH = \pi$ being 485 Hz [95]. The reference microphone being flush-mounted, it is directly exposed to the incident acoustic field and incoming turbulent pressure fluctuations. The second microphone is installed in the aerodynamic fairing, with its sensing port at the same axial location, and should therefore sample the same acoustic signal in both amplitude and phase. From the results of Section 6.4.1, one might however expect different pressure measurements owing to the different evolutions of the boundary layers sensed by the reference and fairing microphone. It was therefore

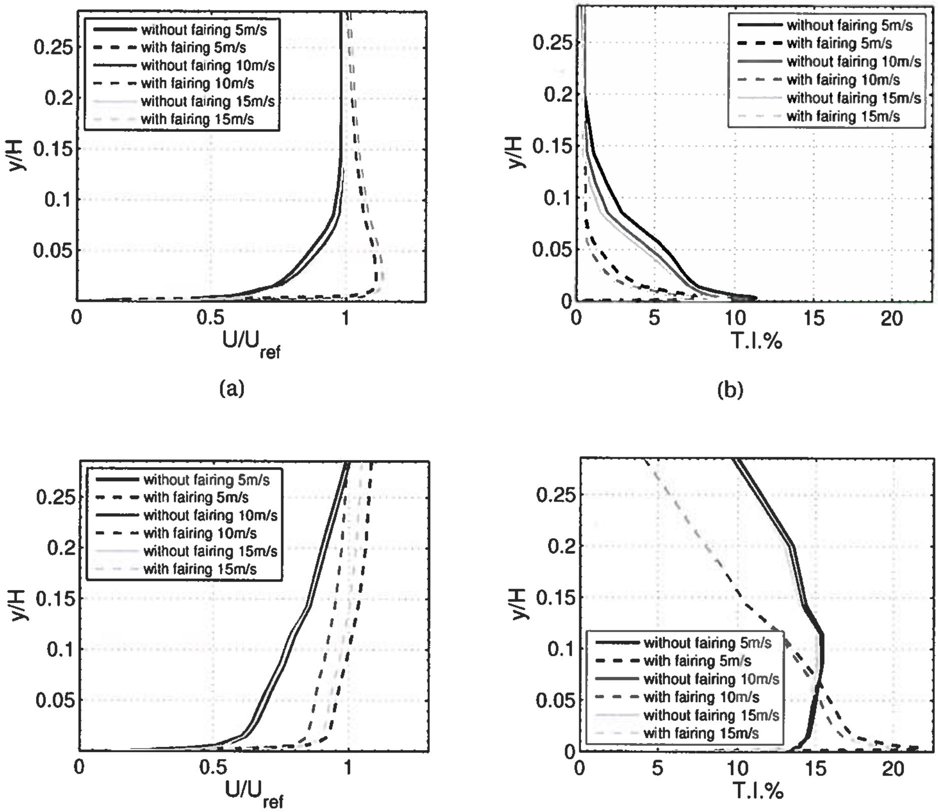

(a) (b)

(c) (d)

Figure 6.8: Mean velocity profiles (left) and turbulence intensity profiles (right), with a clean incoming boundary layer (up) and in presence of upstream turbulence-generating blocks (down), for free-stream velocities $U_{\text{ref}} = 5, 10$ and $15\,\text{m/s}$.

verified *a priori* that the amplitude of the loudspeaker excitation is sufficiently above the background noise of the L2B facility. The results shown in Fig. 6.9 indicate that this condition is fulfilled at 10 m/s, for which the loudspeaker level is at least 10 dB above the background noise of the facility. This is true except for frequencies below 60 Hz, where the wind tunnel longitudinal resonances dominate, and at the Blade Passing Frequency of the axial fan (121 Hz and 176 Hz for 10 m/s and 15 m/s, respectively) and its higher harmonics. For U_∞ = 15 m/s, the background noise cannot be considered as negligible over a large range of frequencies. Thus, the following results focus on the 10 m/s case accordingly.

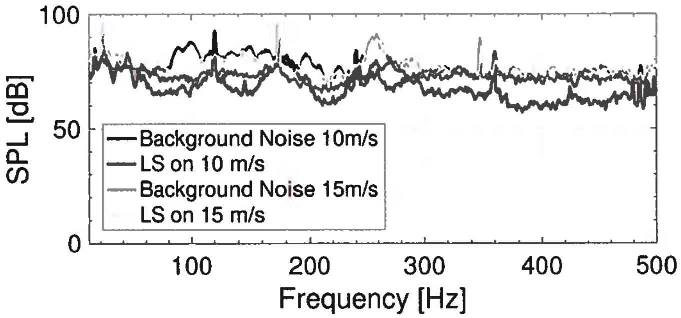

Figure 6.9: Amplitude of the loudspeaker excitation compared with the L2B background noise for U_∞ = 10 m/s and 15 m/s.

The transfer function obtained from the calibration procedure is applied in the Fourier domain to the signal received from the fairing to calibrate the signal:

$$R(f) = \frac{M(f)}{H(f)} \tag{6.3}$$

where M is the raw signal received from the fairing, H is the transfer function given in Eq. (6.2) and R is the calibrated signal. Fig. 6.10 permits comparing the wall pressure signal, the raw signal and the calibrated signal at 10 m/s. The effect of the correction is relatively minor over most of the frequency range (consistently with Fig. 6.6), but reaches a non-negligible difference of 5 dB at 460 Hz, where it still permits an acceptable compensation. Above 460 Hz (kH = 2.98), the appearance of slowly decaying cut-off transverse modes can probably explain the discrepancy between the acoustic fields measured at the upper and lower plates, the loudspeaker being mounted on the upper wall at only $2H$ of longitudinal distance upstream of the microphones section.

With regard to the phase compensation, Fig. 6.11 shows the phase between the wall pressure signal and fairing microphones (theoretically zero for the plane wave mode), without and with compensation applied to the latter. Consistently with the phase calibration shown in Fig. 6.6, it can be seen that the phase compensation is relatively minor in this frequency range, but still brings an improvement with respect to the raw signal.

Second acoustic measurement campaign: measuring facility background noise

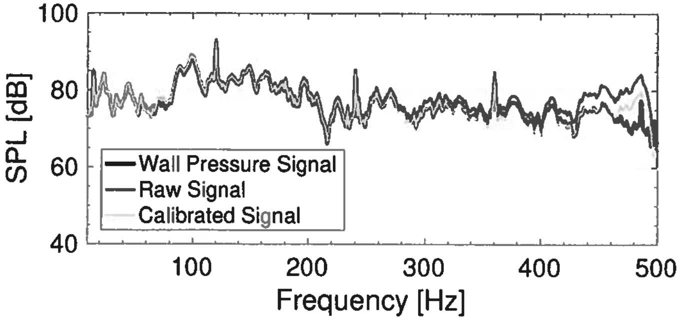

Figure 6.10: Comparison of the wall pressure signal, the raw signal, and calibrated signal, $U_\infty = 10\,\text{m/s}$.

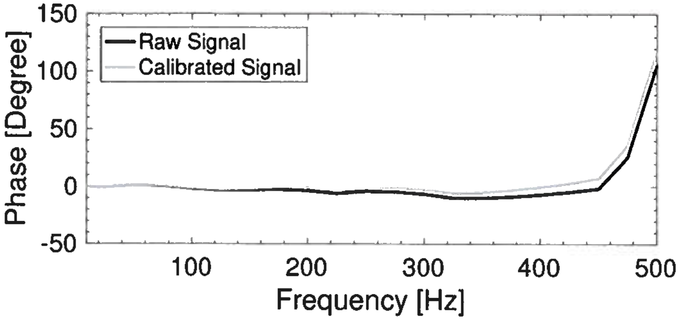

Figure 6.11: Phase difference between the wall pressure signal and fairing microphones, without and with phase compensation for the latter.

The objective of the second acoustic measurement campaign is twofold: *i)* to assess the effect of the compensation for a wider frequency range including the resonance of the pipe-cavity system (observed to lie around 700 Hz in Fig. 6.6), and *ii)* to quantify the impact of the alteration of the turbulent flow by the fairing, observed in Section 6.4.1, on the measured pressure fluctuation. For those measurements, the loudspeaker is not used, and the background noise produced by the L2B facility serves as test signal.

The considered frequency range extends up to 5 kHz. Note that the pressure spectra shown below, including non-negligible turbulent pressure components for some frequencies, are still expressed in terms of Sound Pressure Levels with a reference pressure of 20 μPa. It was verified as a preliminary step that the extended pressure spectra are similar on both lower and upper walls of the test section when measured with flush-mounted microphones. Figure 6.12 confirms this assumption, permitting in what follows the comparison of flush-mounted microphone measurements at the upper wall with fairing microphone measurements at the lower wall under identical flow conditions. Similar conclusions were reached for a free-stream velocity of 15 m/s, and also in presence of the turbulence-generating blocks.

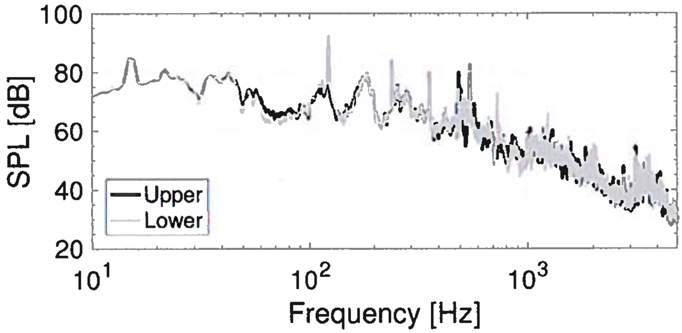

Figure 6.12: Wall pressure spectra measured at the upper and lower walls of the L2B test section using flush-mounted microphones.

The case without TGB is discussed first. The effectiveness of compensating the fairing microphone measurements using the measured calibration function is quite obvious in Fig. 6.13, especially in the range [600-900] Hz where it removes the resonance of the pipe-cavity system, and above 1 kHz where it corrects for the attenuation in the line. Concerning the alteration of turbulence due to the fairing, comparing the calibrated signal and flush-mounted microphones measurements does not allow to discern any substantial difference in spite of the strong acceleration of the flow and substantial reduction of the turbulence intensity (at least far enough from the wall) that were observed in Fig. 6.8 (top). This can be an indication that the measured pressure fluctuations are mostly radiated by the facility and of acoustic nature, and/or that the local wall pressure fluctuations are mostly induced by the near-wall turbulence, which was indeed observed to not vary significantly in Fig. 6.8 (top-right).

Since comparing the spectra at 10 m/s and 15 m/s doesn't allow to elucidate the acoustic vs. turbulent nature of the measured pressure fluctuations, the attention is now turned to the measurements performed with the TGBs, forcing larger incoming turbu-

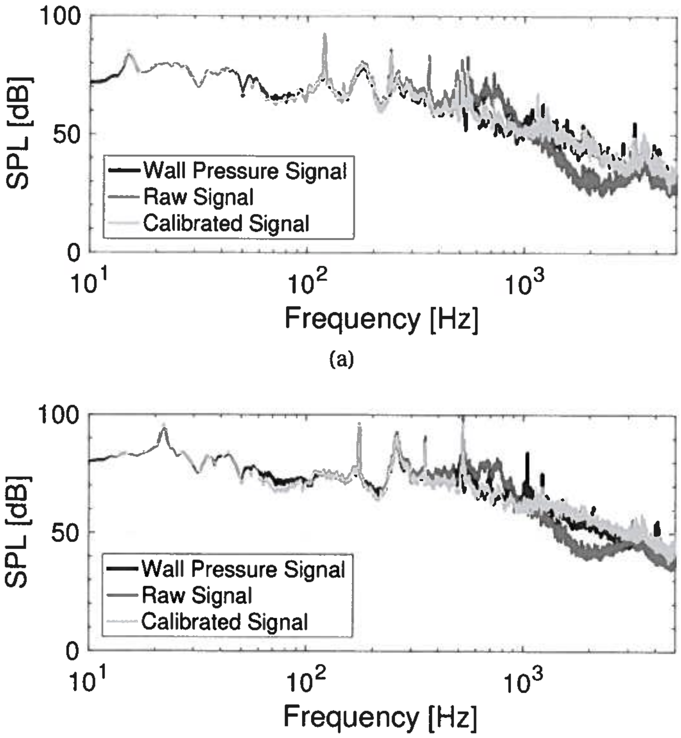

(a)

(b)

Figure 6.13: Effect of the fairing microphone compensation on the measured pressure spectrum for U_∞ = 10 m/s (a) and 15 m/s (b). Clean incoming boundary layer.

lence intensities. The effect of the TGB is quantified by the flush microphone spectra shown in Fig. 6.14, where the frequency axis has been rescaled by the Blade Passing Frequency (BPF) to facilitate comparison, since the fan speed had to be slightly adjusted to maintain the free-stream velocity in presence of the TGBs. The effect of the increased turbulence is mostly visible below the first BPF, where the levels are increased by about 5 to 10 dB depending on the flow speed, compared with the clean TBL case. At higher frequencies the spectrum seems to be dominated by the background acoustic noise of the facility, both in terms of tonal and broadband content.

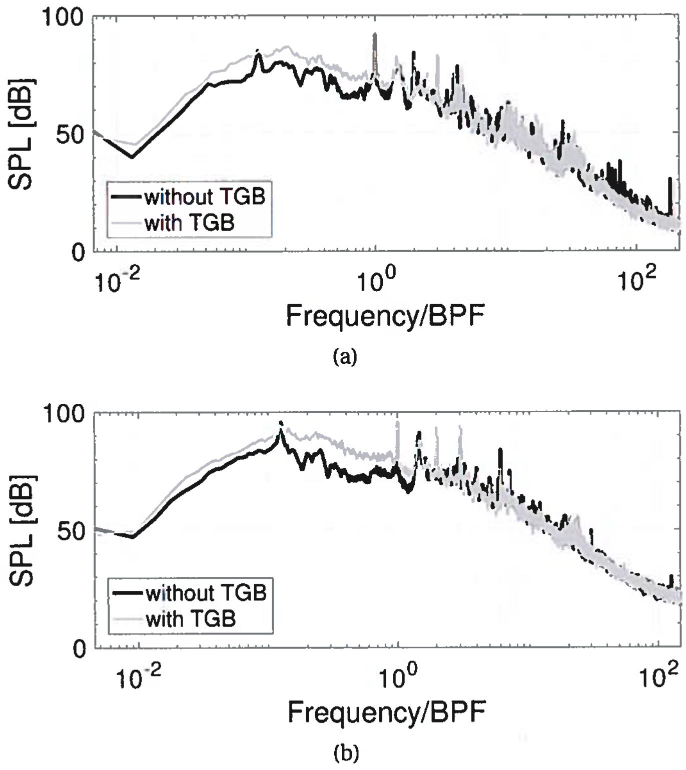

Figure 6.14: Effect of the turbulence-generating blocks on the spectra measured by the flush-mounted microphone for U_∞ = 10 m/s (a) and 15 m/s (b).

In contrast, the acoustic spectra measured by the fairing microphone (Fig. 6.15) exhibit shape and levels that indicate a more intense contribution of the turbulent pressure fluctuations for the fairing microphone than for the flush-mounted one. The increased turbulence pressure levels range from 3-5 dB at low frequencies below the BPF, to reach about 10 dB above 1 kHz at 15 m/s. This result is consistent with the substantial increase of the turbulence intensity close to the fairing surface that was reported in Fig. 6.8 (bottom-right) from the hot wire measurements. This investigation doesn't permit to resolve whether the increase of the measured turbulence pressure levels is predominantly caused by the flow acceleration over the fairing, or due to the sensing location being deported upwards itself, or a combination of both effects. But it can be noted that in the present case the fairing height of $0.13H$, coincidentally, brings the sensing port location roughly at the height where the maximum T.I. was measured in absence of the fairing (Fig. 6.8). Irrespectively of these effects, Fig. 6.15 demonstrates again the efficiency of the signal compensation to remove the effects of line-cavity resonance and dissipation.

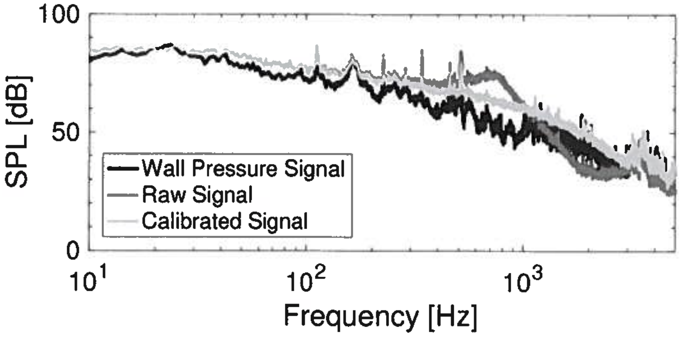

(a)

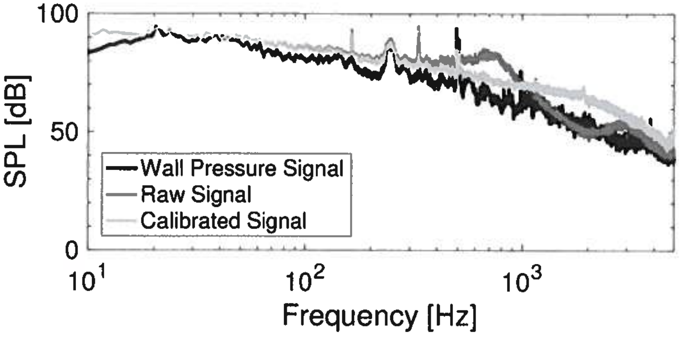

(b)

Figure 6.15: Effect of the fairing microphone compensation on the measured pressure spectrum for U_∞ = 10 m/s (up) and 15 m/s (down). Boundary layer with TGBs.

6.4.3. APPLICATION: CONTRA-ROTATING ROTOR MEASUREMENTS

Contra-rotating fan measurements are performed in the diffuser of the subsonic L1 wind tunnel in VKI (Fig. 6.1). The contra-rotating fans are 4.2 m in diameter and are driven by a 580 kW variable speed DC motor, allowing a continuous variation of the velocity in the 3 m diameter test section from 2 to 60 m/s. The diffuser is a circular divergent concrete duct with diameter starting from 4.2 m to reach 6 m over 20.4 m of length. A fairing was placed 13.20 m downstream of the fans. A free-field microphone with a wind shield was also installed at the same axial and azimuthal position, about 0.1 m above the fairing for comparison. The measurements were performed with a sampling rate of 25.6 kHz with 200,000 samples. The power spectral densities of the free-field microphone and the signal received from the fairing at 500 RPM are shown in Fig. 6.16. The

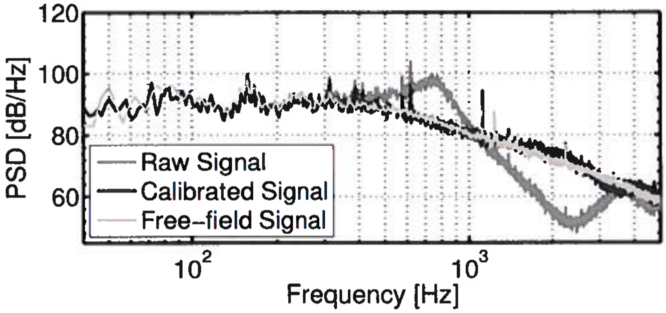

Figure 6.16: Comparison of the free-field microphone, raw and calibrated signals, 500 RPM.

signal received from the fairing is calibrated by applying the transfer function obtained from the calibration procedure described above. In the raw signal, a strong resonance peak around 0.75 kHz followed by an anti-resonance are observed due to the pipe-cavity system. However, after calibrating the signal using the measured transfer function, the artifacts of the line-cavity oscillating response are eliminated and a good match with the free-field wind-shielded microphone is obtained.

6.5. CONCLUSIONS AND PERSPECTIVES

The present work describes an experimental technique aimed at measuring aerodynamic noise in closed test section wind tunnels. The fairing approach permits installing microphones in wind tunnels where the duct walls cannot be conveniently altered, while minimizing the flow disturbances. The microphone is positioned horizontally inside the fairing and is remotely connected to the test section through a pipe-cavity system.

The design of the pipe-cavity system was performed following an analytical model, which proved good enough to derive the main dimensions. The model did however exhibit too much deviation from the measured response function to be used for calibration. A systematic calibration procedure has to be applied to each individual microphone line-cavity holder, which permitted to accurately compensate for the resonance and attenuation of the system.

The aerodynamic effect of the fairing was investigated in a small wind tunnel by means of hot-wire measurements for different velocities, and for low and high turbulence intensities. While it was verified that the fairing induces a strong acceleration of the flow, the expected benefits in terms of turbulence reduction were not observed. For the clean wall turbulent boundary layer case, the reduction of turbulence only occurs far from the wall but remains mostly unaffected in the immediate vicinity of the surface. And in the high incoming turbulence case, the near-wall turbulence is even observed to increase significantly in the presence of the fairing.

As a practical application, the noise emitted by the contra-rotating fan of the subsonic L1 wind tunnel was measured. A fairing was installed in the downstream part of the diffuser, together with a free-field microphone protected by a windshield. The positive match between the compensated fairing and free-field signals demonstrate again the effective compensation of the line-cavity resonance and attenuation effects. This validates the concept of fitting the microphones in an aerodynamically-shaped fairing to avoid introducing flow disturbances. However, further research is needed to reach a more thorough comprehension of the acoustic vs. hydrodynamic content of the measured signals. This might be achieved through modal decomposition of the pressure field measured by multiple fairing microphones, in order to extract the pressure component matching the expected acoustic propagation pattern in a slowly-diverging duct.

7

AN INVESTIGATION ON THE EFFECT OF THE INFLOW QUALITY

This section focuses on a preliminary experimental campaign to investigate the effect of inflow conditions on the aerodynamic performance and aeroacoustic installation effect for a Building Integrated Wind Turbine (BIWT). The building model of Brussels Finance Tower from a former study [141] is used with the straight duct model and wind turbine model. Two types of neutral Atmospheric Boundary Layer (ABL) conditions, from slightly rough and moderately rough classes, generated in the VKI L-1B wind tunnel are used for investigation of turbulence effects, and six angles from 0° to 75° are used to investigate the inflow orientation. The power measurements are performed for a wind turbine within the building and another one placed on the top of the building with varying angle of attacks and different inflow conditions. Furthermore, acoustic measurements within the duct are performed by nine flushed-mounted microphones with varying inflow characteristics and direction.

7.1. INTRODUCTION

Wind turbines have been utilized mainly in rural areas due to available space and established wind resources. As a drawback, it has sometimes caused a significant alteration of the landscape. Also, losses incurred during the transportation of electricity to the residential areas are penalizing the global efficiency. For these reasons, integrating wind turbines into the building environment is currently being considered, as it should minimize those loses and cause less damage to rural areas. However, there are some disadvantages as it is unsuitable to construct wind farms not only due to the lower speed and high turbulence caused by the surface roughness of the complex building arrangement but also due to the lack of space for large wind turbines in urban areas [145]. For this aspect, high-rise buildings offer an interesting compromise as the surface roughness has less effect on the urban area at higher altitudes, thus resulting in a higher velocity and low turbulence. Also, with a correct arrangement of the buildings, a funnel effect could

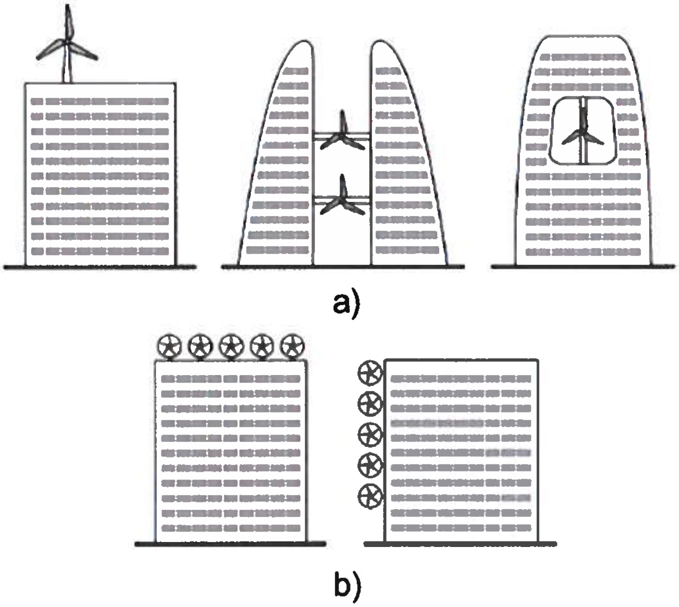

Figure 7.1: BIWT system using wind turbines: (a) three possible installations for large-size wind turbines, and (b) two possible installations for small size wind turbines [145].

be created [145]. Both of the aspects would lead to a velocity augmentation and thus, a higher power output. These types of wind turbines which are integrated to a building are called Building Integrated Wind Turbines (BIWT). Depending on the size of the wind turbine, the installation locations might change as illustrated in Fig. 7.1. For the small wind turbines, there are two possible installation locations: on top or alongside the building. For the wind turbines larger in size, they can only be placed on top or alongside the building, or within a duct.

Utilizing the small wind turbines within the building is considered an economical method, since the existing building can be used without additional modifications and structural strengthening [145]. However, the total output is found to be lower than the larger wind turbines since they can be installed into limited spaces [145]. For the larger wind turbines, the main issue is the structural strengthening due to the wind loads exposed to the wind turbine. Therefore, additional precautions need to be taken.

Regarding the installation location strategy of wind turbines, the configuration on top of buildings benefits from the higher wind speed as well as the less turbulent flow [177]. Moreover, the wind turbine location on the rooftop is interesting to avoid the recirculation zone of low velocity and high turbulence which is caused by the edge of the building. However, with wind turbines within an adjacent building or in a duct through a building, there is a benefit in the pressure difference between upstream and downstream faces of the building, which induces the velocity through the channel. The investigation conducted by BDSP Partnership [177], comparing seven BIWT configurations with their base model at the same height, found that the circular duct with smooth edges produces the maximum power production with respect to the different wind types of uniform wind, weakly and strongly unidirectional wind, and bi-directional wind. Although this configuration produces the maximum power generation, this also contributes to the acoustic nuisance due to the horn effect of such installation, which is particularly problematic in a densely populated urban environment. Moreover, the sound generation process is quite sensitive to the quality of the inflow, which can vary sensibly depending on the integration of the setup in the building, on the wind speed and direction, etc. Research is thus needed to better understand the aerodynamic performance vs. noise tradeoffs that can be achieved by BIWT configurations within the duct.

This section aims at investigating the effect of the inflow quality on the power generation as well as the acoustic installation of a wind turbine placed in a building-integrated duct. An experimental campaign is carried out in the VKI L1-B wind tunnel where two types of ABL are simulated as an incoming flow. Later, the inflow direction is investigated by varying the angle of attack. In addition, the power measurements are performed with two wind turbine configurations simultaneously; one is on the top of the building and the other one is in the duct for comparison.

7.2. EXPERIMENTAL SETUP, ACQUISITION CHAIN, AND POST-PROCESSING

7.2.1. BUILDING AND WIND TURBINE MODELS

In previous study [141], the Brussels Finance Tower Building of 145 m height shown in Fig. 7.2 is modelled with 1/200 scale as representing the high-rise building in an urban environment. The building model has a height of 0.725 m with 0.188 m of width and 0.439 m of length which are specified in Fig. 7.3.

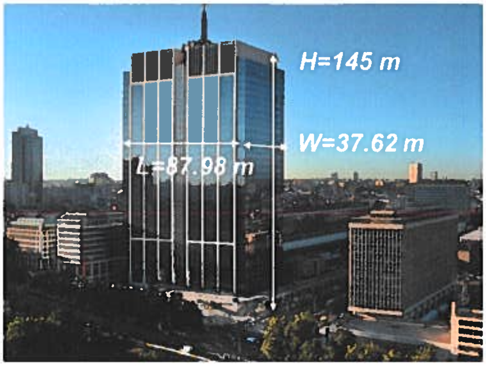

Figure 7.2: Brussels Finance Tower [1].

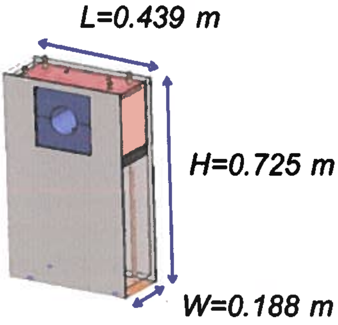

Figure 7.3: Building model.

In a the previous study, three different duct models and three different height configurations were investigated (details can be found in [141]). However, in this study only the straight duct which has a 0.102 m diameter at the highest position will be investigated.

---

[1] http://www.jaspers-eyers.be/finance-tower

It should be noted that the straight duct model has sharp edges in the inlet which differs from the other two duct designs in the previous study where the inlets were smoothly rounded. Thus, a separation might be observed in this configuration with a recirculation zone that may close upstream or downstream of the rotor plane depending on the incoming flow direction. However, a further investigation would be needed to analyse the flow at the inlet, which is not the aim of this study.

To investigate the power efficiency of the BIWT installation positions, a turbine is placed on the top of the building and another one is placed inside of the duct. Power measurement is performed for both wind turbines simultaneously and their configuration is given in Fig. 7.4. Hub heights of the in duct and roof mounted turbines from test section ground are 0.620 m and 0.855 m, respectively. When placing the top wind turbine, the middle position of the roof plane is considered without further investigating the separation due to the sharp edge and the recirculation zone caused by it.

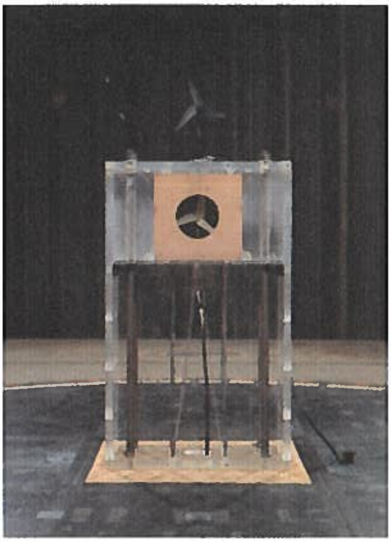

Figure 7.4: The in-duct and roof mounted turbine models.

The wind turbine model used on the top of the building has a HAM-STD HS1-606 airfoil type with 0.15 m diameter. The wind turbine used inside of the duct is an identical turbine, however, with a diameter of 0.1 m as the blades had to be cut to meet the blockage restriction [141]. For both wind turbines, a Maxon motor model-361773 is used as generator. Detailed drawings of wind turbine, duct and building models can be found in Appendix C.

To measure the noise from the ducted wind turbine, 9 flush mounted electret microphones Knowles model FG-23742-C05 are used as specified in Ref [141]. They are mounted on the duct in 3 azimuthal arrays: Upstream (U), Downstream (D), and Further Downstream (FD). The microphones which are in the same axial positions are numbered as # 1, 2 and 3. Figure 7.5 shows locations and numeration of the microphones. It should be noted that the aeroacoustics measurements are performed only with the in-duct configuration.

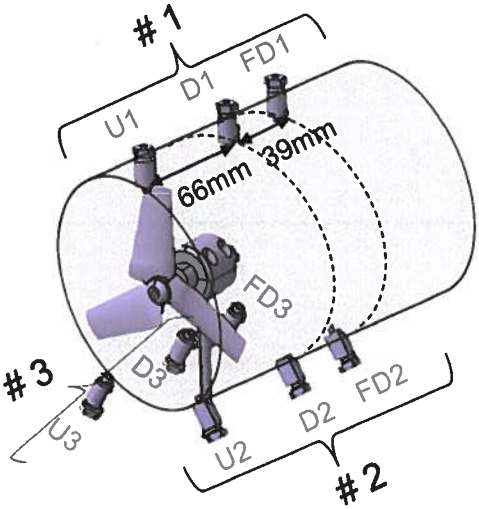

Figure 7.5: Microphone locations and numeration.

7.2.2. WIND TURBINE CHARACTERIZATION

To find the optimum operating condition for these wind turbines, their performance curves are taken from previous studies [50, 141]. Figure 7.6 shows the characterization of the wind turbines as a function of an electrical resistance versus the power coefficient with different velocities in the VKI L-12 facility, which has a 0.2×0.2 m test section, a maximum speed of 15 m/s and a 0.3% turbulence level [50, 141]. For both wind turbines, it can be observed that the power coefficient increases until an optimum resistance, and decreases afterwards. Each velocity curve has a different optimum resistance value. For the wind turbine mounted on top of the building, a velocity of 5 m/s shows a plateau from 2.5 to 8 ohm, with a consistent maximum for both velocities corresponding to 5.6 ohm. For the in-duct wind turbine, 6.8 ohm is chosen as an optimum resistance.

As mentioned before, both wind turbines have the same design except the in-duct wind turbine's blade is cut at the tip. Since the optimized blade geometry is altered it may produce less energy than the wind turbine on the top of the building. The power coefficient of both wind turbines with different resistances are calculated from Eq. 7.4 and given in Fig. 7.6 which indicates that the top wind turbine has a higher power coefficient than the in-duct wind turbine.

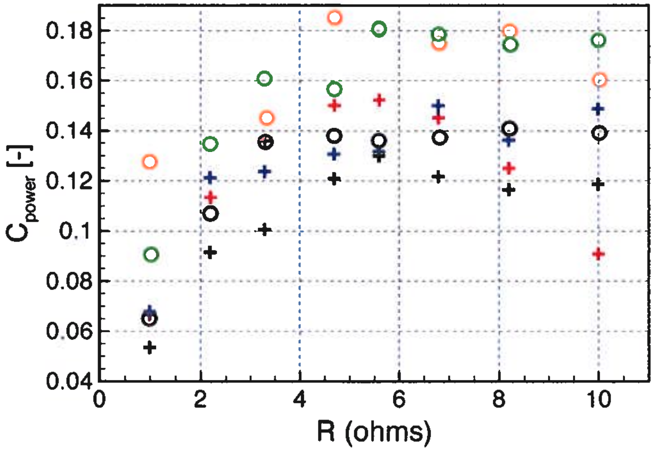

Figure 7.6: Power coefficient results as a function of resistance, taken from previous studies; wind turbine in-duct (+): 5 m/s (black), 7.5 m/s (red), and 10 m/s (blue) [141]; wind turbine on top (∘): 5 m/s (black), 7 m/s (yellow), and 8 m/s (green) [50].

7.2.3. ATMOSPHERIC BOUNDARY LAYER TYPE

The ABL consists of two layers: the inner region and the outer region. The outer region, which is also called as the *Ekman layer*, has little dependence on the nature of surface; however the Coriolis force due to the rotation of the Earth has an important role. On the contrary, the inner region of the ABL surface layer is dependent on the surface characteristics and shows almost no dependence on the rotational motion. The influence of surface, which consists of roughness elements, is directly felt at the interfacial sub-layer, which is the layer of air within and just above the roughness elements of the surface [74]. The height of the ABL and the turbulence intensity are dependent on thermal stratification, in addition to the rotational motion of Earth and its surface roughness. The stratification is said to be neutral when the air rising from the surface is in thermal equilibrium with the surrounding air. The occurrence of a neutral state in the case of strong winds is therefore the most important to consider. It also represents an average condition between stable and unstable ABL conditions [50]. The vertical velocity profile in neutral conditions, in the surface layer, with no pressure gradient is described by the logarithmic law

$$\frac{U}{u_*} = \frac{1}{\kappa} \ln\left(\frac{z}{z_0}\right) \tag{7.1}$$

where u_* is the friction velocity and z_0 is the aerodynamic roughness length. z_0, a function of real surface roughness.

The mean velocity profile is often approximated,

$$\frac{U}{U_{ref}} = \left(\frac{z}{z_{ref}}\right)^{\alpha}_{ABL} \tag{7.2}$$

where U_{ref} is the reference velocity at a reference height z_{ref}, and α is the power law coefficient. Roughness classes of ABL determined by z_0 and α_{ABL} values can be found in VDI [54] and Eurocode [176] standards.

The VKI L1-B wind turbine mentioned in Sec. 6.4.3 is chosen to model the neutral ABL. Two configurations: with grid (G) and with grid, fence and cups (GFC) are reproduced from an existing study [42]. For the first configuration, only the monoplane grid which has a mesh size of 0.02×0.02 m is used. For the second configuration, a 0.15 m fence is placed in front of the grid and 32 mm height cups are placed within the 12 m before the test section as shown in Fig. 7.7 and Fig. 7.8. From the previous studies [32, 48], the type of ABLs are found to be *slightly rough* for the G configuration and *moderately rough* for the GFC configuration.

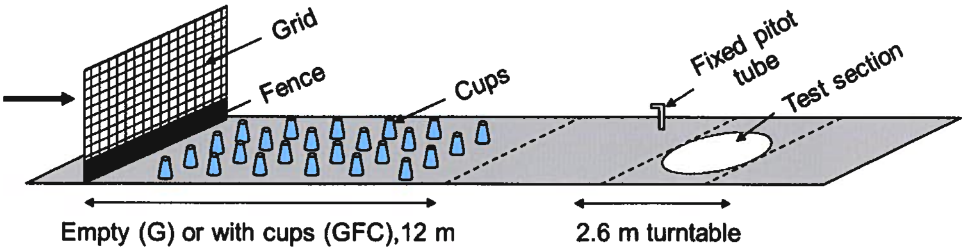

Figure 7.7: The configuration of the ABL in the VKI L1-B wind tunnel.

In order to characterize the wind tunnel ABL 3C-HWA measurements are carried out just upstream of the turntable and on the central axis of the test section. Streamwise velocity and turbulence intensity profiles are obtained along vertical traverses from height of 0.01 m to 0.32 m. The wind tunnel reference velocity is measured by a pitot tube at 0.13 m above the test section ground upstream of the turntable. It was measured to be 8 m/s. Note that the reference pitot tube is located within the boundary layer. The mean axial velocity and turbulent intensity profile are shown in Fig. 7.9. In each measurement campaign, the velocity profile is corrected by the reference Pitot-Prandtl tube by the following formula assuming a linear relationship:

$$U = U_{ref}(z)\frac{U_{pitot(z_{ref})}}{U_{ref}(z_{ref})} \tag{7.3}$$

where U is the corrected average velocity, U_{ref} is the average velocity of the reference ABL measurements, U_{pitot} is the speed measured from reference Pitot-Prandtl tube, z is the height from the ground of test section, and z_{ref} the fixed height of Pitot-Prandtl tube.

The mean velocity at the hub level of the ducted wind turbine is 0.3 m/s higher for the GFC ABL configuration than for the G configuration. Simultaneously, the turbulence intensity doubles from the G ABL configuration to GFC. The main difference between two ABL configurations is thus the turbulence level that is ingested by the ducted wind turbine rotor.

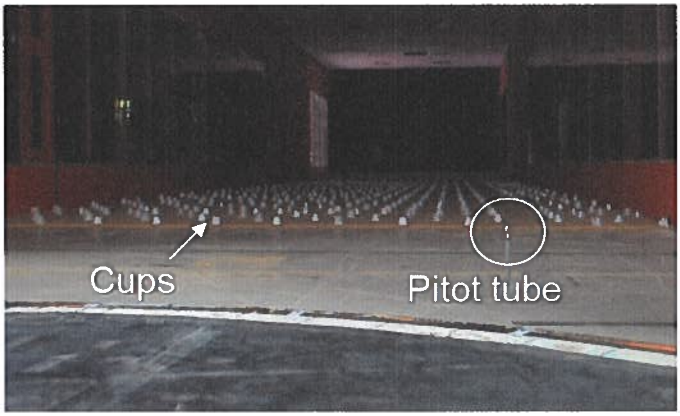

Figure 7.8: The cups and reference Pitot-Prandtl tube in L-1B wind tunnel test section.

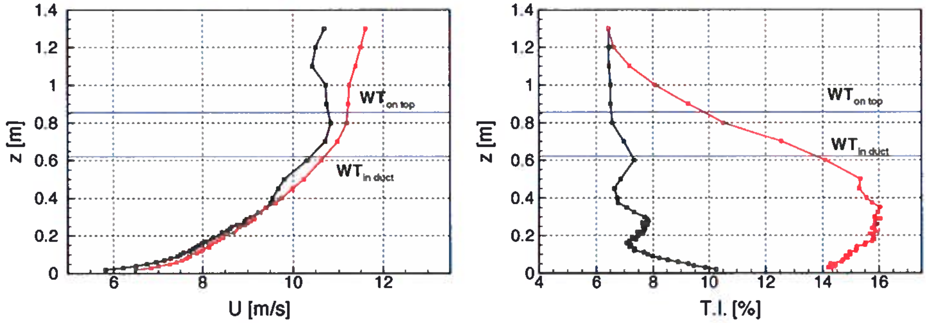

(a) Mean velocity profile.

(b) Turbulent intensity profile.

Figure 7.9: Mean velocity and turbulence intensity (T.I.) profiles of G (black) and GFC (red) ABL configurations.

7.2.4. ACQUISITION CHAIN AND POST-PROCESSING

The instrumentation chain consists of one pitot tube to monitor the inflow velocity, two power measurements for the two wind turbines with a control board, and nine microphones that are placed inside the duct. The power generated by both wind turbines is measured simultaneously. For the acoustic measurements, the top roof wind turbine is removed in order to avoid contaminating the noise measurements of the ducted one. Both measurements are performed for two ABL flow types and six incoming flow directions.

The data acquisition system consists of a PXI system whose components are included a PXIe-1065 chassis, a PXIe-8840 controller, and several PXI DC modules. For simplicity, the same sampling rate is used for all channels.

A pressure transducer with a range of ±0.75 psi is used for the pitot tube.

The power generated by both wind turbines (in-duct and top) is measured simultaneously with an in-house control board [19, 50]. The electrical circuit of the board contains a resistance that dissipates the power generated by the wind turbine. Different tip-speed ratios are obtained for different values of that adjustable resistance. The control board has three BNC outputs. The first output enables the measurement of the rotational speed of the wind turbine from the voltage of the generator's encoder. The second output gives a voltage signal image of the current generated by the wind turbine (I) which can be obtained by an ampere-meter plugged to the control board. The last output provides the wind turbines generator's voltage (V) [50]. From the below equation, the power coefficient is calculated as:

$$C_{power} = \frac{P_{electrical}}{P_{wind}} = \frac{V \cdot I}{\frac{1}{2}\rho A_s U_{hub}^3} \tag{7.4}$$

where A_s is the swept area of the wind turbine rotor and U_{hub} is the incoming velocity at hub level. The details of the control board are given in Appendix C.2. The rotational speed outputs of the turbines are connected to the PXI module whereas the output voltage is acquired by the aforementioned National Instrument PXI acquisition board with a sampling rate of 51.2 kHz and over a duration of 120 s. The voltage output is acquired by a National Instrument CompaqDAC NI9215 system at a sampling rate of 12.8 kHz and for 120 s as well. The current output is displayed by a simple hand-held multimeter.

The calibration of the microphones is not performed, being difficult to perform in situ for this case. The microphones' signals are sampled by the above mentioned PXI system for 120 s at 51.2 kHz. The power spectrum density is obtained using the MATLAB *pwelch* function, where the signal is divided into 2^{14} sample segments with 50% overlap and applying a Hanning window.

7.3. POWER MEASUREMENTS

As stated before, a difference between the wind turbines is that different resistances are used for the power measurements. A resistance of 5.6 ohm was used for the top wind turbine, whereas 6.8 ohm was used for the in-duct wind turbine to operate at the optimum conditions. These were determined by the previous studies conducted in the VKI L12 wind tunnel as mentioned before. Secondly, their swept areas are different since the in-duct wind turbine blades are cut to fit within the duct. Thirdly, the inflow velocity at the hub, U_{hub} is different for both wind turbines. However, the formulation given in Eq. 7.4 is a dimensionless number based on the velocity, U_{hub} and the swept area, A_s. Therefore, the two turbines can be compared as shown in Fig. 7.10 with two ABL configurations: G (black) and GFC (red) with respect to six inflow directions.

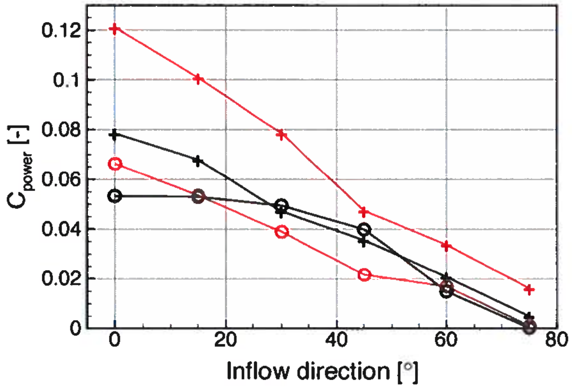

Figure 7.10: The power coefficient of the two wind turbines; WT in-duct (+) and WT on top (○), as a function of inflow direction for the G (black) and GFC (red) configurations.

Also, the variation of the hub velocity U_{hub} that would inevitably result from a variation of the inflow direction wasn't measured. The same reference velocity, obtained from Fig. 7.9, was therefore used for the normalization of the power measurements.

By taking into consideration all the aforementioned explanations, it could be interpreted that the wind turbines perform better with the GFC ABL configuration than the G ABL configuration except for the top wind turbine between 30° to 45°. The GFC ABL configuration has a slightly higher velocity compared with the G ABL configuration at both hub locations, which is likely not sufficient to explain the comparatively larger power increase. The much more substantial increase of the turbulence intensity may thus play a role in this power increase. However, we lack sufficient information regarding the incoming velocity and turbulence intensity just upstream of the building to draw definitive conclusions.

When the two wind turbines are compared, it is observed that the in-duct wind turbine has a higher power coefficient than the top wind turbine. If the top wind turbine is not placed in the recirculation zone, one possible explanation is that the venturi effect increases the velocity, thus resulting in a higher velocity than the top wind turbine.

7.4. ACOUSTIC MEASUREMENTS

The acoustic measurements are performed with three configurations; no flow and no wind turbine, flow and no wind turbine, and flow and wind turbine with two ABL profiles and six wind directions. As a first step, the background noise of the facility is measured by the nine microphones is shown in Fig. 7.11. This noise is the electrical noise, with tones at 50 Hz frequency and higher harmonics.

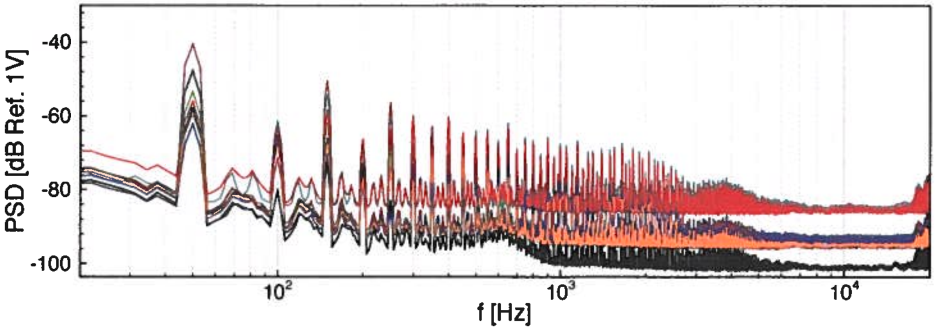

Figure 7.11: PSD of all microphones in no flow configuration as a function of frequency.

Before investigating the noise characteristics of a wind turbine, the remaining system characteristics were analysed by removing the wind turbine. Figure 7.12 shows the PSD of each azimuthal microphones at three axial positions with the G and the GFC ABL configurations at 0° wind direction. The microphones at the azimuthal locations #2 and #3 show the same spectral shape, different from the results obtained at the azimuthal location #1. It should be reminded that the microphones haven't been calibrated in amplitude. When comparing the different ABL profiles with the same microphone, it is observed that the amplitude of the PSD is higher with the GFC ABL configuration than the G ABL configuration. This can be related to the higher turbulence intensities.

With the wind turbines in place, the measured Blade Passing Frequency (BPF) for both ABL configurations with six inflow directions have been obtained from the spectra (see Fig. 7.13 for the 0° deg wind direction), and have been gathered in Table 7.1. When the inflow direction increases, the mass flow passing through the duct decreases, which results in a lower BPF except for the GFC ABL configuration at 15° wind direction. In addition, it is observed that the BPF difference between 0° and 15° wind direction are the lowest compared to the other configurations. This effect might be due to the guiding effect of the duct. For the two ABL configurations, it is observed that a higher BPF is obtained from the GFC ABL configuration. Figure 7.13(a) shows the position of the BPF for the G ABL configuration, where half harmonics are also observed which may due to unequal spacing or the alignment of the wind turbine.

Table 7.1: Blade passing frequency values at all configurations

	0°	15°	30°	45°	60	75°
G	433.57 Hz	428.57 Hz	394.56 Hz	345.85 Hz	301.43 Hz	241.74 Hz
GFC	528.19 Hz	533.56 Hz	473.88 Hz	430.30 Hz	370.36 Hz	305.35 Hz

Figure 7.13 shows the PSD of each azimuthal microphones at three axial position

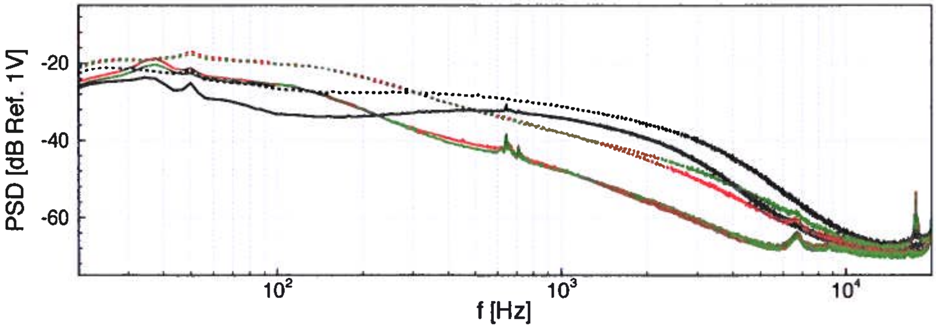

(a) Upstream microphone configuration.

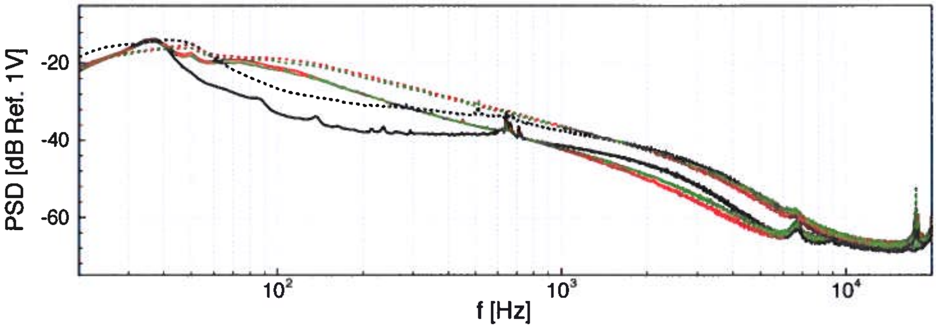

(b) Downstream microphone configuration.

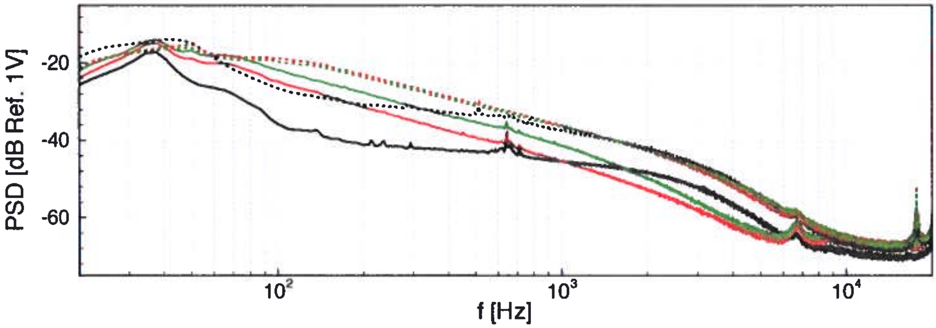

(c) Further downstream microphone configuration.

Figure 7.12: PSD of the microphones without wind turbine at 0° inflow direction with two incoming flow; G (solid line) and GFC (dashed line), Microphones; # 1 (black), 2 (red) and 3 (green).

with and without wind turbine which were performed at 0° wind direction with the G ABL configuration. It can be seen that for the low frequency part the amplitude of the PSD is higher without the wind turbines than with them. This could be explained by a lower velocity due to the wind turbine blockage within the duct. Furthermore, it is also observed that the BPF and its harmonics are more pronounced upstream of the wind turbine. The same figures are given for the GFC ABL configuration in Appendix C.3.

In order to compare the effects of the two ABL configurations, the results for microphone # 3 is selected at 0° wind direction and are shown in Fig. 7.14. A broadening of the BPF tones is observed with the GFC ABL configuration due to an increase in the turbulence intensity. The amplitude difference is not significant for the upstream location for frequencies below the first BPF where the harmonics are still present. For higher frequencies, the broadband noise shows that the amplitude is higher for the GFC ABL configuration, which might be due to higher velocity as well as higher turbulence intensity. The downstream and further downstream positions show a significant amplitude augmentation for the lower frequencies, and they show another peak trend which is different from the upstream locations. Those peaks are not aligned with BPF and change with the ABL configuration.

The effects of changing the wind direction are given in Fig. 7.15 for microphones #3 in the GFC ABL configuration. In order to observe the trend with respect to the wind direction change, three values are selected; 0° (black), 30° (red) and 60° (green). It has been observed that the BPF decreases with increasing wind direction. The half harmonics of the BPF which were observed are now found to be less pronounced with the wind direction above 30°. However, the BPF amplitude and the PSD amplitude itself, increased with a higher inflow direction, especially for the broadband noise for the upstream microphone which could be due to the increase in the T.I. For the downstream and further downstream positions, again a similar behavior is observed: an increase in the amplitude before the BPF and after the BPF, the amplitude of the spectrum almost remains the same for different inflow directions. This might be associated with the stall self-noise where the large coherent eddies emit the noise at a lower frequency. In addition, the tonal peaks are those which are observed in the previous figure and show that those peaks are independent on the flow conditions and the duct characteristics, which might be due to the electrical or mechanical noise.

7.5. CONCLUSIONS

In this section, a preliminary experimental study has been performed to investigate the effect of the inflow quality on the power produced and noise emitted by a Building Integrated Wind Turbine (BIWT). The building model is selected from a previous study [141] which is a 1/200 scaled down model of Brussels Finance Tower, and a straight duct model, where the wind turbine is placed inside the duct. In addition, to investigate the benefits of the BIWT installation locations, another wind turbine is placed on the top of the building.

As the focus of the current research is to investigate the effects of the quality and direction of the flow on wind turbine performance and acoustic emission rather than to quantify the ABL type, two different neutral Atmospheric Boundary Layer (ABL) profiles are regenerated from a previous study [42]. These inlet profiles in the VKI L1-B wind tunnel are the only with Grid (G) and with Grid+Fence+Cups (GFC) configurations. Both profiles provide a similar velocity profile which changes by around 0.4 m/s, while the turbulence intensity (T.I.) increases significantly with the GFC configuration; around 7% for the in-duct wind turbine compared to 3% for the top wind turbine. To vary the inflow direction, six wind directions from 0° to 75° are performed by rotating a turntable which the building model is placed on.

The power coefficient, which is non-dimensionalized by the swept area of the wind turbine and the velocity at the hub, is higher when the T.I. is increased except for the top wind turbine between 30° and 45° inflow direction. It is also observed that the top wind turbine seems more insensitive to the T.I. than the in-duct wind turbine. Overall, when the two wind turbines are compared, the in-duct wind turbine produces more power than the top wind turbine.

The acoustic measurements are performed by nine microphones placed in three axial positions; upstream, downstream, and further downstream and three microphones in each axial location. The measurements are performed with and without the wind turbine, where it is observed that the amplitude of the spectrum decreases when the wind turbine is present due to the blockage effect. It is also observed that the turbulence interaction noise is more dominant on the upstream location than the other locations since the Blade Passing Frequencies (BPF) and its harmonics are only observed in the upstream position, while the peaks are attenuated while moving downstream; only the BPFs which have more energy content remain. The comparison of the incoming flow is investigated by one azimuthal location along the three axial positions as a function of frequency divided by BPF. It is observed that the peaks obtained from the GFC ABL configuration are wider and their peak points are more rounded than the G ABL configuration. Moreover, the small peaks observed from the G ABL configuration, which might be due to misalignment of the wind turbine or unequal blades, are suppressed by the noise which results in smoother peaks. When different axial locations are investigated, similarly, the BPF and its harmonics are more present in the upstream microphone position than the downstream ones. Moreover, the amplitude difference and the width of the peaks are wider for the downstream locations. As a last step, the inflow direction variation was investigated by considering only three angles 0°, 30° and 60° wind directions for one azimuthal location along three axial positions. As expected, increasing the wind direction reduced the velocity, and thus the BPF and its harmonics shift to left. Moreover, two different behaviors are observed depending on the axial location. With respect to the upstream microphone, the low frequency range seems less effected by the wind direction, however, a broadband noise increase is observed for the higher frequencies. On the contrary, the downstream microphones seem more sensitive to the inflow direction for the low frequency range than the higher frequencies.

In future work, the ABL profile could be obtained when the building is present with different wind directions. to investigate the blockage effect of the model and properly obtain the inlet velocity. Furthermore, to better understand the flow field around and inside the duct, a Particle Image Velocimetry (PIV) measurement could be performed. This would give more information about the separation due to the sharp edge of the duct and the building, as well as the vortices formed due to tip leakage. Lastly, a microphone calibration would help to more quantify and characterize the noise emitted by the wind turbine and the in-duct model decomposition technique could be applied to investigate the propagation of the acoustic waves inside the duct.

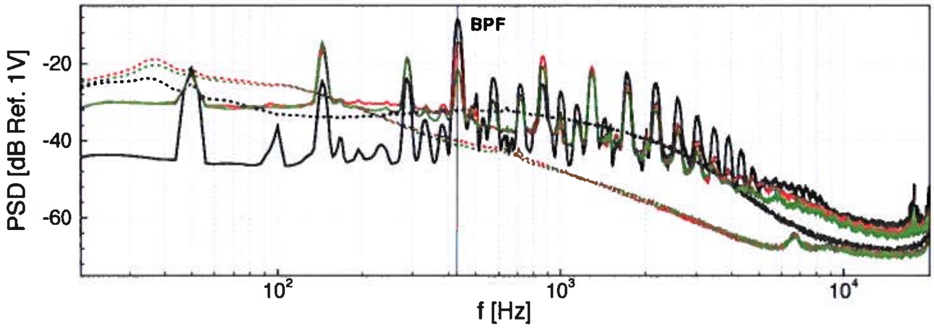

(a) Upstream microphone configuration.

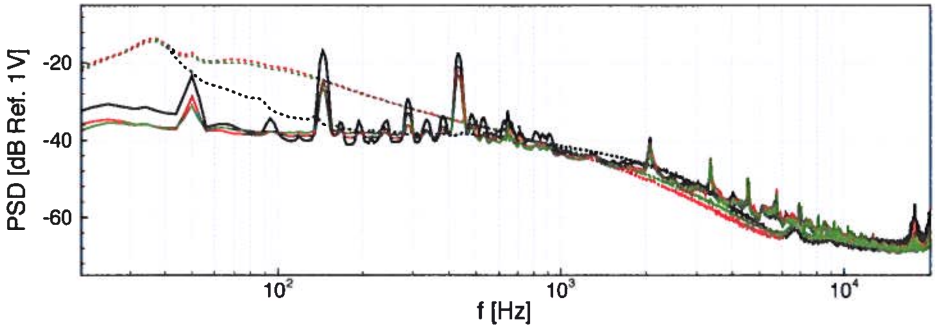

(b) Downstream microphone configuration.

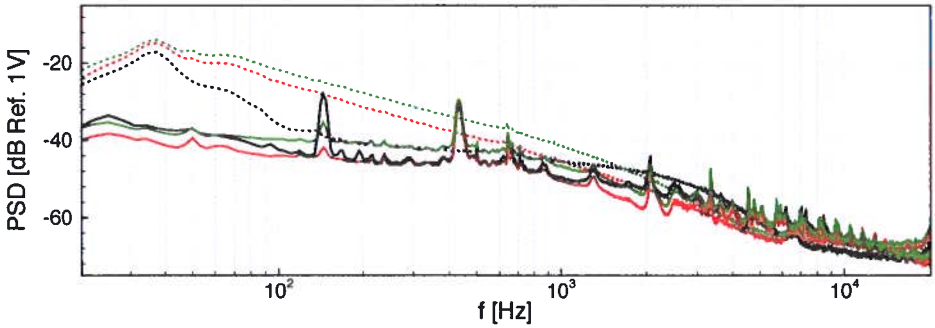

(c) Further downstream microphone configuration.

Figure 7.13: PSD comparison with and without wind turbine at 0° wind direction for the G ABL configuration; with wind turbine (solid line) and without wind turbine (dashed line). Microphones; # 1 (black), 2 (red) and 3 (green).

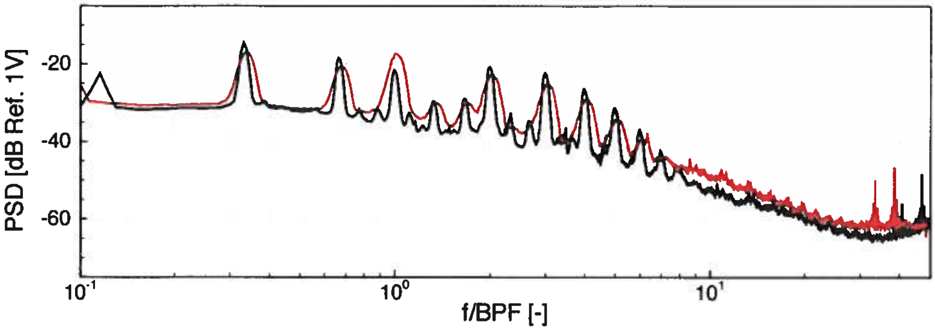

(a) Upstream microphone #3.

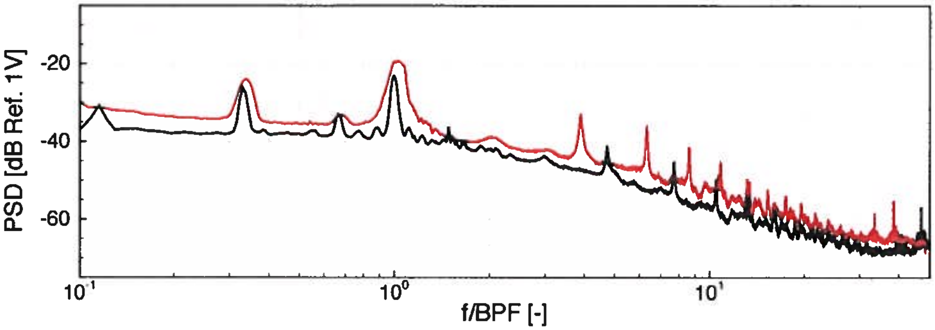

(b) Downstream microphone #3.

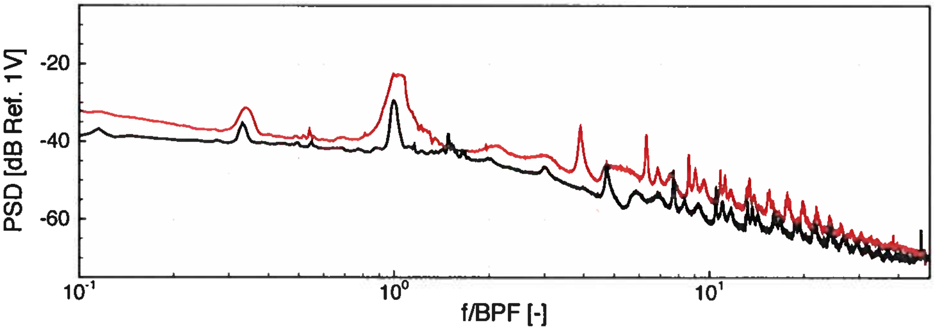

(c) Further downstream microphone #3.

Figure 7.14: PSD comparison of microphones # 3 with respect to incoming flow; G (—) and GFC (—).

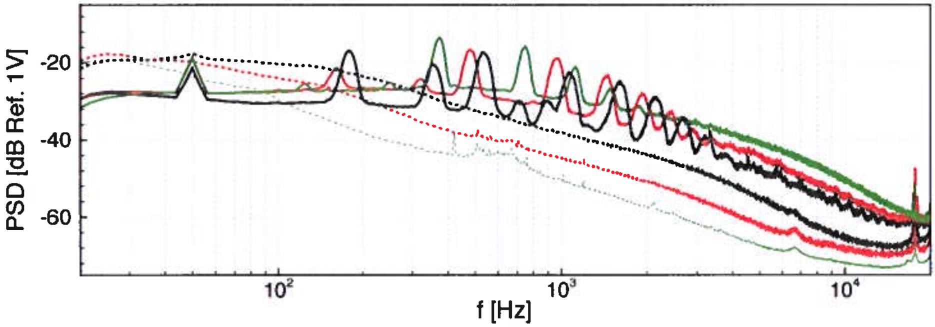

(a) Upstream microphone #3.

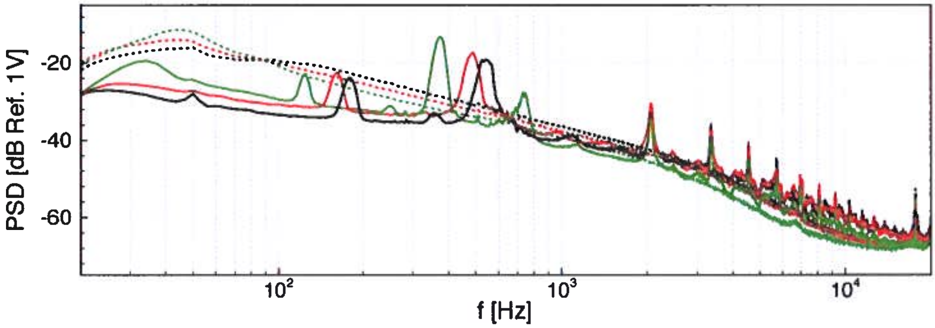

(b) Downstream microphone #3.

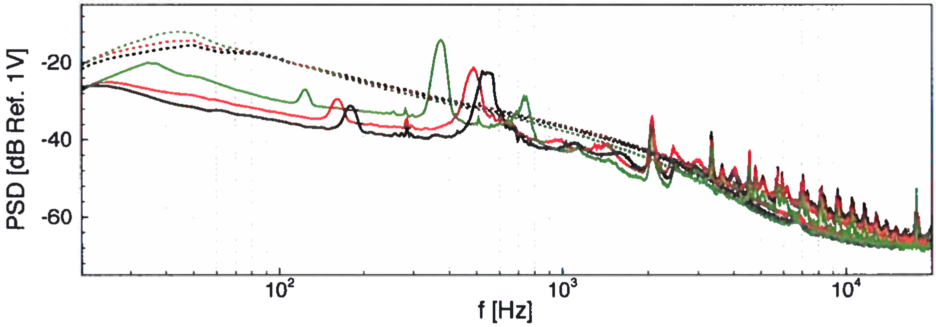

(c) Further downstream microphone #3.

Figure 7.15: PSD comparison of microphones # 3 with and without wind turbine with the GFC ABL configuration at different wind directions; with wind turbine (solid line) and without wind turbine (dashed line), 0° (black), 30° (red) and 60° (green).

8

CONCLUSIONS

This chapter focuses on the summary of the thesis with its main results followed by the future work and further improvements.

8.1. SUMMARY AND MAIN RESULTS

In this study, the noise emitted by a ducted wind turbine is investigated both numerically and experimentally. The numerical part, which is denoted as Part I, focuses on the accuracy, validation and development of low cost methods to predict the far-field trailing edge noise. To achieve this, Amiet's theory, which relates the statistical description of the pressure field beneath the incoming turbulent boundary layer to the acoustic field, is applied. The state-of-art wall-pressure models are tuned based on RANS simulations and their accuracy with respect to the different mesh resolutions is investigated for an isolated airfoil. Further analyses are performed on a full scale of a commercial ducted wind turbine by neglecting the scattering due to the diffuser. As a final step, to reduce the computational time, a 2D approach based on the strip theory is applied. The acceleration due to the diffuser and nacelle is imposed as an inlet condition which is obtained from a 2D axisymmetric simulation without blade. In the experimental part, two different aspects are investigated. First, the development of a remote microphone measurement technique which can be placed on the duct surface in order to acquire the noise emitted by rotating machines is proposed. Second, the effect of the aerodynamic roughness on the noise emission is evaluated for a building-integrated wind turbine. Furthermore, the suitable siting position of a wind turbine is investigated by comparing the power efficiency of a wind turbine within a duct and on the top of the building.

The far-field trailing edge noise is predicted by Amiet's theory for NACA0012 and DU96-W-180 airfoils at 0° and 4° angle of attacks, respectively, in Chapter 4. 2D RANS simulations are performed by the $k-\Omega$ SST turbulence model and the turbulent boundary layer profiles are extracted at $x/c = 0.99$ from the leading edge. The wall-pressure spectrum is computed by semi-empirical models which are Goody (assuming ZPG), Rozenberg, Kamruzzaman, Catlett, Hu & Herr and Lee (assuming APG) and an integral method (Panton & Linebarger). The grid sensitivity analysis is performed for both airfoils with different grid resolutions characterized by the non-dimensional wall-normal units, y^+. Overall, the pressure coefficient for both airfoils shows mesh independent results whereas the turbulent boundary layer profiles in terms of the wall-normal velocity (only for the DU96-W-180 airfoil), the kinetic energy and the specific dissipation for both airfoils exhibit some sensitivity with respect to the mesh resolution. The wall-pressure spectrum obtained by the semi-empirical models are insensitive to the mesh resolution, while the spectrum obtained by the Panton & Linebarger model performs mesh independence for $y^+ < 5$ for the NACA0012 airfoil. When the wall-pressure spectrum is compared with the NACA0012 airfoil experimental data, it is concluded that the Goody model is not accurate for the APG flow. Even though, the Cattlett and Hu & Herr models are developed for APG flows, a poor prediction is observed, which can be related to the scaling of the flat-plate experimental data. For the DU96-W-180 airfoil, it is concluded that the suction side, which contributes to the low frequency of the spectrum, is more mesh-dependent than the pressure side which dominates the higher frequencies. A mesh independent solution for these airfoils and the flow solver is obtained for $y^+ < 15$ for $kc > 10$. Moreover, the Kamruzzaman and the Panton & Linebarger models are found to be generally applicable. When the probe location is varied along the trailing edge, it is concluded that the far-field noise predictions by the semi-empirical models are sensitive to the probe location for $kc < 10$.

As a next step, a full scale of a commercial ducted wind turbine is simulated by 3D incompressible RANS with the $k-\Omega$ SST turbulence model in Chapter 5. The Coriolis and centrifugal effects are considered by applying a MRF methodology. The far-field trailing edge noise is predicted by applying the Schlinker and Amiet theory. An alternative approach based on a 2D strip theory is proposed to reduce the computational time required for the 3D RANS simulation. In this method, the blade is divided into strips and 2D RANS simulations are performed for each strip location to obtain the turbulent boundary layer near the trailing edge. A further improvement of this method is introduced by taking into account the acceleration due to the diffuser and nacelle. This is achieved by extracting the axial velocity profiles from a 2D axisymmetric simulation without blade and imposing these profiles as the inlet conditions to the 2D strip simulations. Even though the comparison between the 3D simulation and 2D simulations obtained by the improved inlet conditions demonstrates a close match with respect to the axial velocity extracted upstream of the blades, the azimuthal velocity and the pressure coefficient exhibit a poor match. The same observation was made regarding the turbulent boundary layer profiles extracted at $x/c = 0.99$. In general, the wall-pressure spectrum obtained by the Panton & Linebarger model from the 3D simulation show lower levels than other models both for the 2D and 3D simulations. This might be due to the fact that the kinetic energy is under-predicted. The far-field noise prediction obtained by the Kamruzzaman model imposing the inlet velocity at $z/c = -5.0$ agrees well with the 3D simulation at higher frequencies. In terms of the computation cost, the 2D simulations with the acceleration correction is about two orders of magnitude faster than corresponding 3D simulations.

The development of a measurement device based on a remote microphone is introduced in Chapter 6.2. The main purpose of this fairing is to enable the acquisition of the noise emitted by rotating machines where the duct surface cannot be altered. The device is designed using a streamlined profile, where the microphone is connected to the surrounding with a pipe-cavity system. An analytical model is used to design the pipe-cavity system. However, the model deviates significantly compared to the response function of the signal. The aim of the streamlined design is not to disturb the flow and to make use of local acceleration which would reduce the turbulence level on the pressure tap and that would increase the noise to signal ratio. However, it is found that near-wall turbulence significantly increases when the incoming turbulence level is high. Contrary to this, a practical application where noise emitted by a contra-rotating fan is measured, the fairing and a free-field microphone reveals a good match.

In Chapter 7, a preliminary experimental study is conducted to investigate the effect of inflow conditions, in terms of wind speed and direction, on the power production and the noise emission of a BIWT through a duct. Two different neutral ABL profiles, corresponding to different aerodynamic roughness lengths and turbulence intensities, are imposed as inlet profiles. Furthermore, another wind turbine is placed on the top of the building to assess the best siting within the building by comparing the power efficiency. Although the two ABL configurations provide a similar velocity profile, the turbulence intensity obtained by the GFC configuration is 7% and 3% higher than the G configuration for the in-duct and top wind turbine, respectively. It is concluded that the power produced by the in-duct wind turbine is higher than the top wind turbine while the top wind turbine appears to be less sensitive to the inflow direction than the in-duct wind turbine. From the noise measurements obtained within the duct demonstrate that the turbulence interaction noise is more dominant upstream of the wind turbine than downstream. Furthermore, broad peaks are observed when the turbulence level is higher and with higher magnitudes.

8.2. FUTURE RESEARCH AND POSSIBLE FURTHER IMPROVEMENTS

Reminding that the grid sensitivity study is investigated using only one eddy-viscosity model, $k-\Omega$ SST, further analysis with different turbulence models and numerical schemes would be recommended.

As the Corcos model is not physically consistent in the low-frequency regime, more accurate models such as Efimstsov and Smolyakov could be used to calculate the far-field spectrum.

When performing the 2D strip theory, only the axial acceleration is taken into account by applying a correction from a 2D axisymmetric simulation. However, the comparison with the 3D simulation exhibits a significant different when the azimuthal axial profiles are compared. Therefore, an analysis could be also performed by changing the rotational speed to take the three-dimensional effects into account.

In literature, there are several correction for BEM to take into account the three-dimensional effects. So that the inlet conditions acquired with a BEM method can be imposed to the 2D strip theory simulations to parametrize the 3D effects for a 2D simulation.

Further verification experiments can also be performed to test the consistency between the reproduced inflow conditions at the L1 wind tunnel with and without a building.

In this study, two wind turbines with the same blade design are used. However, the blades of the ducted wind turbine is cut in order to sit inside the building. Therefore, another possible future study can focus on the performance comparison of identical wind turbines.

A

GLOBAL BOUNDARY LAYER VARIABLES WITH RESPECT TO PROBE LOCATION

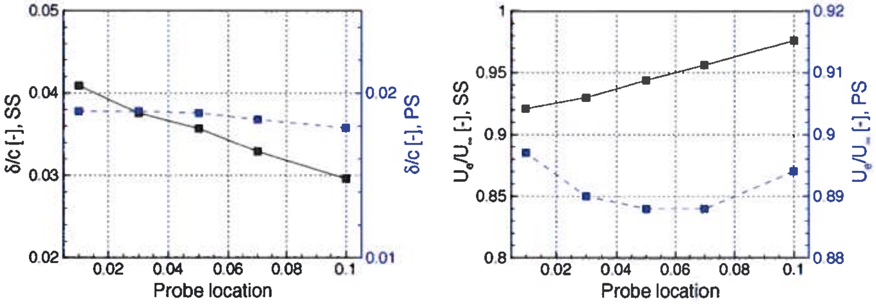

(a) Boundary layer thickness.

(b) External velocity.

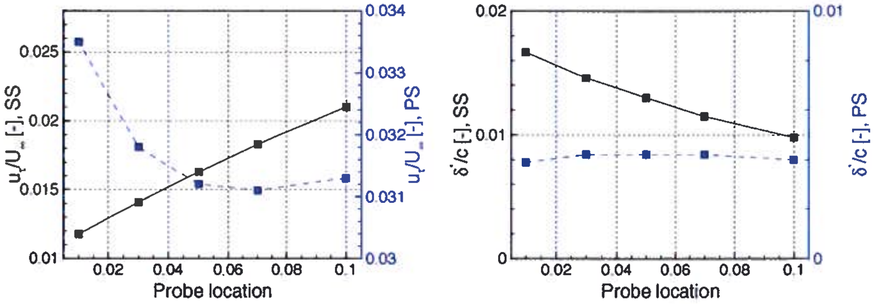

(c) Friction velocity.

(d) Boundary layer displacement thickness.

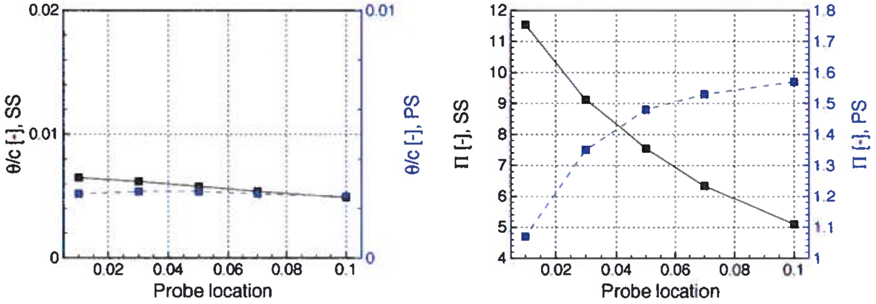

(e) Boundary layer momentum thickness.

(f) Coles' wake parameter.

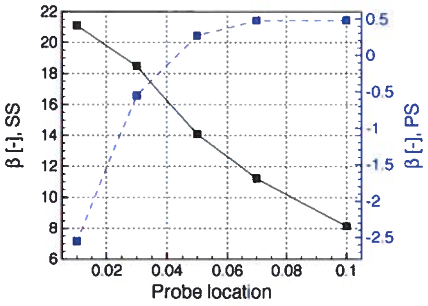

(g) Clauser equilibrium parameter.

Figure A.1: Non-dimensional boundary layer values along the DU96-W-180 airfoil; (black line: suction side, blue dashed line: pressure side).

B

BOUNDARY LAYER PROFILES FROM 3D SIMULATION

B.1. MESH SENSITIVITY

The wall-normal and spanwise velocity profiles extracted at $x/c = 0.99$ from the leading edge with respect to the different mesh resolution are given as:

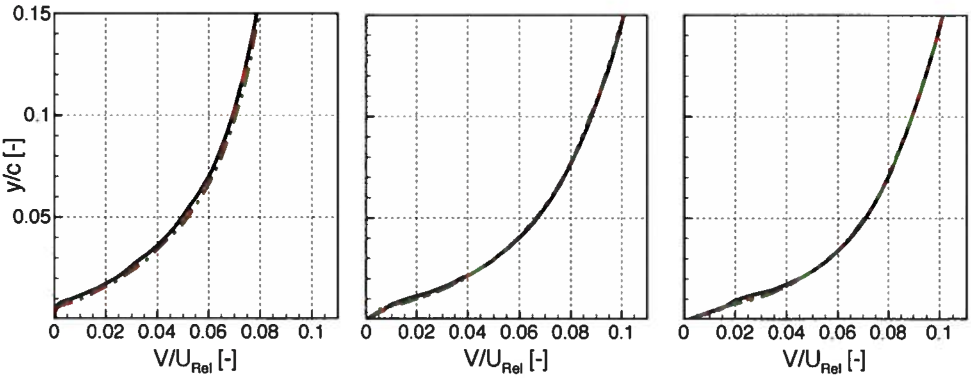

(a) Strip 1.

(b) Strip 2.

(c) Strip 3.

Figure B.1: The wall-normal velocity profiles at x/c =0.99 from the leading edge at each strip location with different mesh resolutions; $y^+_{ave} \simeq 2.5$ (——), $y^+_{ave} \simeq 2$ (- - -), $y^+_{ave} \simeq 1.6$ (-·-·).

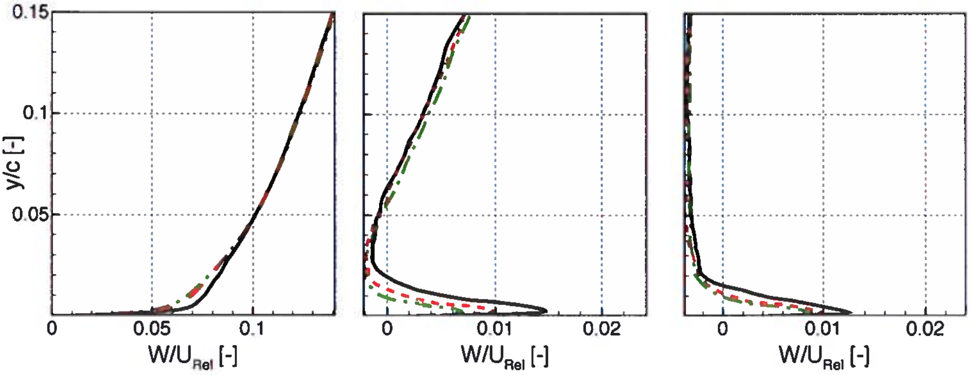

(a) Strip 1. (b) Strip 2. (c) Strip 3.

Figure B.2: The spanwise velocity profiles at x/c =0.99 from the leading edge at each strip location with different mesh resolutions; $y^+_{ave} \simeq 2.5$ (——), $y^+_{ave} \simeq 2$ (- - -), $y^+_{ave} \simeq 1.6$ (-·-·).

B.2. BOUNDARY LAYER COMPARISON BETWEEN 2D AND 3D SIMULATIONS

The comparison of the kinetic energy profile and the specific dissipation rate extracted at $x/c = 0.99$ from the leading edge with 2D and 3D simulations is given in Fig. B.3 and Fig. B.4.

B.3. GLOBAL BOUNDARY LAYER VARIABLES

The global boundary layer variables obtained from 2D and 3D simulations are given in the following table.

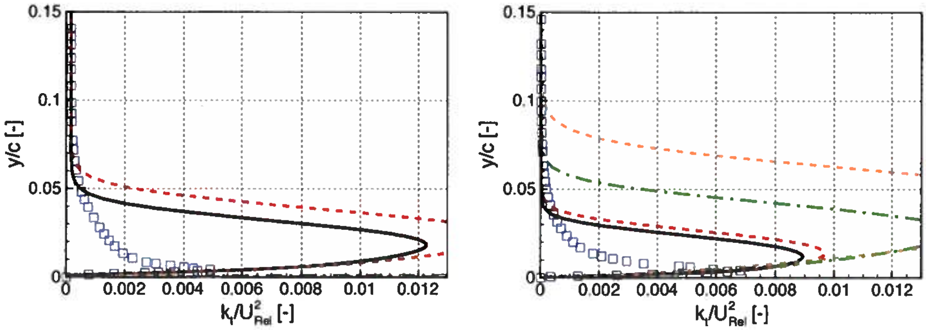

(a) Strip 1.

(b) Strip 3.

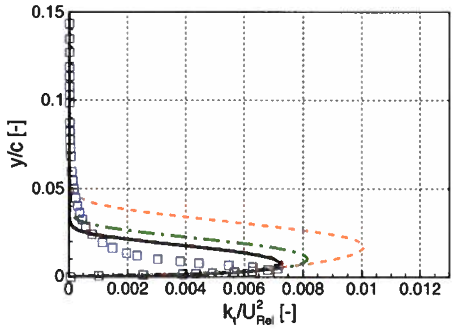

(c) Strip 5.

Figure B.3: The turbulent kinetic energy profiles extracted at $x/c = 0.99$ with respect to each strip location; $U_{z/c=-\infty}$ (——), $U_{z/c=-5.0}$ (- - -), $U_{z/c=-0.5}$ (-·-), $U_{z/c=0.667}$ (·····) and 3D simulation (□).

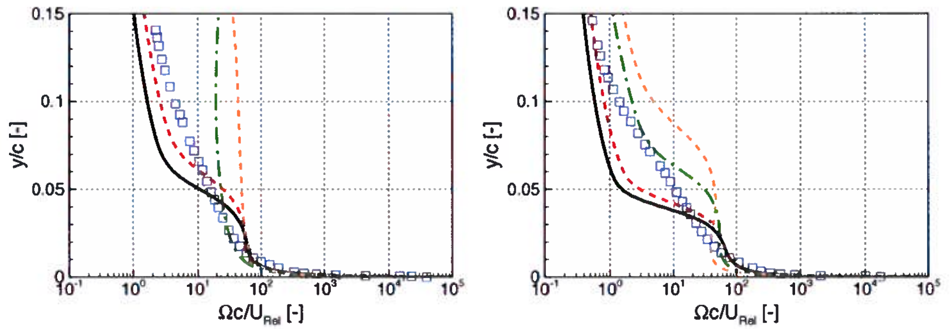

(a) Strip 1. (b) Strip 3.

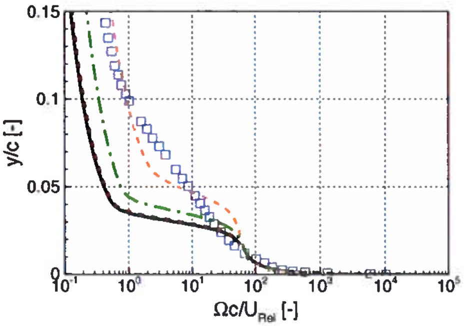

(c) Strip 5.

Figure B.4: The specific dissipation profiles extracted at $x/c = 0.99$ with respect to each strip location; $U_{z/c=-\infty}$ (——), $U_{z/c=-5.0}$ (- - -), $U_{z/c=-0.5}$ (-·-·), $U_{z/c=0.667}$ (·····) and 3D simulation (□).

Table B.1: Global variables at $x/c = 0.99$ for $U_{z/c=0.667}$.

Simulation	Side	Strip number	δ/c	U_e/U_{Rel}	u_τ/U_{Rel}^2	δ^*/c	θ/c	Π	β
$U_{z/c=0.667}$	Suction	*Strip 1*	-	-	-	-	-	-	-
		Strip 2	-	-	-	-	-	-	-
		Strip 3	-	-	-	-	-	-	-
		Strip 4	0.043	1.020	0.001	0.016	0.007	0.9827	0.8155
		Strip 5	0.042	1.001	0.001	0.015	0.007	1.2324	1.2792
	Pressure	*Strip 1*	0.010	1.737	0.019	0.002	0.001	0.2606	-0.2758
		Strip 2	0.009	1.461	0.008	0.002	0.001	-	-0.6291
		Strip 3	0.014	1.075	0.004	0.003	0.002	0.0675	-0.463
		Strip 4	0.016	1.002	0.002	0.003	0.002	0.1927	-0.3501
		Strip 5	0.015	0.985	0.002	0.003	0.002	0.2203	-0.3208

C

BUILDING INTEGRATED WIND TURBINE

The details about the Building Integrated Wind Turbine (BIWT) model is given. The model consists of three main modules; building, duct and wind turbine modules.

C.1. BUILDING INTEGRATED WIND TURBINE MODEL

C.1.1. BUILDING MODULE

The building model which is a 1/200 scale model of Brussels Finance Tower. The façade plate and interior of the module is shown.

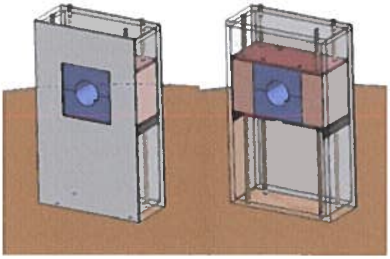

Figure C.1: Building part with and without façade plate and movable duct part.

C.1.2. DUCT MODULE

The duct module is used to adjust the height of the system and dismantle the wind turbine.

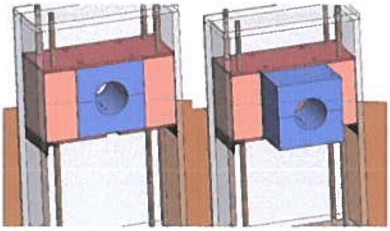

Figure C.2: Dismantling mechanism of duct module from building module.

C.1.3. WIND TURBINE MODULE

The duct module is used to adjust the height of the system and dismantle the wind turbine.

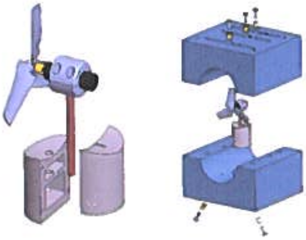

Figure C.3: Dismantling mechanism of duct module from building module.

C.2. POWER MEASUREMENTS

The electrical board shown in Fig. C.4 is used to perform the power measurements.

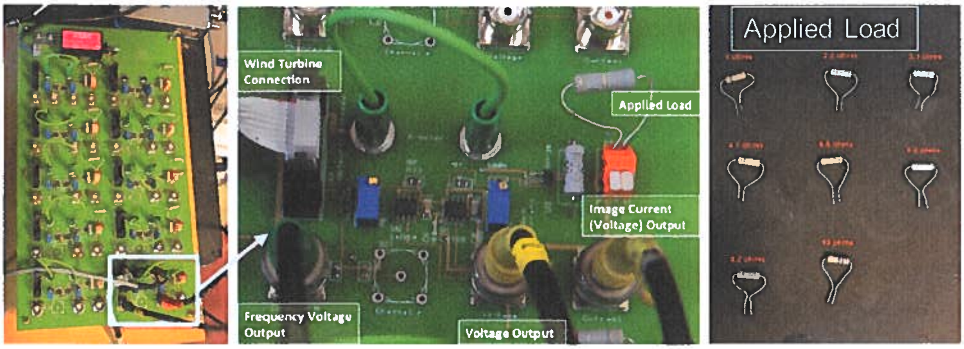

Figure C.4: The control board for wind farm (left), control board module (middle) and electrical resistance (right) [141].

C.3. ACOUSTIC MEASUREMENTS

The comparison of PSD with and without wind turbine at 0° a.o.a with GFC ABL configuration is given in Fig. C.5.

The effect of a.o.a is given in Fig. C.6 with G ABL configuration comparing the microphones at #3 axial position.

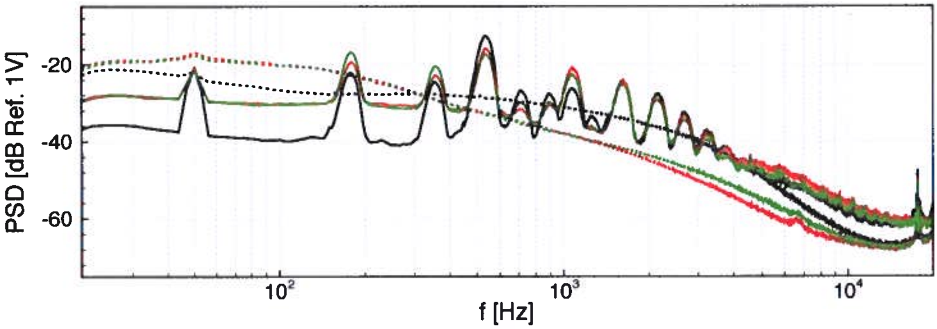

(a) Upstream microphone configuration.

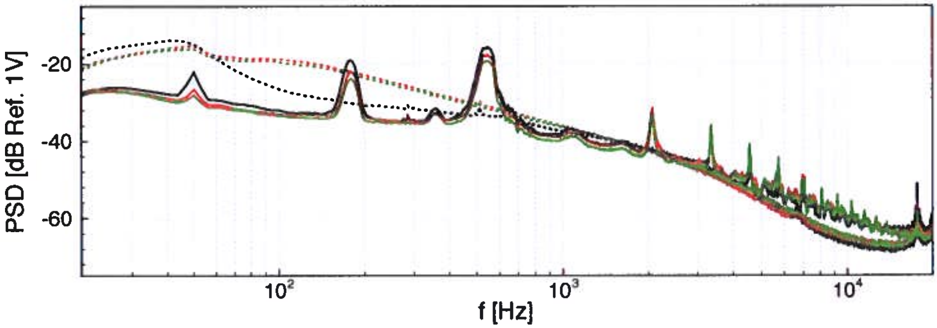

(b) Downstream microphone configuration.

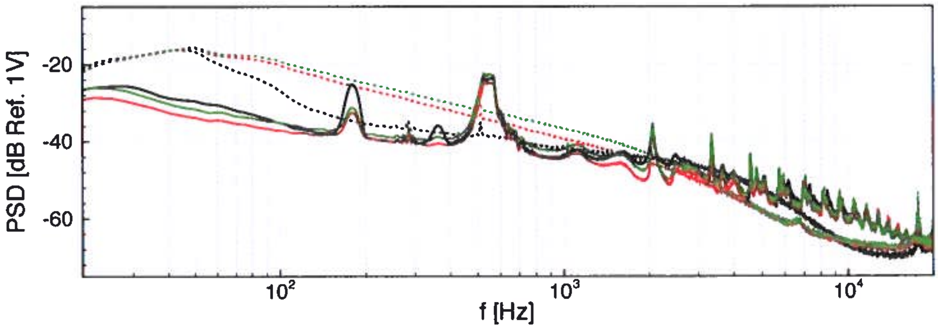

(c) Further downstream microphone configuration.

Figure C.5: Comparison of the PSD with and without wind turbine at 0° inflow direction with GFC ABL configuration; with wind turbine (solid line) and without wind turbine (dashed line), Microphones; number 1 (black), 2 (red) and 3 (green).

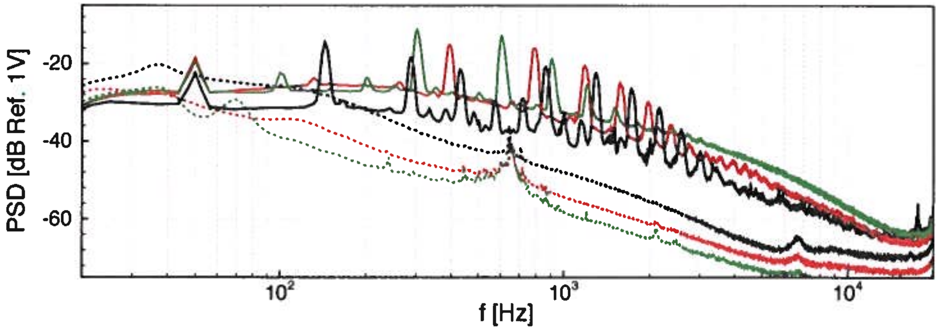

(a) Upstream microphone #3.

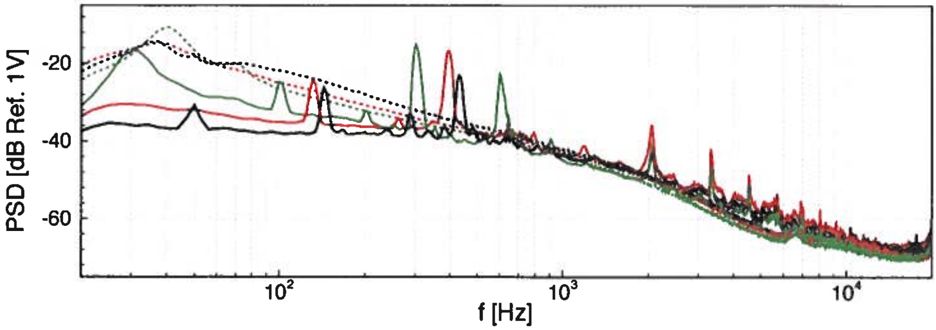

(b) Downstream microphone #3.

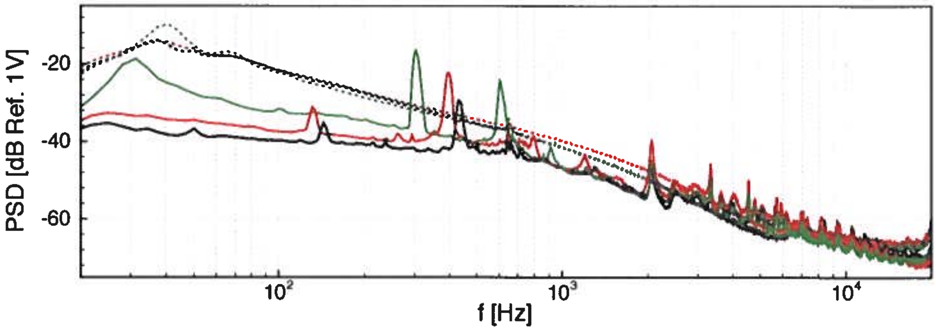

(c) Further downstream microphone #3.

Figure C.6: PSD comparison of microphones # 3 with and without wind turbine with G ABL configuration at different inflow directions; with wind turbine (solid line) and without wind turbine (dashed line), 0° (black), 30° (red) and 60° (green).

REFERENCES

[1] Abe, K., Nishida, M., Sakurai, A., Ohya, Y., Kihara, H., Wada, E., Sato, K., 2005. Experimental and numerical investigations of flow fields behind a small wind turbine with a flanged diffuser. Journal of Wind Engineering and Industrial Aerodynamics 93 (12), 951 – 970.

[2] Abe, K., Ohya, Y., 2004. An investigation of flow fields around flanged diffusers using CFD. Journal of Wind Engineering and Industrial Aerodynamics 92 (3), 315 – 330.

[3] Al-Kodmany, K., 2014. Green towers and iconic design: cases from three continents. Archnet-IJAR: International Journal of Architectural Research 8 (1), 11–29.

[4] Al-mulali, U., Fereidouni, H. G., Lee, J. Y., Sab, C. N. B. C., 2013. Exploring the relationship between urbanization, energy consumption, and CO2 emission in MENA countries. Renewable and Sustainable Energy Reviews 23, 107–112.

[5] Amiet, R., 1975. Acoustic radiation from an airfoil in a turbulent stream. Journal of Sound and Vibration 41 (4), 407–420.

[6] Amiet, R., 1976. Noise due to turbulent flow past a trailing edge. Journal of Sound and Vibration 47 (3), 387–393.

[7] Amiet, R., 1977. Noise produced by turbulent flow into a propeller or helicopter rotor. AIAA Journal 15 (3), 307–308.

[8] Amiet, R., 1978. Effect of the incident surface pressure field on noise due to turbulent flow past a trailing edge. Journal of Sound and Vibration 57 (2), 305–306.

[9] Anselmi, L., 2017. Computational analysis of ducted wind turbines noise. Master's thesis, Delft University of Technology.

[10] Antonini, C., Persico, G., Rowe, A. L., 2008. Prediction of the dynamic response of complex transmission line systems for unsteady pressure measurements. Measurement Science and Technology 19 (12), 125401.

[11] Aranake, A., Duraisamy, K., 2017. Aerodynamic optimization of shrouded wind turbines. Wind Energy 20 (5), 877–889.

[12] Aranake, A. C., Lakshminarayan, V. K., Duraisamy, K., 2014. Assessment of low-order theories for analysis and design of shrouded wind turbines using CFD. Journal of Physics: Conference Series 524 (1), 012077.

[13] Aranake, A. C., Lakshminarayan, V. K., Duraisamy, K., 2015. Computational analysis of shrouded wind turbine configurations using a 3-dimensional RANS solver. Renewable Energy 75, 818–832.

[14] Arguillat, B., 2006. Étude expérimentale et numérique de champs de pression pariétale dans l'espace des nombres d'onde, avec application aux vitrages automobiles. Ph.D. thesis, Ecole Centrale de Lyon.

[15] Avallone, F., van der Velden, W., Ragni, D., 2017. Benefits of curved serrations on broadband trailing-edge noise reduction. Journal of Sound and Vibration 400, 167–177.

[16] Bak, C., Johansen, J., Anderse, P. B., 2006. Three-dimensional corrections of airfoil characteristics based on pressure distributions. In: European Wind Energy Conference & Exhibition (EWEC). Athens, Greece.

[17] Bakker, R., Pedersen, E., van den Berg, G., Stewart, R., Lok, W., Bouma, J., 2012. Impact of wind turbine sound on annoyance, self-reported sleep disturbance and psychological distress. Science of The Total Environment 425, 42–51.

[18] Bangga, G., Lutz, T., Jost, E., Krämer, E., 2017. CFD studies on rotational augmentation at the inboard sections of a 10 MW wind turbine rotor. Journal of Renewable and Sustainable Energy 9 (2), 023304.

[19] Barlas, E., 2014. Experimental investigation of wind turbine / farm wakes in a boundary layer wind tunnel. Master's thesis, von Karman Institute for Fluid Dynamics.

[20] Barone, M. F., 2011. Survey of techniques for reduction of wind turbine blade trailing edge noise.

[21] Bergh, H., Tijdeman, H., 1965. Theoretical and experimental results for the dynamic response of pressure measuring systems. Technical Report. National Aerospace Laboratory.

[22] Bertagnolio, F., 2008. Trailing edge noise model applied to wind turbine airfoils. Constraints 4, 0–002.

[23] Betz, A., 1920. Das maximum der theoretisch moglichen ausnutzung des windes durch windmotoren. Zeitschrift für das gesamte Turbinenwesen 26, 307–309.

[24] Betz, A., 1929. Energieumsetzungen in venturidüsen. Naturwissenschaften 17 (10), 160–164.

[25] Blake, W. K., 1986. Mechanics of flow-induced sound and vibration Volume I, General concepts and elementary sources. Academic Press.

[26] Blandeau, V. P., Joseph, P. F., 2011. Validity of Amiet's model for propeller trailing-edge noise. AIAA Journal 49 (5), 1057–1066.

[27] Bontempo, R., Cardone, M., Manna, M., Vorraro, G., 2014. Ducted propeller flow analysis by means of a generalized actuator disk model. Energy Procedia 45, 1107 – 1115, aTI 2013 - 68th Conference of the Italian Thermal Machines Engineering Association.

[28] Bontempo, R., Manna, M., 2014. Performance analysis of open and ducted wind turbines. Applied Energy 136, 405 – 416.

[29] Bowdler, R., Leventhall, G., 2012. Wind turbine noise. Multi-Science Publishing Co Ltd.

[30] Bree, H.-E. d., Eerden, F. v. d., Honschoten, J. v., 2000. A novel technique for measuring the reflection coefficient of sound absorbing materials.

[31] Brooks, T., Pope, D., Marcolini, M., 1989. Airfoil self-noise and prediction. NASA reference publication. National Aeronautics and Space Administration, Office of Management, Scientific and Technical Information Division.

[32] Buckingham, S., 2010. Wind park siting in complex terrains assessed by wind tunnel simulations. Master's thesis, von Karman Institute for Fluid Dynamics.

[33] Caetano Alves, J., 2005. Premesys v2.0: a software tool to characterize the dynamic response of apressure measurement system.

[34] Campbell, N., Stankovic, S., 1999. Wind Energy for the Built Enviroment (Project WEB). Tech. rep.

[35] Campbell, N., Stankovic, S., M. Graham, P. P., van Duijvendijk, M., de Gruiter, T., Behling, S., J. Hieber, M. B., 2001. Wind energy for the built enviroment (project web). In: European Wind Energy Conference & Exhibition. Copenhagen.

[36] Carcangiu, C. E., Sørensen, J. N., Cambuli, F., Mandas, N. 2007. CFD–RANS analysis of the rotational effects on the boundary layer of wind turbine blades. Journal of Physics: Conference Series 75, 012031.

[37] Casalino, D., Barbarino, M., 2011. Stochastic method for airfoil self-noise computation in frequency domain. AIAA Journal 49 (11), 2453–2469.

[38] Catalano, P., Amato, M., 2003. An evaluation of RANS turbulence modelling for aerodynamic applications. Aerospace science and Technology 7 (7), 493–509.

[39] Catlett, M. R., Anderson, J. M., Forest, J. B., Stewart, D. O., 2015. Empirical modeling of pressure spectra in adverse pressure gradient turbulent boundary layers. AIAA Journal 54 (2), 569–587.

[40] Chandiramani, K. L., 1974. Diffraction of evanescent waves, with applications to aerodynamically scattered sound and radiation from unbaffled plates. The Journal of the Acoustical Society of America 55 (1), 19.

[41] Chase, D., 1980. Modeling the wavevector-frequency spectrum of turbulent boundary layer wall pressure. Journal of Sound and Vibration 70 (1), 29–67.

[42] Chauveau, M., 2017. Instantaneous measurements of fluctuating temperature and velocity. Master's thesis, von Karman Institute for Fluid Dynamics.

[43] Chaviaropoulos, P., Hansen, M., 2000. Investigating three-dimensional and rotational effects on wind turbine blades by means of a quasi-3D Navier-Stokes Solver. Journal of Fluids Engineering 122, 330–336.

[44] Chitale, K. C., Rasquin, M., Sahni, O., Shephard, M. S., Jansen, K. E., 2014. Boundary layer adaptivity for incompressible turbulent flows. ArXiv e-prints.

[45] Christophe, J., Moreau, S., Hamman, C. W., Witteveen, J. A. S., Iaccarino, G., 2014. Uncertainty quantification for the trailing-edge noise of a controlled-diffusion airfoil. AIAA Journal 53 (1), 42–54.

[46] Clauser, F. H., 1954. Turbulent boundary layers in adverse pressure gradients. Journal of the Aeronautical Sciences 21 (2), 91–108.

[47] Coles, D., 1956. The law of the wake in the turbulent boundary layer. Journal of Fluid Mechanics 1 (2), 191–226.

[48] Conan, B., 2012. Wind resource assesment in complex terrain by wind tunnel modelling. Ph.D. thesis, Université d'Orléans.

[49] Corcos, G. M., 1964. The structure of the turbulent pressure field in boundary-layer flows. Journal of Fluid Mechanics 18 (03), 353.

[50] Coudou, N., 2016. Wind turbine / farm wake(s) meandering study in an ABL tunnel. Master's thesis, von Karman Institute for Fluid Dynamics.

[51] Curle, N., 1955. The influence of solid boundaries upon aerodynamic sound. Proceedings of the Royal Society A: Mathematical, Physical and Engineering Sciences 231 (1187), 505–514.

[52] Dayan, E., 2006. Wind energy in buildings. Refocus 7 (2), 33–38.

[53] Degrassi, S., Castelli, M. R., Benini, E., 2013. A retrospective of wind turbine architectural integration in the built environment. World Academy of Science, Engineering and Technology International Journal of Civil, Environmental, Structural, Construction and Architectural Engineeringy 7 (6), 417–421.

[54] der Luft im VDI und DIN. Normenausschuss, K. R., 2000. Environmental meteorology : physical modelling of flow and dispersion processes in the atmospheric boundary layer : application of wind tunnels:. DIN-VDI-Taschenbuch. Beuth Verlag.

[55] Dick, E., 1986. Power limits for wind energy concentrator systems. Wind Engineering 10 (2), 98–115.

[56] Dighe, V., Avallone, F., van Bussel, G., 2016. Computational study of diffuser augmented wind turbine using actuator disc force method. International Journal of Computational Methods and Experimental Measurements 4 (4), 522–531.

[57] Dighe, V. V., Avallone, F., Tang, J., van Bussel, G., Jan 2017. Effects of gurney flaps on the performance of diffuser augmented wind turbine. American Institute of Aeronautics and Astronautics.

[58] Doolan, C., 2013. A review of wind turbine noise perception, annoyance and low frequency emission. Wind Engineering 37 (1), 97–104.

[59] Doolan, C. J., Gonzalez, C. A., Hansen, C. H., 2010. Statistical estimation of turbulent trailing edge noise. In: Proceedings of 20th International Congress on Acoustics. American Institute of Aeronautics and Astronautics.

[60] Doolan, C. J., Moreau, D. J., Brooks, L. A., 2012. Wind turbine noise mechanisms and some concepts for its control. Acoustics Australia 40 (1).

[61] Drela, M., 1989. Xfoil: An analysis and design system for low Reynolds number airfoils. In: Mueller, T. J. (Ed.), Low Reynolds Number Aerodynamics. Springer Berlin Heidelberg, Berlin, Heidelberg, pp. 1–12.

[62] Du, Z., Selig, M., jan 1998. A 3-D stall-delay model for horizontal axis wind turbine performance prediction. In: 1998 ASME Wind Energy Symposium. American Institute of Aeronautics and Astronautics.

[63] Du, Z., Selig, M., 2000. The effect of rotation on the boundary layer of a wind turbine blade. Renewable Energy 20 (2), 167–181.

[64] Dumitrache, A., Cardos, V., Dumitrescu, H., Simos, T. E., Psihoyios, G., Tsitouras, C., 2010. Delayed stall modeling of the rotating blades. AIP.

[65] Dumitrescu, H., Cardos, V., 2009. Inboard boundary layer state on wind turbine blades. ZAMM-Journal of Applied Mathematics and Mechanics/Zeitschrift fur Angewandte Mathematik und Mechanik 89 (3), 163–173.

[66] Dumitrescu, H., Cardos, V., 2012. Inboard stall delay due to rotation. Journal of Aircraft 49 (1), 101–107.

[67] Durbin, P., Reif, B., 2011. Statistical theory and modeling for turbulent flows. Wiley.

[68] E., L., 2011. Advanced cfd methods for wind turbine analysis. Ph.D. thesis, Georgia Institute of Technology, Atlanta, GA, USA.

[69] Efimtsov, B., 1982. Characteristics of the field of turbulent wall pressure-fluctuations at large Reynolds-numbers. Soviet Physics Acoustics-USSR 28 (4), 289–292.

[70] Ewert, R., 2007. RPM - the Fast Random Particle-Mesh Method to realize unsteady turbulent sound sources and velocity fields for CAA Applications. In: 13th AIAA/CEAS Aeroacoustics Conference (28th AIAA Aeroacoustics Conference). Vol. 4. American Institute of Aeronautics and Astronautics, Reston, Virigina, p. 1.

[71] Ewert, R., 2008. Broadband slat noise prediction based on CAA and stochastic sound sources from a fast random particle-mesh (RPM) method. Computers & Fluids 37 (4), 369–387.

[72] Fletcher, C. A., 1981. Computational analysis of diffuser-augmented wind turbines. Energy Conversion and Management 21 (3), 175 – 183.

[73] Foreman, K., 1981. Preliminary design and economic investigations of Diffuser-augmented Wind Turbines (DAWT). Executive Summary. Final Report. National Renewable Energy Laboratory (U.S.).

[74] Garratt, J. R., 1994. The atmospheric boundary layer (Cambridge Atmospheric and Space Science Series). Cambridge University Press.

[75] Giahi, M. H., Dehkordi, A. J., 2016. Investigating the influence of dimensional scaling on aerodynamic characteristics of wind turbine using CFD simulation. Renewable Energy 97, 162–168.

[76] Gilbert, B. L., Foreman, K. M., 1979. Experimental demonstration of the diffuser-augmented wind turbine concept. Journal of Energy 3 (4), 235–240.

[77] Gilbert, B. L., Oman, R. A., Foreman, K. M., 1978. Fluid dynamics of diffuser-augmented wind turbines. Journal of Energy 2 (6), 368–374.

[78] Gloerfelt, X., Le Garrec, T., 2009. Trailing edge noise from an isolated airfoil at a high Reynolds number. AIAA Journal.

[79] Goody, M., 2004. Empirical spectral model of surface pressure fluctuations. AIAA Journal 42 (9), 1788–1794.

[80] Grönman, A., Backman, J., Avramenko, A., 2014. Wind profile effect on small wind turbine noise generation. In: Volume 3B: Oil and Gas Applications Organic Rankine Cycle Power Systems Supercritical CO2 Power Cycles Wind Energy. ASME.

[81] Guerri, O., Bouhadef, K., Harhad, A., 2006. Turbulent flow simulation of the NREL S809 airfoil. Wind Engineering 30 (4), 287–301.

[82] Guidati, G., Barei, R., Wagner, S., 1994. An investigation of blade-tower-interaction noise (bti) for horizontal axis wind turbines in upwind and downwind configuration. first steps towards modeling of aeroelastic effects. In: Proc. 8th IEA Symposium. pp. 249–255.

[83] Guilmineau, E., Piquet, J., Queutey, P., 1997. Two-dimensional turbulent viscous flow simulation past airfoils at fixed incidence. Computers & Fluids 26 (2), 135–162.

[84] Gumley, S., 1983. A detailed design method for pneumatic tubing systems. Journal of Wind Engineering and Industrial Aerodynamics 13 (1), 441 – 452.

[85] H. Snel, R. Houwink, J. B., 1994. Sectional Prediction of Lift Coefficients on Rotating Wind Turbine Blades in Stall. Netherlands Energy Research Foundation.

[86] Hansen, C. H., Doolan, C. J., Hansen, K. L., 2017. Wind Farm Noise: Measurement, Assessment, and Control (Wiley Series in Acoustics Noise and Vibration). Wiley.

[87] Hansen, M., Sørensen, J., Voutsinas, S., Sørensen, N., Madsen, H., 2006. State of the art in wind turbine aerodynamics and aeroelasticity. Progress in Aerospace Sciences 42 (4), 285–330.

[88] Hansen, M. O. L., 2008. Aerodynamics of Wind Turbines. Earthscan Publications Ltd.

[89] Hansen, M. O. L., Madsen, H. A., 2011. Review paper on wind turbine aerodynamics. Journal of Fluids Engineering 133 (11), 114001.

[90] Hansen, M. O. L., Sørensen, N. N., Flay, R. G. J., 2000. Effect of placing a diffuser around a wind turbine. Wind Energy 3 (4), 207–213.

[91] Herr, M., Bahr, C. J., Kamruzzaman, M., 2012. Problem Statement for the AIAA/CEAS Second Workshop on Benchmark Problems for Airframe Noise Computations (BANC-II). AIAA Journal.

[92] Herr, M., Ewert, R., Rautmann, C., Kamruzzaman, M., Bekiropoulos, D., Arina, R., Iob, A., Batten, P., Chakravarthy, S., Bertagnolio, F., 2015. Broadband Trailing-Edge Noise Predictions—Overview of BANC-III Results. In: 21st AIAA/CEAS Aeroacoustics Conference. American Institute of Aeronautics and Astronautics, Reston, Virginia.

[93] Herrig, A., Kamruzzaman, M., Würz, W., Wagner, S., 2013. Broadband airfoil trailing-edge noise prediction from measured surface pressures and spanwise length scales. International Journal of Aeroacoustics 12 (1-2), 53–82.

[94] Himmelskamp, H., 1945. Profile investigations on a rotating airscrew. Ph.D. thesis, Gottingen University, Germany.

[95] Hirschberg, A., Rienstra, S. W., 2004. An introduction to aeroacoustics. Tech. rep.

[96] Holmberg, A., Åbom, M., Bodén, H., 2011. Accurate experimental two-port analysis of flow generated sound. Journal of Sound and Vibration 330 (26), 6336 – 6354.

[97] Howe, M. S., 1998. Acoustics of Fluid-Structure Interactions. Cambridge University Press, Cambridge.

[98] Hu, N., Herr, M., 2016. Characteristics of wall pressure fluctuations for a flat plate turbulent boundary layer with pressure gradients. In: 22nd AIAA/CEAS Aeroacoustics Conference. Aeroacoustics Conferences. American Institute of Aeronautics and Astronautics, p. 2749, 0.

[99] Hu, S.-Y., Cheng, J.-H., 2008. Innovatory designs for ducted wind turbines. Renewable Energy 33 (7), 1491–1498.

[100] Hurst, A. M., Van De Weert, J., 2013. An experimental and theoretical investigation of wave propagation in teflon and nylon tubing with methods to prevent aliasing in pressure scanners. Journal of Engineering for Gas Turbines and Power 135 (10), 101602–101602.

[101] Hwang, Y., Bonness, W. K., Hambric, S. A., 2009. Comparison of Semi-Empirical Models for Turbulent Boundary Layer Wall Pressure Spectra. Journal of Sound and Vibration 319 (1), 199–217.

[102] Igra, O., 1976. Shrouds for aerogenerators. AIAA Journal 14 (10), 1481–1483.

[103] Igra, O., 1977. The shrouded aerogenerator. Energy 2 (4), 429 – 439.

[104] Igra, O., 1981. Research and development for shrouded wind turbines. Energy Conversion and Management 21 (1), 13 – 48.

[105] Irwin, H., Cooper, K., Girard, R., 1979. Correction of distortion effects caused by tubing systems in measurements of fluctuating pressures. Journal of Wind Engineering and Industrial Aerodynamics 5 (1), 93 – 107.

[106] Ishugah, T., Li, Y., Wang, R., Kiplagat, J., 2014. Advances in wind energy resource exploitation in urban environment: A review. Renewable and Sustainable Energy Reviews 37, 613–626.

[107] Iwasaki, M., 1953. The experimental and theoretical investigation of windmills. Reports of Research Institute for Applied Mechanics 2 (8), 181–229.

[108] Jamieson, P. M., 2009. Beating Betz: Energy extraction limits in a constrained flow field. Journal of Solar Energy Engineering 131 (3), 031008–031008–6.

[109] Jones, D. W., 1991. How urbanization affects energy-use in developing countries. Energy Policy 19 (7), 621–630.

[110] Kamruzzaman, M., Bekiropoulos, D., Lutz, T., Würz, W., Krämer, E., 2015. A semi-empirical surface pressure spectrum model for airfoil trailing-edge noise prediction. International Journal of Aeroacoustics 14 (5-6), 833–882.

[111] Kamruzzaman, M., Herrig, A., Lutz, T., Würz, W., Krämer, E., Wagner, S., 2011. Comprehensive evaluation and assessment of trailing edge noise prediction based on dedicated measurements. Noise Control Engineering Journal 59 (1), 54.

[112] Kardous, M., Chaker, R., Aloui, F., Nasrallah, S. B., 2013. On the dependence of an empty flanged diffuser performance on flange height: Numerical simulations and PIV visualizations. Renewable Energy 56, 123 – 128, the International Conference on Renewable Energy: Generation and Applications.

[113] Klebanoff, P. S., January 1955. Characteristics of turbulence in boundary layer with zero pressure gradient. Tech. rep.

[114] Kogan, A., Seginer, A., 1963. Final Report on Shroud Design. Tech. rep., Dept. of Aeronautical Eng.,.

[115] Kogan, A., Seginer, A., 1963. Shrouded Aerogenerator Desing Study II, Axisymmetric Shroud Performance. Tech. rep., Dept. of Aeronautical Eng.,.

[116] Kraichnan, R. H., 1956. Pressure fluctuations in turbulent flow over a flat plate. The Journal of the Acoustical Society of America 28 (3), 378–390.

[117] Kral, L., 1998. Recent experience with different turbulence models applied to the calculation of flow over aircraft components. Progress in Aerospace Sciences 34 (7), 481–541.

[118] Küçükcoskun, K., 2012. Prediction of free and scattered acoustic fields of low-speed fans. Ph.D. thesis, Ecole Centrale de Lyon.

[119] Lee, S., Villaescusa, A., 2017. Comparison and assessment of recent empirical models for turbulent boundary layer wall pressure spectrum. In: 23rd AIAA/CEAS Aeroacoustics Conference. American Institute of Aeronautics and Astronautics, p. 3688.

[120] Lee, Y.-T., Blake, W. K., Farabee, T. M., 2004. Modeling of wall pressure fluctuations based on time mean flow field. Journal of Fluids Engineering 127 (2), 233–240.

[121] Lewis, R. I., Williams, J. E., Abdelghaffar, M. A., 1977. A theory and experimental investigation of ducted wind turbines. Wind Engineering 1, 104–125.

[122] Lighthill, M. J., 1952. On sound generated aerodynamically. i. general theory. Proceedings of the Royal Society A: Mathematical, Physical and Engineering Sciences 211 (1107), 564–587.

[123] Lighthill, M. J., 1954. On sound generated aerodynamically. II. turbulence as a source of sound. Proceedings of the Royal Society A: Mathematical, Physical and Engineering Sciences 222 (1148), 1–32.

[124] Lilley, G., Rainbird, W., Association, E. R., 1956. A Preliminary Report on the Design and Performance of Ducted Windmills. CoA report aero. College of Aeronautics.

[125] Lilley, G. M., Hodgson, T., 1960. On surface pressure fluctuations in turbulent boundary layers. Tech. rep., Advisory Group For Aeronautical Research and Development Paris(France).

[126] Lindenburg, C., 2004. Modelling of rotational augmentation based on engineering considerations and measurements. In: European Wind Energy Conference. London, pp. 22–25.

[127] Loeffler, A. L., Steinhoff, J. S., 1985. Computation of wind tunnel wall effects in ducted rotor experiments. Journal of Aircraft 22 (3), 188–192.

[128] Loeffler, J. A. L., 1981. Flow field analysis and performance of wind turbines employing slotted diffusers. Journal of Solar Energy Engineering 103 (1), 17–22.

[129] Lowson, M. V., 1965. The sound field for singularities in motion. Proceedings of the Royal Society A: Mathematical, Physical and Engineering Sciences 286 (1407), 559–572.

[130] Menter, F. R., 1994. Two-equation eddy-viscosity turbulence models for engineering applications. AIAA Journal 32 (8), 1598–1605.

[131] Mertens, S., 2006. Wind Energy in the Built Environment: Concentrator Effects of Buildings. Multiscience Publishing.

[132] Moreau, A., Guerin, S., Enghardt, L., Denmat, A.-L. L., Nicke, E., Weber, S., Diehl, S., Koch, P., 2012.

[133] Moreau, S., Roger, M., jan 2007. Competing broadband noise mechanisms in low-speed axial fans. AIAA Journal 45 (1), 48–57.

[134] Moriarty, P., Migliore, P. G., (U.S.), N. R. E. L., 2003. Semi-empirical aeroacoustic noise prediction code for wind turbines [electronic resource] / P. Moriarty and P. Migliore. National Renewable Energy Laboratory Golden, Colo.

[135] Moshfeghi, M., Song, Y. J., Xie, Y. H., 2012. Effects of near-wall grid spacing on SST-k-ω model using NREL phase VI horizontal axis wind turbine. Journal of Wind Engineering and Industrial Aerodynamics 107-108, 94–105.

[136] Nash, J. F., 1966. Turbulent-Boundary-Layer Behaviour and the Auxiliary Equation. HM Stationery Office.

[137] Nations, U., 2007. City planning will determine pace of global warming.

[138] Oerlemans, S., Schepers, J. G., 2009. Prediction of wind turbine noise and validation against experiment. International Journal of Aeroacoustics 8 (6), 555–584.

[139] Ohya, Y., Karasudani, T., 2010. A shrouded wind turbine generating high output power with wind-lens technology. Energies 3 (4), 634–649.

[140] Ohya, Y., Karasudani, T., Sakurai, A., ichi Abe, K., Inoue, M., 2008. Development of a shrouded wind turbine with a flanged diffuser. Journal of Wind Engineering and Industrial Aerodynamics 96 (5), 524 – 539.

[141] Özçakmak, O. S., 2016. Building integrated wind turbines. Master's thesis, von Karman Institute for Fluid Dynamics.

[142] Panton, R. L., Linebarger, J. H., 1974. Wall pressure spectra calculations for equilibrium boundary layers. Journal of Fluid Mechanics 65 (02), 261.

[143] Pape, A. L., Lecanu, J., 2004. 3D Navier-Stokes computations of a stall-regulated wind turbine. Wind Energy 7 (4), 309–324.

[144] Parchen, R., TNO-TH., T. P. D., 1998. Progress report DRAW: a prediction scheme for trailing edge noise based on detailed boundary layer characteristics. TNO-report HAG-RPT. TNO Institute of Applied Physics.

[145] Park, J., Jung, H.-J., Lee, S.-W., Park, J., 2015. A new building-integrated wind turbine system utilizing the building. Energies 8 (10), 11846–11870.

[146] Perea-Moreno, M.-A., Hernandez-Escobedo, Q., Perea-Moreno, A.-J., 2018. Renewable energy in urban areas: Worldwide research trends. Energies 11 (3), 577.

[147] Perennes, S., Roger, M., 1998. Aerodynamic noise of a two-dimensional wing with high-lift devices. In: 4th AIAA/CEAS Aeroacoustics Conference. p. 2338.

[148] Philips, D., 2003. An investigation on diffuser augmented wind turbine design. Ph.D. thesis, Unverstiy of Auckland.

[149] Phillips, D., Flay, R., Nash, T., 1998. Aerodynamic analysis and monitoring of the vortec 7 diffuser-augmented wind turbine. In: IPENZ Conference. Auckland, New Zealand.

[150] Phillips, D., Richards, P., G.D., M., Flay, R., 1998. Computational modelling of diffuser designs for a diffuser augmented wind turbine. In: 13th Australasian Fluid Mechanics Conference. Monash University, Melbourne, Australia.

[151] Pinder, J., 1992. Mechanical noise from wind turbines. Wind Engineering 16 (3), 158–168.

[152] Ramachandran, R. C., Patel, H., Raman, G., Jiang, Y., Krishnamurthy, M., 2014. Noise source localization on a small wind turbine using a compact microphone array with advanced beamforming algorithms: Part i — a study of aerodynamic noise from blades. Wind Engineering 38 (1), 73–88.

[153] Redonnet, S., Jun. 2014. Aircraft noise prediction via aeroacoustic hybrid methods - development and application of onera tools over the last decade : some examples. AerospaceLab (7), p. 1–16.

[154] Remmler, S., Christophe, J., Anthoine, J., Moreau, S., 2010. Computation of wall pressure spectra from steady flow data for noise prediction. AIAA Journal 48 (9), 1997–2007.

[155] Roger, M., 2004. Noise from moving surfaces. In: Advances in aeroacoustics and applications. von Karman Institute for Fluid Dynamics.

[156] Roger, M., Moreau, S., 2005. Back-scattering correction and further extensions of Amiet's trailing-edge noise model. Part 1: theory. Journal of Sound and Vibration 286 (3), 477–506.

[157] Rotta, J., 1953. On the theory of the turbulent boundary layer.

[158] Rozenberg, Y., 2007. Modélisation analytique du bruit aérodynamique à large bande des machines tournantes : utilisation de calculs moyennés de mécanique des fluides. Ph.D. thesis, Ecole Centrale de Lyon.

[159] Rozenberg, Y., Robert, G., Moreau, S., 2012. Wall-pressure spectral model including the adverse pressure gradient effects. AIAA Journal 50 (10), 2168–2179.

[160] Sack, S., Åbom, M., Schram, C., Kucukcoskun, K., Jun 2014. Generation and scattering of acoustic modes in ducts with flow.

[161] Sanderg, R. D., Sandham, N. D., jan 2008. Direct numerical simulation of turbulent flow past a trailing edge and the associated noise generation. Journal of Fluid Mechanics 596.

[162] Sanjosé, M., Moreau, S., 2011. Direct simulation of trailing-edge noise generated by a controlled diffusion airfoil using a lattice-boltzmann method.

[163] Sanuki, M., 1950. Studies on biplane wind vanes, ventilator tubes and cup anemometers (i). Papers in Meteorology and Geophysics 1 (1), 81–132.

[164] Schetz, J. A., 1993. Boundary Layer Analysis. NASA STI/Recon Technical Report A 93.

[165] Schlinker, R., Amiet, R., 1981. Helicopter rotor trailing edge noise. In: 7th Aeroacoustics Conference. American Institute of Aeronautics and Astronautics.

[166] Schroeder, W., Martin, K., Lorensen, B., 2006. Visualization Toolkit: An Object-Oriented Approach to 3D Graphics, 4th Edition. Kitware.

[167] Selig, M., 2003. Low reynolds number airfoil design lecture notes. VKI Lecture Series, 24–28.

[168] Shen, W. Z., Sørensen, J. N., 1999. Quasi-3D Navier–Stokes model for a rotating airfoil. Journal of Computational Physics 150 (2), 518–548.

[169] Siddiqui, M. S., Rasheed, A., Tabib, M., Kvamsdal, T., 2016. Numerical analysis of NREL 5MW wind turbine: a study towards a better understanding of wake characteristic and torque generation mechanism. Journal of Physics: Conference Series 753 (3), 032059.

[170] Sinayoko, S., Hurault, J., 2015. On predicting wind turbine noise and amplitude modulation using amiet's theory. In: Conference: International Conference on Wind Turbine Noise.

[171] Sinayoko, S., Kingan, M., Agarwal, A., 2013. Trailing edge noise theory for rotating blades in uniform flow. Proceedings of the Royal Society A: Mathematical, Physical and Engineering Sciences 469 (2157), 20130065–20130065.

[172] Smol'yakov, A. V., 2006. A new model for the cross spectrum and wavenumber-frequency spectrum of turbulent pressure fluctuations in a boundary layer. Acoustical Physics 52 (3), 331–337.

[173] Sørensen, N., Michelsen, J., et al., 2004. Drag prediction for blades at high angle of attack using CFD. Transactions-American Society of Mechanical Engineers Journal of Solar Energy Engineering 126 (4), 1011–1016.

[174] Sørensen, N. N., Michelsen, J., Schreck, S., 2002. Navier-stokes predictions of the NREL phase vi rotor in the nasa ames 80 ftv× 120 ft wind tunnel. Wind Energy 5 (2-3), 151–169.

[175] Spalart, P., Allmaras, S., 1992. A one-equation turbulence model for aerodynamic flows. In: 30th Aerospace Sciences Meeting and Exhibit. American Institute of Aeronautics and Astronautics.

[176] Standard, B.-A. E., 2005. BS EN 1991-1-4:2005+A1:2010: Eurocode 1. Actions on structures. General actions. Wind actions. British-Adopted European Standard.

[177] Stankovic, S., Campbell, N., Harries, A., 2015. Urban Wind Energy. Routledge.

[178] Stathopoulos, T., Alrawashdeh, H., Al-Quraan, A., Blocken, B., Dilimulati, A., Paraschivoiu, M., Pilay, P., 2018. Urban wind energy: Some views on potential and challenges. Journal of Wind Engineering and Industrial Aerodynamics 179, 146–157.

[179] Surry, D., Stathopoulos, T., 1978. An experimental approach to the economical measurement of spatially-averaged wind loads. Journal of Wind Engineering and Industrial Aerodynamics 2 (4), 385 – 397.

[180] Tachos, N. S., Filios, A. E., Margaris, D. P., 2010. A comparative numerical study of four turbulence models for the prediction of horizontal axis wind turbine flow. Proceedings of the Institution of Mechanical Engineers, Part C: Journal of Mechanical Engineering Science 224 (9), 1973–1979.

[181] Tang, J., Avallone, F., van Bussel, G., 2016. Experimental study of flow field of an aerofoil shaped diffuser with a porous screen simulating the rotor. International Journal of Computational Methods and Experimental Measurements 4 (4), 502–512.

[182] Taylor, J., Eastwick, C., Lawrence, C., Wilson, R., 2013. Noise levels and noise perception from small and micro wind turbines. Renewable Energy 55, 120–127.

[183] Temel, O., Bricteux, L., van Beeck, J., 2018. Coupled WRF-OpenFOAM study of wind flow over complex terrain. Journal of Wind Engineering and Industrial Aerodynamics 174, 152–169.

[184] ten Hoopen, P., 2009. An Experimental and Computational Investigation of a Diffuser Augmented Wind Turbine. Master's thesis, Delft University, Delft, the Netherlands, m. Ss. Thesis.

[185] Thé, J., Yu, H., 2017. A critical review on the simulations of wind turbine aerodynamics focusing on hybrid RANS-LES methods. Energy 138, 257–289.

[186] Tian, Y., Cotté, B., 2016. Wind turbine noise modeling based on Amiet's theory: Effects of wind shear and atmospheric turbulence. Acta Acustica united with Acustica 102, 626–639.

[187] Tong, W., 2014. Mechanical Design of Electric Motors. CRC Press.

[188] Tonon, D., Hirschberg, A., Golliard, J., Ziada, S., 2011. Aeroacoustics of pipe systems with closed branches. Noise Notes 10 (3).

[189] Toshimitsu, K., Nishikawa, K., Haruki, W., Oono, S., Takao, M., Ohya, Y., 2008. Piv measurements of flows around the wind turbines with a flanged-diffuser shroud. Journal of Thermal Science 17 (4), 375–380.

[190] Tulapurkara, E., 1997. Turbulence models for the computation of flow past airplanes. Progress in Aerospace Sciences 33 (1), 71–165.

[191] van Bussel, D. G. J. W., 2007. The science of making more torque from wind: Diffuser experiments and theory revisited. Journal of Physics: Conference Series 75 (1), 012010.

[192] van Dorst, F., 2011. An improved rotor design for a diffuser augmented wind turbine. Master's thesis, Delft University, Delft, the Netherlands, m. Ss. Thesis.

[193] Vries, O. d., 1979. Fluid dynamic aspects of wind energy conversion. Tech. rep., Advisory Group for Aerospace Research and Development NEUILLY-SUR-SEINE (France).

[194] Wagner, S., Bareiß, R., Guidati, G., 1996. Wind Turbine Noise. Springer.

[195] Watson, S. J., Infield, D. G., Barton, J. P., Wylie, S. J., 2007. Modelling of the performance of a building-mounted ducted wind turbine. Journal of Physics: Conference Series 75 (1), 012001.

[196] Whitmore, S. A., Leondes, C. T., 1991. Pneumatic distortion compensation for aircraft surface pressure sensing devices. Journal of Aircraft 28 (12), 828–836.

[197] Williams, J. E. F., Hawkings, D. L., 1969. Sound generation by turbulence and surfaces in arbitrary motion. Philosophical Transactions of the Royal Society A: Mathematical, Physical and Engineering Sciences 264 (1151), 321–342.

[198] Willmarth, W. W., Roos, F. W., 1965. Resolution and structure of the wall pressure field beneath a turbulent boundary layer. Journal of Fluid Mechanics 22 (01), 81.

[199] Yakhot, V., Orszag, S. A., 1986. Renormalization group analysis of turbulence. i. basic theory. Journal of Scientific Computing 1 (1), 3–51.

[200] Zagarola, M. V., Smits, A. J., 1998. Mean-flow scaling of turbulent pipe flow. Journal of Fluid Mechanics 373, 33-79.

ACKNOWLEDGEMENTS

I always told myself that if I ever finish a Ph.D., I will start by thanking my parents. As I am a trustworthy person, I will keep my word. Mum and Dad, I want to thank you for making me and my education a top priority during this period. I couldn't be there for you during your hard times, but you were always with me whenever I needed you, no matter how hard the situation was. Even though I didn't show you how much your love and support helped me to move forward during this period, obviously, I couldn't have done it without you.

I am grateful to Prof. Christophe Schram who gave me the opportunity to start my career with my dream subject by accepting me for an 8 months project, which turned out to be a long term commitment to VKI. During this period, you guided me through not only scientific aspects of my project, but also personal development. You taught me the benefits of failure and the disadvantages of being a perfectionist, which was one of the toughest lesson I had to grasp. I would like to thank you for being open-minded, supportive, and believing in me until the end. I would like to express my deep appreciation to Julien Christophe without whom this thesis wouldn't exist. Thank you for helping me out with my biggest nightmare, meshing, and answering my endless questions with patience. Most of all, thank you for reminding me that I should have breaks sometimes. I would like to extend my thanks to Prof. Jeroen van Beeck for giving me the opportunity to be a part of the VKI family and for providing me with insightful discussions throughout this period. I owe a debt of gratitude for Mathieu, Gertjan, technicians, and IT team. Without them I couldn't conduct my experimental campaign nor run my simulations.

I am thankful to Prof. Damiano Casalino, Daniele Ragni and Francesco Avallone for giving me an opportunity in TU Delft. I have always felt very welcomed and supported during the time I spent there.

I would like to thank Prof. Michel Roger, Prof. Stéphane Moreau, Prof. Simon Watson and Dr. Stefan Oerlemans for having accepted to review my thesis and be part of my committee.

My dear master friends, Eduardo, Sri, Ilkay, Nick, and Oguzhan, even though we were living different parts of the world, you were always a phone call away whenever I needed. I know that I made a habit of calling you whenever I am in trouble and you kept calling me when I didn't have news to check on me, I deeply appreciate your concern! I am glad that we kept our passion for turbulence and helped to broaden my horizon.

My friends in VKI, during 4 years I have met numerous interesting, unique, and special people with whom I have established a strong bond. Orkun, Sara Porchetta, Taygun, Güven, Cem and Ali Can, thank you for being there not only for technical but also for spiritual support, I couldn't make it without you guys =) It was such a pleasure to share the office with Christopher, Andrea and Sara. Additional thanks to Marco, Ümran, Alejandro, Ernesto, Tania, Gian Luca, Fernando, Bruno, ïsa, Işıl, Sophia, Bayindir, Ertan, and also to my aeroacoustic group, Ugur, Gabriel, Daniel, Joachim, Zoé, Lionel, Ricardo and Alessandro.

To my third family, Aeolus4future, thank you for the crazy times we had during the workshops, conferences, and training. Especially, I want to thank you Giulio for being such a wonderful friend. I couldn't make it without you!

To my friends back home: Sare, Sena, Tilbe, Nermin, Deniz, Mete, Mustafa Can, Sinem, Nilufer, Eda, Mine, and Sera, and to my friends whom I met in Europe: Julia, Him, Myriam, Cecile, Celine, Marine, Bibiana, Ekin, Onursal, and Argun thank you for being there for me and making me feel loved.

I would like to also gratefully acknowledge the support of the European Commission's Framework Program "Horizon 2020", through the Marie Skłodowska-Curie Innovative Training Networks (ITN) "AEOLUS4FUTURE - Efficient harvesting of the wind energy" (H2020-MSCA-ITN-2014: Grant agreement no. 643167).

CURRICULUM VITÆ

Yakut Cansev KÜÇÜKOSMAN

27-04-1990	Born in Ankara, Turkey.

EDUCATION

2008–2012	B . Sc. in Aerospace Engineering, Middle East Technical University, Turkey.	
2012–2014	M. Sc. in Turbulence, EC Lille, ISAE-ENSMA, ENSIP / Lille-Poitiers, France.	
	Thesis:	The investigation of the wall signature of coherent structures in a turbulent boundary layer without adverse pressure gradient.
2015-2019	Ph. D. in Aeroacoustics, Faculty of Aerospace Engineering, Delft University of Technology, Delft, the Netherlands.	
	Thesis:	Semi-analytical approaches for the prediction of the noise produced by ducted wind turbines.
	Promotor:	Prof. dr. D. Casalino
	Copromotor:	Prof. dr. C. Schram